Department of Mechanical Engineering
The University of Michigan, Ann Arbor, Michigan

Modeling, Analysis and Control of Fuel Cell Hybrid Power Systems

Kyung Won Suh

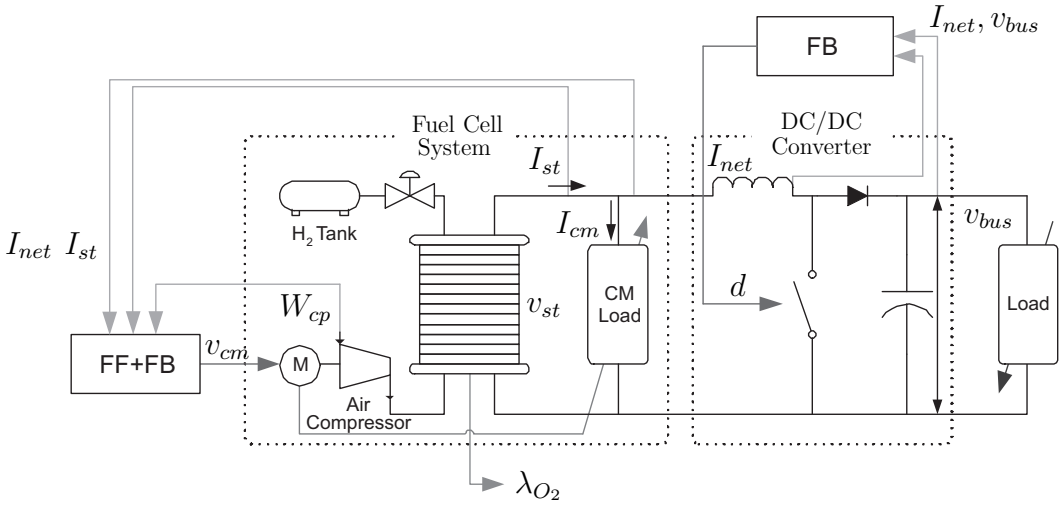

Modeling, Analysis and Control of Fuel Cell Electric Hybrid Power Systems

by

Kyung Won Suh

Chair: Anna G. Stefanopoulou

Transient performance is a key characteristic of fuel cells, that is sometimes more critical than efficiency, due to the importance of accepting unpredictable electric loads. To fulfill the transient requirement in vehicle propulsion and portable fuel cell applications, a fuel cell stack is typically coupled with a battery through a DC/DC converter to form a hybrid power system. Although many power management strategies already exist, they all rely on low level controllers that realize the power split. In this dissertation we design controllers that realize various power split strategies by directly manipulating physical actuators (low level commands). We maintain the causality of the electric dynamics (voltage and current) and investigate how the electric architecture affects the hybridization level and the power management.

We first establish the performance limitations associated with a stand-alone and power-autonomous fuel cell system that is not supplemented by an additional energy storage and powers all its auxiliary components by itself. Specifically, we examine the transient performance in fuel cell power delivery as it is limited by the air supplied by a compressor driven by the fuel cell itself. The performance limitations arise from the intrinsic coupling in the fluid and electrical domain between the compressor and the fuel cell stack. Feedforward and feedback control strategies are used to demonstrate these limitations analytically and with simulations. Experimental tests on a small commercial fuel cell auxiliary power unit (APU) confirm the dynamics and the identified limitations.

The dynamics associated with the integration of a fuel cell system and a DC/DC converter is then investigated. Decentralized and fully centralized (using linear quadratic techniques) controllers are designed to regulate the power system voltage and to prevent fuel cell oxygen starvation. Regulating these two performance variables is a difficult task and requires a compromise due to the conflicting objectives. The compromise can be mitigated by augmenting the fuel cell power system with an energy buffer such as a battery. We consider two different and popular ways of connecting the battery and the fuel cell to the load and we refer to them as electric architectures. Various controller gains are used to span the fuel cell operation from load-following to load-leveling, and hence, to determine adequate fuel cell-battery sizing (hybridization level) and the associated trends in the system efficiency.

Contents

List of Figures

List of Tables

Chapter 1

Introduction

Hydrogen is considered as one of the best alternative fuels for augmenting fossil fuels due to high net energy density[1] and its potential for zero local pollution. Proton exchange membrane (PEM), also known as polymer electrolyte membrane fuel cells (FCs) use hydrogen and are considered for vehicular power and portable applications because of high efficiency, low operating temperature, and simplicity in construction. The PEM fuel cells employ hydrogen and oxygen from the air to produce electricity, water and heat. In PEM FC, hydrogen and air are supplied to the inlet manifolds and flow fields, and then diffuse through porous media to the polymer membrane. The membrane in the middle of the cell contains catalyst layers, one in anode and the other in cathode. The catalyst layer at the anode separates hydrogen molecules into protons and electrons. The membrane permits transfer of protons, enabling the electrons to flow through an external circuit before recombining with protons and oxygen at the cathode to form water. This migration of electrons produces electricity. The anode and cathode reactions in PEM fuel cells are shown below

$$\begin{aligned} \text{Anode reaction} \quad & \mathrm{H_2} \longrightarrow 2\mathrm{H^+} + 2e^- \\ \text{Cathode reaction} \quad & \frac{1}{2}\mathrm{O_2} + 2\mathrm{H^+} + 2e^- \longrightarrow \mathrm{H_2O}. \end{aligned}$$

The electrical characteristics of fuel cells are normally given in the form of a polarization curve which is a relation of cell voltage versus cell current density (current per unit cell active area). The cell voltage varies from the ideal voltage of about 1.2 V to usually below 1 V. Stack temperature and membrane water content affect the fuel cell voltage, as do reactant pressures and flows. The voltage decreases as more current is drawn from the fuel cell, due to fuel cell electrical resistance, inefficient reactant gas transport, and low reaction rate. Lower voltage indicates lower efficiency of the fuel cell. The loss in the cell turns into heat which can damage the polymer membrane. Many cells are typically combined in a stack to satisfy the power requirements of the targetted application.

Various power applications impose stringent requirements on the transient performance of PEM

[1]Net energy density (including average engin/motor efficiency) for diesel is 3.2 kWh/kg, for gasoline 2.8 kWh/kg and hydrogen 2.0 kWh/kg [30].

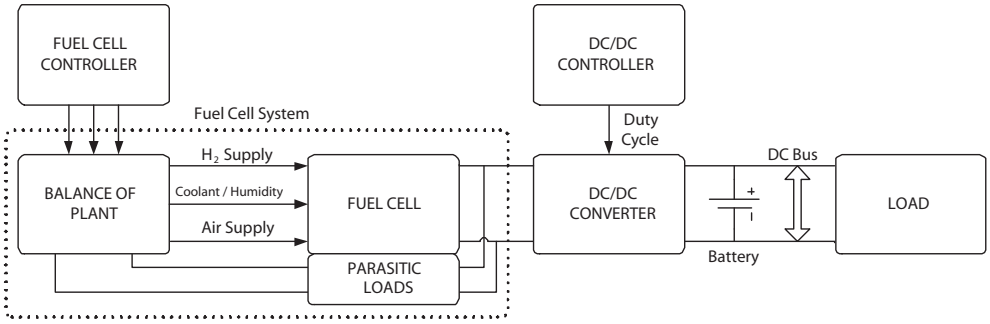

Figure 1.1: Configuration of a typical fuel cell hybrid power system

fuel cells. Transient response is a key characteristic feature of backup power system, sometimes more critical than efficiency, due to the importance of accepting rapidly changing, uncertain electric loads. Fast transient response is also essential for autonomy in start-up and fast power response. For these reasons, every fuel cell power system is expected to produce power on demand, also known as, a load-following fuel cell. Fuel cell response, however, is known to be limited by the complex dynamics associated with mass and heat balances inside and outside the stack. To address these limitations, a PEM fuel cell system is typically combined with a battery or capacitor into a hybrid power generation system. In this work, we concentrate on the FC limitations imposed by the air flow supply control. The FC performance objective is to avoid or reduce oxygen starvation during transient loading.

1.1 Background

The PEM fuel cell system for portable, stationary and automotive propulsion power applications requires both performance and reliability. The overall system should function with a high degree of reliability under a wide range of conditions, leading to a robust fuel cell system based on the system integration and control. A complete PEM fuel cell hybrid power system includes several components apart from the fuel cell stack and battery, such as an air delivery system which supplies oxygen using a compressor or a blower, a hydrogen delivery system using pressurized gas storage or reformer, a thermal and water management system that handles temperature and humidity, DC/DC converters to condition the output voltage and/or current of the stack and finally electric loads [57, 71]. Figure 1.1 shows the configuration of a typical fuel cell hybrid power system which is constructed with fuel cell, DC/DC converter and battery.

The control of a PEM fuel cell mainly consists of reactant supply, water/temperature, and power management as can be seen in Figure 1.1. Lack of robustness in control can cause cross-coupled failures during dynamic load changes in fuel cell system. Proton exchange membrane fuel cells, when operating with low air flow to minimize parasitic loss associated with powering the flow device, are prone to oxidant starvation during dynamic load changes even with optimized flow field design. The temporarily low oxidant stoichiometry produces cell voltage drop, resulting in local temperature

increase. Insufficient gas flow associated with dynamic load may cause accumulation of excess water, possibly blocking reactant diffusion. Anomalous operating conditions can cause not only reversible performance decrease but irreversible degradation [40, 61].

Hybridization in various electric power configurations with the fuel cell stack, DC/DC converter and battery offers flexibility in managing the power demand from the fuel cell, and thus protects the FC from transient loading [57]. For instance, a load-following fuel cell supplies the majority of power to the load with a small energy buffer responsible for parasitic losses or start-up procedures [21]. In a load-leveling fuel cell hybrid system, the battery complements the fuel cell power during transient loading. Hybridization in the fuel cell power system may protect the fuel cell from harmful transition and in addition may achieve higher fuel cell efficiency by leveling peak power demand from the FC.

The DC/DC converter is a key component for the hybridization. It is a power electric device that transforms unregulated DC power to regulated DC bus power in the hybrid configuration. The DC/DC converter is mostly dedicated to regulate the output voltage, masking the voltage variation of the fuel cell stack. The wide FC voltage imposes difficulties in efficiency and reliability. Typically less knowledge of the fuel cell dynamics forces the use of secondary energy storage such as battery or ultracapacitor for transient response [50]. Then DC/DC converter can be a current limiter or a filter for fuel cells to avoid transients that can lead to FC failure or degradation. In this case, the difference between load power demand and fuel cell power is covered by the other energy sources. Although splitting the power is an obvious way of explaining the operation of a hybrid system, dynamic interaction arises among fuel cells, power electronics devices and battery. Specifically, the coupled dynamics of current and voltage in the fuel cell and the DC/DC converter affect the system performance.

The stationary fuel cell power that is tied to an external grid can provide a certain amount of constant power, while other power sources on the grid will supply additional power that meets a transient response. This approach leads to the idea of load-leveling with a constant load to the fuel cell [5]. This is possible to the power conversion units. Namely, the DC/DC converter and DC/AC inverter can operate in nearly constant power, enabling constant load to the fuel cells. Another example of FC load-leveling is found when fuel cells are used in communication and computer products. For example, the electric load of radio communication can be characterized as randomly applied specific pulses with a constant power load [36]. In this configuration, active control of the fuel cell components is not necessary because battery power covers the most transients. The load to the stack is mostly constant power and slowly varying battery charging load. The control of the DC/DC converter is concentrated on the battery charging/discharging [34]. In these cases, the reactant supply system and other fuel cell conditioning units are optimally designed for the specific power and dynamic aspects in the balance of plant for the fuel cells can be neglected.

The fuel cells for an auxiliary power unit (APU) or vehicle propulsion require dynamic power over wide range even though battery or ultracapacitor is combined. The performance analysis of the FC hybrid system is mostly based on specific load profiles. For example, the specific APU load profile is presented with passively controlled hybrid fuel cell with a battery in [27]. Various electric loads

for tactical truck, although mostly for randomly processed pulse load, are discussed in [17]. The vehicle propulsion load is derived from specific driving cycles such as federal urban driving schedule and US06 [21, 45]. However, these analysis results are mostly based on non-causal modeling, thus being incapable of predicting dynamic interaction among the hybrid system components.

1.2 Literature review

To fulfill the performance requirement in vehicle propulsion and portable fuel cell applications, a fuel cell stack is typically coupled with a battery through a DC/DC converter to form a hybrid power system. Defining the fuel cell performance and identifying the limitation are critical in designing fuel cell hybrid power applications. Otherwise, unnecessary protection with conservative FC operation may results in lower overall efficiency. However, FC system identification and performance validation outside the safe limits might cause stack degradation or failure. Therefore, physics-based model is necessary in designing a FC hybrid power system.

The fuel cell model developed in the literature can be classified into two main categories, namely, microscopic and macroscopic model. The microscopic model deals with performance of the local area in the cell. For example, the FC model predicts spatial distribution of current density [66]. Due to computational load, the microscopic model is not suitable in system integration studies. The macroscopic model is generally defined by global pressure, temperature and flow conditions. The electrochemical reactions are considered instantaneous [1]. Recent research also shows a lot of results in modeling the transient behavior of fuel cells based on reactants supply dynamics [52], temperature dynamics [3] and humidity [70]. Amphlett *et al.* [3] showed the temperature dynamics of fuel cells. Wang *et al.* [70] also presented that the fuel cell dynamics associated with humidity exhibit a time constant that is far slower than the ones of reactants supply even though humidity has direct effect on the membrane conductivity and thus internal resistance. Transient power performance is highly related with the reactant pressure and flow dynamics [60]. Modeling and control of the air supply that can respond to transient load is emphasized in [52].

The past models consider exogenous input to interface the FC with the external power demand. In most fuel cell models, exogenous input is current and the resulting output is either cell or stack voltage [1, 52, 60]. Rarely voltage is defined as the input load [66]. Independently from the input, the internal dynamics of the FC follow the same physical principles.

Performance limitations due to the air supply in PEM FC have been reported previously. Regulating air flow based on the flow rate measurement at the supply manifold inlet introduces a limitation because the actual air flow at the cathode inlet is not the same as the one at the compressor outlet [48, 52, 60]. This mismatch introduces a significant complexity in tuning the air flow controller for the actual in-stack performance objective. On the other hand, high compressor control effort, which draws current directly from the stack, can cause instabilities in the FC power delivery system [49]. Two performance variables, air flow and cathode pressure, become both critical to the fuel cell performance and the system efficiency [4, 46]. Note that the hydrogen supply is more

important than the air supply when reformer is used due to the slow dynamics of the reformer [55].

The integration and associated dynamics of the fuel cells in the hybrid power system depend highly on the electric architecture and specific load conditions. Various electric connections between the fuel cell and battery have been proposed in literature. Parallel connection between the fuel cell and the battery with the electric load without any DC/DC converter is originally proposed for submarine applications [2]. Although parallel connection does not provide active control in power management, this design provides a first-order RC (resistor-capacitor) filter to the fuel cell stack [50]. This way, the battery can cover the transient power demand. However, this passive connection limits the fuel cell stack and battery size and imposes constraints in their operation, and hence, performance [27].

The DC/DC converter isolates the voltage range of the fuel cell from the battery, offering more flexibility and the potential for optimized performance. Hence a DC/DC converter is almost always considered in FC hybrid system studies. A large number of studies on the DC/DC converters for fuel cells is focused on soft voltage sources, which accounts for the cell voltage variation due to the electrochemical characteristic at different operation conditions [67]. There is another functionality, however, that a DC/DC converter has to perform. The DC/DC converter in FC hybrid system handles power split and active fuel cell management. The operation principles of power split in FC hybrid vehicle power are well summarized in [57]. In the same paper, several electric architectures are presented with signal flows associated to interacting current and voltage, pointing to the lack of appropriate dynamic model for analysis and control design.

Since the control bandwidth of the DC/DC converter is faster than any other dynamics in the FC, battery and electric load, the DC/DC converter is sometimes modeled as static conversion of power. Based on quasi-steady state assumption, noncausal optimization methods have been used to evaluate the supervisory control in energy storage and regenerative braking strategies [13, 39, 58, 59, 64].

Most hybrid strategies associated with fuel cell applications mainly focus on protection of the FC stack. Therefore the control command to the DC/DC converter is determined by the fuel cell system. To prevent abrupt changes in current load to the fuel cell, first-order current load filter is proposed in [29]. Load governors [63, 68] and model predictive control [69] have been also proposed for current control. The control objective of the DC/DC converter varies with the specification of the electric loads. The duty cycle control of the DC/DC converter is proposed for the purpose of maintaining battery stage of charge [34]. Two different DC/DC converters are proposed with its own control objective, namely, fuel cell objective and power bus objective [44]. Specifically, conventional DC/DC converter manages the current drawn from the fuel cell based on a supervisory control command, whereas a bidirectional DC/DC converter draws power from the battery to maintain the DC bus voltage. The small volume and weight of a bidirectional DC/DC converter make it lucrative for FC hybrid vehicle [18]. The bidirectional DC/DC converter controls fuel cell voltage instead of current load [37].

In most of FC hybrid power studies, the fuel cell stack is modeled with a static polarization relationship assuming fixed fuel cell operating parameters and avoiding the dynamical variations.

Thus, the major objective of protecting the fuel cell from harmful transition cannot be evaluated.

1.3 Thesis overview

This dissertation focuses on the fuel cell hybrid power system which is composed of active control in oxidant air supply, DC/DC converter and battery. Control challenges arise with a highly dynamic electric load applied to the fuel cell hybrid power system. To define achievable performance and limitations of the FC system, modeling and analysis of the electric architectures for FC hybrid power system combining fuel cell system, DC/DC converter and battery are presented.

Control of energy conversion from the chemical energy of hydrogen to the electric energy results electron flows from the fuel cell stack to the load. On the electric load side, the flow of electrons is considered as the current, producing electric power. On the other hand, flow of electrons in the fuel cell is equivalent to the reaction of hydrogen and oxygen molecules that is supported by the reactant supply system. Thus current and reactant flow are considered in the same domain, and the current drawn to the load and the reactants supplied to fuel cell need to be precisely controlled.

The electrically connected FC and compressor allow us to design a realistic air delivery controller for regulating the oxygen excess ratio and to capture the FC performance limitation during abrupt changes in the current drawn (load) from the fuel cell. The electric load in FC system is controlled by DC/DC converter following certain objectives, for instance, regulating bus voltage or charging/discharging battery. The interaction and tradeoff between generating the electric power on demand and protecting the stack in dynamic load are examined. Model-based control design is performed to regulate both the air supply into the FC and the voltage/current of the DC/DC converter and the battery.

1.3.1 Control of power-autonomous fuel cell system

In PEM fuel cell application, dynamic performance in the range of 0.1-1 second mainly depends on the air supply sub-system [12]. In the case of pressurized pure hydrogen supply, oxygen kinetics and mass transport become the limiting dynamic factor. Excluding start-up and shut down periods, the transient response associated with controlling air and avoiding oxygen starvation is an improtant factor in PEM fuel cell system.

In Chapter 2, a low-order fuel cell system model with reactants supply dynamics is presented, following and extending the work in [52]. Fuel cell stack and reactant flow model is based on electrochemistry, mass balances for lumped volumes in the stack and auxiliary, and rotational dynamics of compressor and motor. It is assumed that the fuel cell stack is conditioned to be in desirable operating range of temperature and humidity using thermal and water management system. The temperature and humidity dynamics are in general slower than the pressure, flow, voltage and current dynamics observed during power transient [6]. The effect of transient dynamic response of electrochemical double-layer discharging in the stack is sufficiently short to be safely ignored [42]. The simulation comparisons in Section 2.2 confirms the developed low-order model accurately predicts

the air dynamics in the fuel cell stack system including the flow coupling among the air compressor, manifolds, volumes and nozzles.

The importance of the air delivery system in PEM fuel cell is recognized with several limitations on air supply control repeatedly reported in [48, 49, 52, 60]. The significance of the air management arises due to its considerable parasitic losses [12]. The compressor power affects the net power of the fuel cell significantly. For example, the air supply compressor load consumes up to 14% of stack power [11].

In Chapter 3, we introduce another important aspect of air flow control, namely, the electric coupling between the air supply compressor and the fuel cell when the compressor motor is driven by the stack power and connected directly on the fuel cell stack voltage bus. A compressor driven directly by the fuel cell bus voltage (before the DC/DC converter in Figure 1.1) introduces another limitation to the fuel cell operation. The effect of the compressor power is simple subtracted by the fuel cell power in order to calculate the net power in [53]. In Section 3.1, we connect the compressor motor directly to the stack so that compressor driving current is a portion of the stack current. Thus the stack performance is affected by the air supply control through the current drawn by the compressor. In Section 3.3, it is shown that the oxidant air supply, consists of air compressor/motor and flow manifold, in FC system has inherent limitations on the control of air flow to the stack with respect to dynamic current load due to the non-minimum phase zeros. The analysis results show us fundamental design limitations on both feedforward and feedback controller in Section 3.4 and 3.5. The electric coupling and the effects on fuel cell system performance due to parasitic losses are qualitatively confirmed with an experimental setup of a commercial fuel cell stack system in Chapter 4.

1.3.2 Fuel cell power management

Although hybridization of a fuel cell system mainly focuses on protection of the FC stack, the study of FC system efficiency is also raised [33]. The anticipated benefits of hybridization for fuel cell vehicle differ from those for internal combustion engine (ICE) vehicle. Hybridization in ICE vehicle enables the decoupling of the instantaneous torque and speed demands from the wheels, and in this way, it enforces the optimum engine operation. The fuel cell hybrid electric vehicle, on the other hand, has high efficiency at wide range of power levels so it is not clear if hybridization increases efficiency in any significant manner to justify the increase in weight and complexity associated with the addition of the batteries.

The efficiency of fuel cells is generally calculated by the produced electric energy as the output and heating value of hydrogen as the input [42]. The cell voltage also can be used as indication of the fuel cell efficiency. However, battery efficiency cannot be calculated directly because the losses in battery during charging-discharging are varying with current. Total vehicle level efficiency can be compared through the consumed hydrogen fuel during specific driving cycles [59].

On the other hand, efficiency of fuel cells and battery can be interpreted with internal resistance which can be assumed to be static or dynamic impedance following the paradigm of electric circuits.

The overall efficiency of a hybrid fuel cell power system without regenerative braking is expected to be improved by adding battery when the demanded current is drawn from the power source which has smaller internal resistance. Otherwise the overall efficiency of the system becomes lower even when the fuel cell is at its optimal operating condition. For example, the fuel cell impedance in an automotive size stack varies from 0.05 to 0.3 Ω [54] in certain operating point and the internal resistance of high voltage battery pack for fuel cell hybrid vehicle is about 0.3 to 0.4 Ω [35, 51]. In this case, using the energy in battery that is charged from the fuel cells is obviously inefficient. Note here that the loss due to the current drawn from a battery should be calculated twice because there is charging and discharging losses to maintain the battery state of charge. Of course this comparison is not valid for transient operation, but it raises several questions about the overall efficiency of hybridization in PEM fuel cells.

The regenerative braking helps capture and reuse the energy improving fuel economy. Indeed a battery-hybrid fuel cell vehicle equipped with regenerative braking improves efficiency up to 15% [13]. The efficiency gain in a fuel cell hybrid vehicle depends on the hybridization level or the degree of hybridization [33]. The hybrid system efficiency can be worse than the stand-alone fuel cell in some driving cycles [21, 58, 64]. Also, efficiency of a hybridized auxiliary power unit (APU) or distributed power generation, which has no energy recovery apparatus like regenerative braking, is not yet addressed.

These unexplored issues highlight the importance of defining the achievable performance and limitation of a fuel cell power system before hybridization. Hybridization in fuel cell power system is achieved through filtering the current from the fuel cells to avoid imposing transients that can lead to FC failure or degrade its life. This conservative approach may lead to unnecessarily lower overall efficiency. Therefore our goal in Chapter 5 is to first examine the capability and limitation of fuel cell power system first before adding secondary power source such as battery or capacitor. In Section 5.1, the dynamic behavior of voltages and currents between the input source and the output load of the DC/DC converter is explained by a simple transient model. The actual converter operates by switching pulse devices, but it is approximated here by an average model that captures transient dynamics within the bandwidth of the switching frequency.

In the controller design stage presented in Section 5.2, the DC/DC converter controller is treated separately from the fuel cell controller and is responsible for meeting the fuel cell requirement during power transient. In other words, the boost converter controller is first designed for the best performance, and then in Section 5.2.1 each controller is re-tuned sequentially in favor of the other because there is a direct conflict between the performance objectives of the fuel cell and the converter. Specifically, limiting the current drawn from the fuel cell with DC/DC converter enhances fuel cell performance but degrades the voltage regulation performance in DC/DC converter. In Section 5.2.2 we introduce coordination in a combined system controller with optimal gains. The coordinated control accounts for the interactions between the two systems and allows us to construct a controller for the optimum performance. The result of the dynamic model analysis and control study in this work provides the insight on the fundamental system controllability and limitations in handling

transient load in a fuel cell power system.

1.3.3 Electric configuration of FC hybrid power

Managing the power split between the fuel cell and the battery in a hybrid system depends on the connection of the FC with the battery. We refer to the various configurations of connecting the fuel cell and the battery as electric architectures. There are several electrical configurations that have been considered for hybrid (FC and battery/ultracapacitor) systems [57, 67].

Figure 1.2(a) shows a typical load-sharing or load-leveling fuel cell hybrid vehicle configuration that extends FC power using the high voltage battery. The DC/DC converter boosts the stack voltage of the FC to the battery voltage, drawing the current from the stack. The battery current supplements the FC current in order to satisfy the power demand. In automotive propulsion application, regenerative braking is used to charge battery. The DC/DC converter control problem gets simplified when a high voltage battery is connected in parallel between the DC/DC converter and the load. The battery supports the main electric bus voltage, and the duty cycle of the DC/DC converter controls the current drawn from the fuel cell.

Direct-hydrogen PEM fuel cell system can be used as load-following power source for various applications. Load-following FC without high power buffer battery is already applied to the vehicle propulsion [24]. The purpose of the electric architecture in the hybrid fuel cell power system in Figure 1.2(b) is to avoid large-size batteries and to meet the electric load mostly with the fuel cell. In configuration (b), the major power flows from the FC to the load directly without DC/DC converter. A small amount of battery current flows through the bidirectional DC/DC converter during charging/discharging. This configuration can be more efficient than configuration in Figure 1.2(a) because it avoids the DC/DC converter losses and weight. However it relies more than configuration (a) on the ability of the FC to follow the load demands. In any FC electric hybrid configuration, the coupled dynamics of currents and voltages in fuel cells and DC/DC converter will affect the overall dynamics and ultimately dictate the final control calibration independently of steady-state efficiency.

The dynamic coupling between the voltages and currents among the fuel cell, battery and the traction load is captured in Chapter 6. A converter controller is then designed to boost and regulate the voltage at the converter output. Good regulation of the voltage at the converter output is typically achieved by large current drawn from the fuel cell and it is typically followed by small currents drawn from the battery. The converter controller can be tuned to avoid causing abrupt current draw from the fuel cell. In Section 6.2, various DC/DC converter controller gains result in different levels of power split between the fuel cell and the battery, spanning load-following to load-leveling. It is thus possible to assess the effects of control calibrations on the power split, FC oxygen excess ratio, compressor behavior, and vehicle efficiency.

In Section 6.3, we introduce coordination between the bidirectional DC/DC converter and the FC into a combined system in the electric hybrid configuration of Figure 1.2(b). To address the control of the FC hybrid system, a fuel cell model with voltage input is applied. The bidirectional

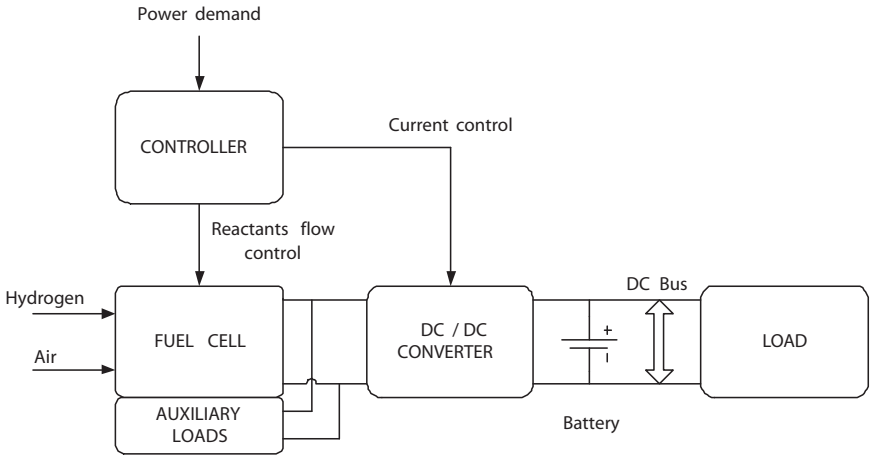

(a) FC+DC/DC converter with a high voltage battery

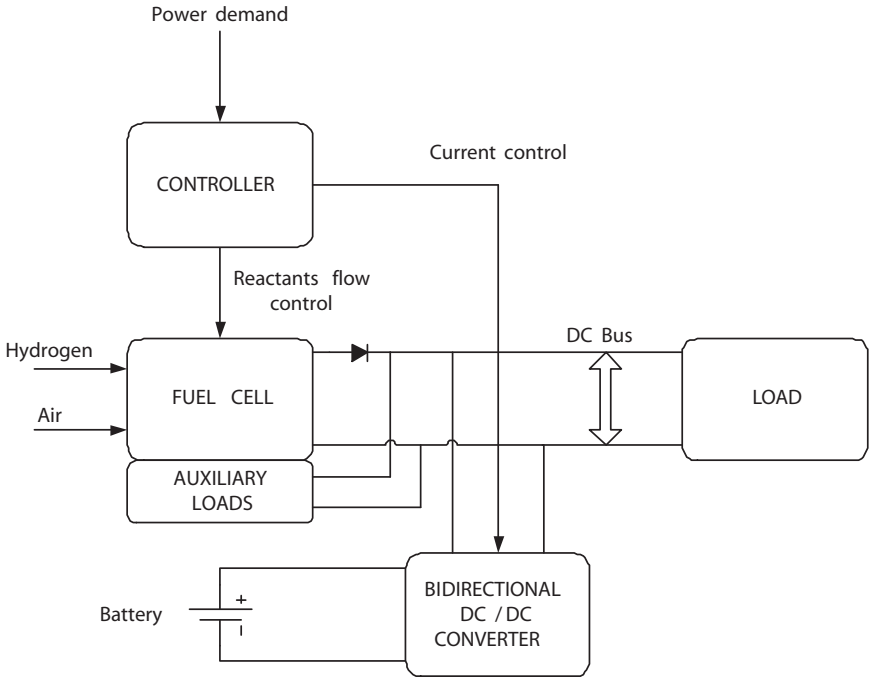

(b) FC directly connected to the load with bidirectional converter+battery

Figure 1.2: Electric configurations for fuel cell hybrid power system

DC/DC converter control with optimal gains emulates the FC load-following power split scenario as in Section 6.2, but with smaller-size battery. The control design accounts for the limitations in the fuel cell system and allows us to construct a controller for the smallest possible power assist level without compromising the fuel cell operation. The results of fuel economy and battery sizing with the dynamic model and control in this work provide insight on the necessary hybridization of a fuel cell power system without employing cycle-dependent optimization.

1.4 Contributions

System-level design is not only valuable design tool, but also the key to successful FC applications. While the PEM FC system has been studied from different disciplinary perspectives as we have reviewed in literature, the interdisciplinary features of fuel cell systems have remained unexamined. In this dissertation, fuel cell system is explained on multidisciplinary basis, connecting the weakest link between the fuel cells' own dynamics and power electronics with modeling and control design. The electric architecture and configuration study in this work provides a comprehensive approach to evaluating the control performances in fuel cell hybrid power.

The major contributions of the dissertation are as follows.

- A simple but accurate, low-order FC system model has been developed to describe the dynamic performances, which is adequate to apply in hybrid power system analysis. Control design limitations of a power-autonomous fuel cell system in air supply arise when the air supply compressor is powered directly from the FC. The coupling between the power and flow paths through a compressor driven fuel cell stack is clarified. It is shown that the inherent design limitations due to the non-minimum phase zeros dictate the performance of the system. A control strategy combining feedback and feedforward controller is proposed and used to demonstrate those limitations in the FC air supply in simulations.

- The direct conflict between FC oxygen excess ratio and the output voltage of the DC/DC converter is elucidated when the FC is augmented with a DC/DC converter to form a stand-alone power generation. A model-based controller is designed to achieve the two performance objectives using decentralized control and compared with multivariable control architectures. An average continuous-in-time modeling approach that approximates the converter switching dynamics is applied. It is shown that coordination between the air compressor and the converter controllers provides a small improvement over a decentralized controller.

- The control coordination in the fuel cell system and DC/DC converter is expanded to the applications in FC-battery hybrid system in light of the two configurations in Figure 1.2.

  - The control problem is reformulated for FC power system with a battery connected directly to the high voltage DC bus. It is shown that adding a secondary power source mitigates the tradeoffs between the FC and the DC/DC converter, while another tradeoff

between the FC and the battery performance arises. Controller design is performed for the FC-battery hybrid system to define the hybridization level. It is shown that the model developed for FC hybrid power application is capable of evaluating the system efficiency as well as transient performances.

– The controller design of FC hybrid with low voltage battery is performed. The controllability and performance limitation are revisited for minimum size of battery. It is shown that a small battery achieves adequate load buffering without compromising the fuel cell protection and system efficiency.

Chapter 2

PEM fuel cell system model

We first develop a phenomenological model of the PEM fuel cell stack, mainly focusing on air supply dynamics. The fuel cell stack and reactant flow models are based on electrochemistry, mass balances for lumped volumes in the stack and peripheral volumes, and rotational dynamics of compressor and motor. Electrochemical models are basically developed for the relation between equilibrium cell voltage versus current density of the cell. The empirical equations have been established for cell voltage of PEM fuel cells from electrochemical theory and experiments [1]. The results presented the steady-state voltage-current relation for a particular set of operating conditions include reactant gas concentration, pressures and operating current.

In a dynamic model for fuel cell voltage and current, the reactants supply has an important role in fuel cell performance because characteristics of PEM fuel cells are dominated by kinetics of hydrogen and oxygen. To concentrate on air (oxygen) dynamics of the fuel cell system, we assume that the fuel cell system is fed by pressurized high-purity hydrogen and the hydrogen supply control is perfect for tracking the anode pressure to the cathode pressure.

We also neglect humidity and temperature dynamics because they are slower than the air flow dynamics. The temperature and humidity dynamics in fuel cells are slower than the dynamics observed during fuel cell power changes which are the condition we focused in the study. Temperature and humidity models are developed with heat and mass balance equations in fuel cells. However, fast transient in temperature humidity excursion do not occur within the dynamics of transient power [3, 70]. Additional considerations associated with controlling the system humidity and temperature depending on the operational pressure are still under debate [22]. To concentrate on the dynamics of the air supply, the humidity and temperature of the fuel cell stack is assumed to be controlled perfectly by dedicated hardware and controller.

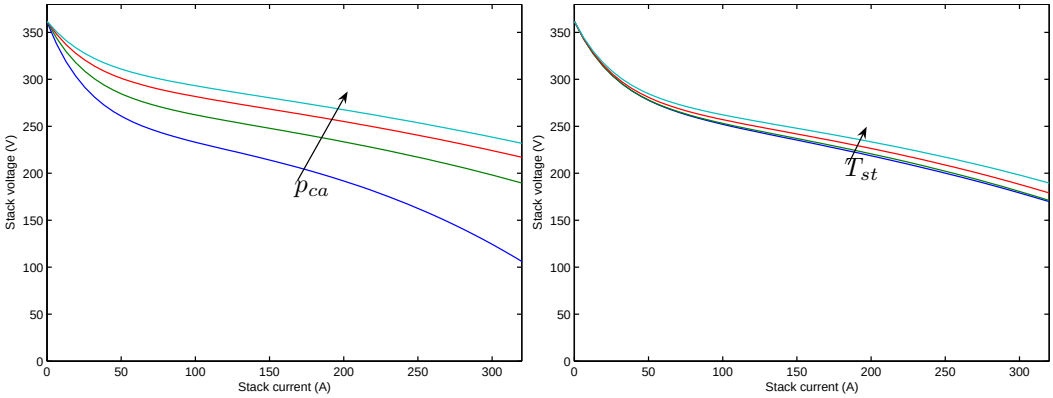

(a) p_{ca} = 1 bar, 2 bar, 3 bar, 4 bar (b) T_{st} = 20℃, 40℃, 60℃, 80℃

Figure 2.1: Stack polarization

2.1 Fuel cell system model

We consider a fuel cell stack with active cell area of $A_{fc} = 280$ cm^2 and $n = 381$ number of cells with 75 kW gross power output that is applicable for automotive and residential use. The performance variables for the FC power system are (i) the stack voltage v_{st} that directly influences the stack power generated, $P_{fc} = v_{st}I_{st}$, when the load current I_{st} is drawn from the stack, and (ii) the oxygen excess ratio λ_{O_2} in the cathode that indirectly ensures adequate oxygen supply to the stack.

Stack voltage is calculated as the product of the number of cells and cell voltage $v_{st} = nv_{fc}$. The combined effect of thermodynamics, kinetics, and ohmic resistance determines the output voltage of the cell, as defined by

$$v_{fc} = E - v_{act} - v_{ohm} - v_{conc} \tag{2.1}$$

where E is the open circuit voltage, v_{act} is the activation loss, v_{ohm} is the ohmic loss, and v_{conc} is the concentration loss. The detailed formulation of the FC voltage, also known as, polarization characteristic can be found in [52].

In steady state, FC voltage is given as static function of current density $i_{fc} = I_{st}/A_{fc}$ and several other variables such as oxygen and hydrogen partial pressures p_{O_2} and p_{H_2}, cathode pressure p_{ca}, temperature T_{st} and humidity λ_m. Although we assume instantaneous electrochemical reaction and negligible electrode double layer capacity, the FC voltage has a rich dynamic behavior due to its dependance on dynamically varying stack variables $(p_{O_2}, p_{ca}, p_{H_2}, T_{st}, \lambda_m)$. Figure 2.1 shows examples of the stack polarization with different cathode pressure and stack temperature conditions. In this thesis, we assume compressed hydrogen supply as shown in Figure 2.2, which simplifies the control of anode reactant flow. We also assume that the stack temperature and humidity is controlled accurately and with negligible lag. The cooler and humidifier are neglected for this work because their power requirement are smaller than the compressor power [8].

In this study, we concentrate on the dynamic behavior of the variables associated with the air

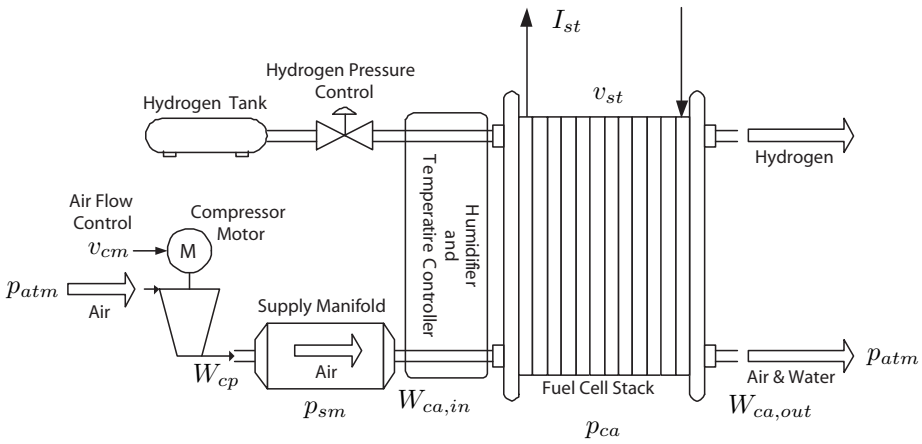

Figure 2.2: Fuel cell reactant supply system

flow control, namely, oxygen pressure p_{O_2}, total cathode pressure p_{ca}, and oxygen excess ratio in the cathode λ_{O_2}, which is a lumped parameter that indicates the amount of oxygen supplied versus oxygen consumed. All variables associated with the air supply and the stack performances are defined in the following sections. The transient voltage excursions in the stack are minimized with precise control of reactants. However, the flow dynamics of the oxygen and hydrogen reactants are governed by pressure dynamics through flow channels, manifolds and orifices. Also, fuel cells are required to have an excessive amount of oxygen and hydrogen flow into the stack to avoid stagnant vapor and nitrogen films covering the electrochemical area.

Depending on the load (current) drawn from the fuel cell and the air supply to the fuel cell, the stack voltage varies between 220 V to 350 V. The air is supplied by a compressor that is driven by a motor with maximum power of 15 kW. At its maximum rotational speed of 100 kRPM the compressor provides 95 g/sec of air flow and generates a pressure increase of 3.5 atm. The maximum compressor air flow is twice the air flow necessary to replenish the oxygen consumed from the stack when the maximum current is drawn $I_{st,max} = 320$ A. The maximum FC current is defined as the current at which the maximum FC power is achieved. Drawing more current from the fuel cell results in rapid decrease of the stack voltage, and thus power due to concentration losses [42].

2.1.1 Dynamic states

Details of the model used in this study can be found in [52, 54]. Several simplifications and modifications have been employed to allow us to concentrate on the fast dynamics associated with the integration of a fuel cell with a DC/DC converter, by mainly focusing on the air dynamics. Specifically, the following assumptions are made: (i) All gases obey the ideal gas law; (ii) The temperature of the air inside the cathode is equal to the bulk stack temperature which is, in turn, equal to the temperature of the coolant exiting the stack; (iii) The properties of the flow exiting the cathode such as temperature and pressure are assumed to be the same as those inside the cathode and are the

ones that dominate the reaction at the catalyst layers in the membrane; (iv) The gases in the anode and cathode are fully humidified and the water inside the cathode is only in vapor phase assuming any extra water turns to liquid and is removed from the channels; (v) We neglect flooding of the gas diffusion layer; (vi) Finally, the flow channel and the gas diffusion layer are lumped into one volume, i.e., the spatial variations are neglected. Note here that all these assumptions are made to isolate the potential problems associated with non-hybridized load-following fuel cell that supports its external and auxiliary loads through its bus. By assuming perfect humidity and temperature regulation, we do not wish to underestimate their importance nor the challenges associated with the specific control task. We present the model dynamic states first and then in Section 2.1.2, we describe the nonlinear relationships that connect the inputs with the states and the outputs (performance variables and measurements for control).

The mass continuity of the oxygen and nitrogen inside the cathode volume and ideal gas law yield

$$\frac{dp_{O_2}}{dt} = \frac{\bar{R}T_{st}}{M_{O_2}V_{ca}}\left(W_{O_2,in} - W_{O_2,out} - W_{O_2,rct}\right), \tag{2.2}$$

$$\frac{dp_{N_2}}{dt} = \frac{\bar{R}T_{st}}{M_{N_2}V_{ca}}\left(W_{N_2,in} - W_{N_2,out}\right) \tag{2.3}$$

where V_{ca} is the lumped volume of cathode, $\bar{R}$ is the universal gas constant, and M_{O_2} and M_{N_2} are the molar mass of oxygen and nitrogen, respectively.

The rate of change of air pressure in the supply manifold that connects the compressor with the fuel cell (shown in Figure 2.2) depends on the compressor flow into the supply manifold W_{cp}, the flow out of the supply manifold into the cathode $W_{ca,in}$ and the compressor flow temperature T_{cp}.

$$\frac{dp_{sm}}{dt} = \frac{\bar{R}T_{cp}}{M_{a,atm}V_{sm}}\left(W_{cp} - W_{ca,in}\right) \tag{2.4}$$

where V_{sm} is the supply manifold volume and $M_{a,atm}$ is the molar mass of atmospheric air.

The compressor motor state is associated with the rotational dynamics of the motor through thermodynamic equations. A lumped rotational inertia is used to describe the compressor with the compressor rotational speed ω_{cp}

$$\frac{d\omega_{cp}}{dt} = \frac{1}{J_{cp}}\left(\tau_{cm} - \tau_{cp}\right) \tag{2.5}$$

where τ_{cm} is the compressor motor torque and τ_{cp} is the load torque of the compressor.

2.1.2 Nonlinear static relations

The nonlinear relations that connect the dynamics states (pressure and rotational speed) through the right-hand side of equations (2.2) - (2.5) are described in this section.

The inlet mass flow rate of oxygen $W_{O_2,in}$ and nitrogen $W_{N_2,in}$ can be calculated from the inlet

cathode flow $W_{ca,in}$ as follows

$$W_{O_2,in} = \frac{x_{O_2,atm}}{1+w_{atm}} W_{ca,in}, \tag{2.6}$$

$$W_{N_2,in} = \frac{1-x_{O_2,atm}}{1+w_{atm}} W_{ca,in} \tag{2.7}$$

where $x_{O_2,atm}$ is the oxygen mass fraction of the inlet air

$$x_{O_2,atm} = \frac{y_{O_2,atm} M_{O_2}}{y_{O_2,atm} M_{O_2} + (1-y_{O_2,atm}) M_{N_2}} \tag{2.8}$$

with the oxygen molar ratio $y_{O_2,atm} = 0.21$ and the humidity ratio of inlet air

$$w_{atm} = \frac{M_v}{y_{O_2,atm} M_{O_2} + (1-y_{O_2,atm}) M_{N_2}} \frac{\phi_{atm} p_{sat}}{p_{atm} - \phi_{atm} p_{sat}} \tag{2.9}$$

where $p_{sat} = p_{sat}(T_{st})$ is vapor saturation pressure and ϕ_{atm} is the relative humidity at ambient conditions which is preset to the average value of 0.5.

The supply manifold model describes the mass flow rate from the compressor to the outlet mass flow. A linear flow-pressure condition is assumed for the flow calculation due to the small pressure difference between the supply manifold and the cathode

$$W_{ca,in} = k_{ca,in}(p_{sm} - p_{ca}) \tag{2.10}$$

where $k_{ca,in}$ is the supply manifold orifice flow constant and spatially invariant cathode pressure p_{ca} is the sum of oxygen, nitrogen and vapor partial pressures

$$p_{ca} = p_{O_2} + p_{N_2} + p_{sat}. \tag{2.11}$$

The rate of oxygen consumption $W_{O_2,rct}$ in (2.2) from the stack current I_{st} is given by

$$W_{O_2,rct} = M_{O_2} \frac{n I_{st}}{4F} \tag{2.12}$$

where n is the number of cells in the stack and F is the Faraday number.

The outlet mass flow rate of oxygen $W_{O_2,out}$ and nitrogen $W_{N_2,out}$ used in (2.2) and (2.3) are calculated from the mass fraction of oxygen and nitrogen in the stack after the reaction

$$W_{O_2,out} = \frac{M_{O_2} p_{O_2}}{M_{O_2} p_{O_2} + M_{N_2} p_{N_2} + M_v p_{sat}} W_{ca,out}, \tag{2.13}$$

$$W_{N_2,out} = \frac{M_{N_2} p_{N_2}}{M_{O_2} p_{O_2} + M_{N_2} p_{N_2} + M_v p_{sat}} W_{ca,out}. \tag{2.14}$$

The total flow rate at the cathode exit $W_{ca,out}$ is calculated by the nozzle flow equation [31] because the pressure difference between the cathode and the ambient pressure is large in pressurized stacks.

$$W_{ca,out} = \frac{C_D A_T p_{ca}}{\sqrt{\bar{R}T_{st}}} \left(\frac{p_{atm}}{p_{ca}}\right)^{\frac{1}{\gamma}} \left\{ \frac{2\gamma}{\gamma - 1} \left[1 - \left(\frac{p_{atm}}{p_{ca}}\right)^{\frac{\gamma-1}{\gamma}} \right] \right\}^{\frac{1}{2}} \quad \text{for} \quad \frac{p_{atm}}{p_{ca}} > \left(\frac{2}{\gamma+1}\right)^{\frac{\gamma}{\gamma-1}} \tag{2.15}$$

and

$$W_{ca,out} = \frac{C_D A_T p_{ca}}{\sqrt{\bar{R}T_{st}}} \gamma^{\frac{1}{2}} \left(\frac{2}{\gamma+1}\right)^{\frac{\gamma+1}{2(\gamma-1)}} \quad \text{for} \quad \frac{p_{atm}}{p_{ca}} \leq \left(\frac{2}{\gamma+1}\right)^{\frac{\gamma}{\gamma-1}} \tag{2.16}$$

where γ is the ratio of the specific heat capacities of the air, C_D is the discharge coefficient of the nozzle, A_T is the opening area of the nozzle.

The compressor flow W_{cp} is modeled by applying the Jensen and Kristensen nonlinear fitting method [52] as functions of the pressure ratio p_{sm}/p_{atm}, the upstream temperature T_{atm}, and the compressor rotational speed ω_{cp}. The temperature of the air leaving the compressor is modeled based on [52] with a map of the compressor efficiency η_{cp}

$$T_{cp} = T_{atm} + \frac{T_{atm}}{\eta_{cp}} \left[\left(\frac{p_{sm}}{p_{atm}}\right)^{\frac{\gamma-1}{\gamma}} - 1 \right]. \tag{2.17}$$

The compressor motor torque τ_{cm} is calculated assuming a simplified DC motor model with a static electromechanical relation of applied motor input voltage v_{cm} and back emf

$$\tau_{cm} = \eta_{cm} \frac{k_t}{R_{cm}} (v_{cm} - k_v \omega_{cp}) \tag{2.18}$$

where k_t, k_v, and R_{cm} are motor constants and η_{cm} is the motor mechanical efficiency. The assumption of a voltage-controlled DC motor instead of frequency/amplitude controlled AC motor implies instantaneous generation of motor torque (v_{cm} to τ_{cm} relationship), neglecting all the high frequency dynamics associated with more realistic and modern switching drive. Our assumption can be justified because the switching frequency of the drive and the motor flux dynamics are faster than the dynamics of the combined motor-compressor inertia in Equation (2.5). Even the implementation of a filter that minimizes the switching ripples preserves the highly dynamic (almost instantaneous) relationship between the motor control command (v_{cm} in our case) and the torque generation τ_{cm}. One will need to convert the voltage control command v_{cm} derived to current or frequency/amplitude control command when specific motor and drive design are specified. The torque consumed by the compressor is calculated from the thermodynamic equation

$$\tau_{cp} = \frac{C_p}{\omega_{cp}} \frac{T_{atm}}{\eta_{cp}} \left[\left(\frac{p_{sm}}{p_{atm}}\right)^{\frac{\gamma-1}{\gamma}} - 1 \right] W_{cp} \tag{2.19}$$

where C_p and correspond to the specific heat capacities of the air.

The compressor motor power P_{cm} provided by the compressor motor is calculated using the compressor motor voltage input v_{cm} and its rotational speed ω_{cp}

$$P_{cm} = \frac{v_{cm}}{R_{cm}}(v_{cm} - k_v\omega_{cp}). \tag{2.20}$$

This power can be supplied directly from the fuel cell or from an auxiliary power source.

We assume vapor is saturated in the anode without flooding or nitrogen diffusion. We also assume that the anode pressure is regulated to follow the cathode pressure. Controlled anode pressure can be achieved either with anode recirculation [38] or dead-ended anode outlet [52]. Based on these assumptions, the hydrogen pressure that affects the FC voltage is calculated

$$p_{an} = p_{ca}, \tag{2.21}$$

$$p_{H_2} = p_{an} - p_{sat}. \tag{2.22}$$

The oxygen excess ratio

$$\lambda_{O_2} = \frac{W_{O_2,in}}{W_{O_2,rct}} \tag{2.23}$$

corresponds to the ratio between the oxygen supplied and the oxygen reacted in the cathode. The oxygen excess ratio is typically regulated at $\lambda_{O_2}^{ref} = 2$ to reduce the formation of stagnant vapor and nitrogen films in the electrochemical area. Values of λ_{O_2} lower than 1 indicate oxygen starvation and has serious consequences in the stack life.

2.1.3 Input and output in the fuel cells

The nonlinear model based on the state equations (2.2)-(2.5) involves the four states

$$x = \begin{bmatrix} p_{O_2} & p_{N_2} & \omega_{cp} & p_{sm} \end{bmatrix}^T. \tag{2.24}$$

Given the four states, we can formulate state equations with the control actuator signal v_{cm}, and a exogenous input from the electric load outside.

Traditionally, the current have been chosen as an input in the fuel cell model. Thus Equation (2.1) produces the cell voltage v_{fc}, and the stack voltage v_{st} given the stack current I_{st} or current density i_{fc}. The input of the fuel cell model is actually the controlled electric load with external device and the choice of the electric load is depends on the applications. For example, the voltage of the cell can be an input of the fuel cells to analyze spatially distributed current density [66]. The resistance input may be more realistic to define the electric load to the stack [6].

In the causal model described in this chapter, either the stack current or voltage can be chosen to be the input of the system. When the stack current is used as the input, the stack voltage shows dynamic behavior with respect to the current density and the pressure conditions. If the stack voltage is used as the input of the system, the dynamic behavior of the stack current represent the performance of the fuel cell system. The input current or voltage is implemented as a boundary

Table 2.1: Fuel cell stack system parameters

Symbol	Variable	Value
n	number of cell in fuel cell stack	381
A_{fc}	fuel cell active area	280 cm^2
J_{cp}	compressor and motor inertia	5×10^{-5} kg·m^2
V_{ca}	cathode volume	0.01 m^3
V_{sm}	supply manifold volume	0.02 m^3
C_D	cathode outlet throttle discharge coefficient	0.0124
A_T	cathode outlet throttle area	0.00175 m^2
$k_{sm,out}$	supply manifold outlet orifice constant	0.3629×10^{-5} kg/(s·Pa)

condition, which is shown in dynamic model for battery cell [28]. When the input is the current from the fuel cell stack, the stack current calculation is straitforward from Equation (2.1) given the pressure conditions. If the stack voltage is chosen as an input, the stack current is calculated by solving Equation (2.1) implicitly as is in [66].

The decision of input and output for the fuel cell system model here is dependent to the specific electric architecture of the fuel cell hybrid. In the case of electric architecture shown in Figure 1.2(a), the current from the fuel cell stack is determined by the DC/DC converter, thus the current is used as an input to the fuel cell model. On the other hand, fuel cell is controlled by it own voltage instead of current in the electric architecture shown in Figure 1.2(b) [32, 58]. The details of integration and control in electric architecture are presented in Chapter 5 and 6.

2.2 Simulation validation

Model validation is performed through simulation comparisons between the 4 state model developed in Section 2.1.1 and 2.1.2, and the originally developed 9 states[1] model [52, 54]. The parameters used in the four state model are summarized in Table 2.1. The dynamic response of the performance variables, which are the stack voltage v_{st}, the stack and net power, P_{st} and P_{net} and oxygen excess ratio λ_{O_2}, are compared.

To demonstrate the FC model characteristics, a series of step changes in stack load (current) and compressor motor input voltage are applied to the stack in Figure 2.3. During the first four steps, the compressor voltage is controlled so that the oxygen excess ratio at 2 is maintained using a simple static feedforward controller. The remaining steps are then applied independently, resulting in different levels of oxygen excess ratios. Also the same current and actuator inputs are applied to the nine state model.

During a positive load step, the oxygen excess ratio drops due to the depletion of oxygen, that correlates well with the drop in the stack voltage. The step at $t = 18$ seconds shows the response due to an increase in the compressor input while keeping the stack current constant. The opposite scenario is shown at $t = 22$ seconds. The response between the 18th and 22th seconds shows that

[1]The nine states are $x = \begin{bmatrix} m_{O_2} & m_{H_2} & m_{N_2} & \omega_{cp} & p_{sm} & m_{sm} & m_{w,an} & w_{w,ca} & p_{rm} \end{bmatrix}^T$ in [52]. Note here that the mass and the pressure of O_2 or N_2 are equivalent terms based on the assumption of the ideal gas law.

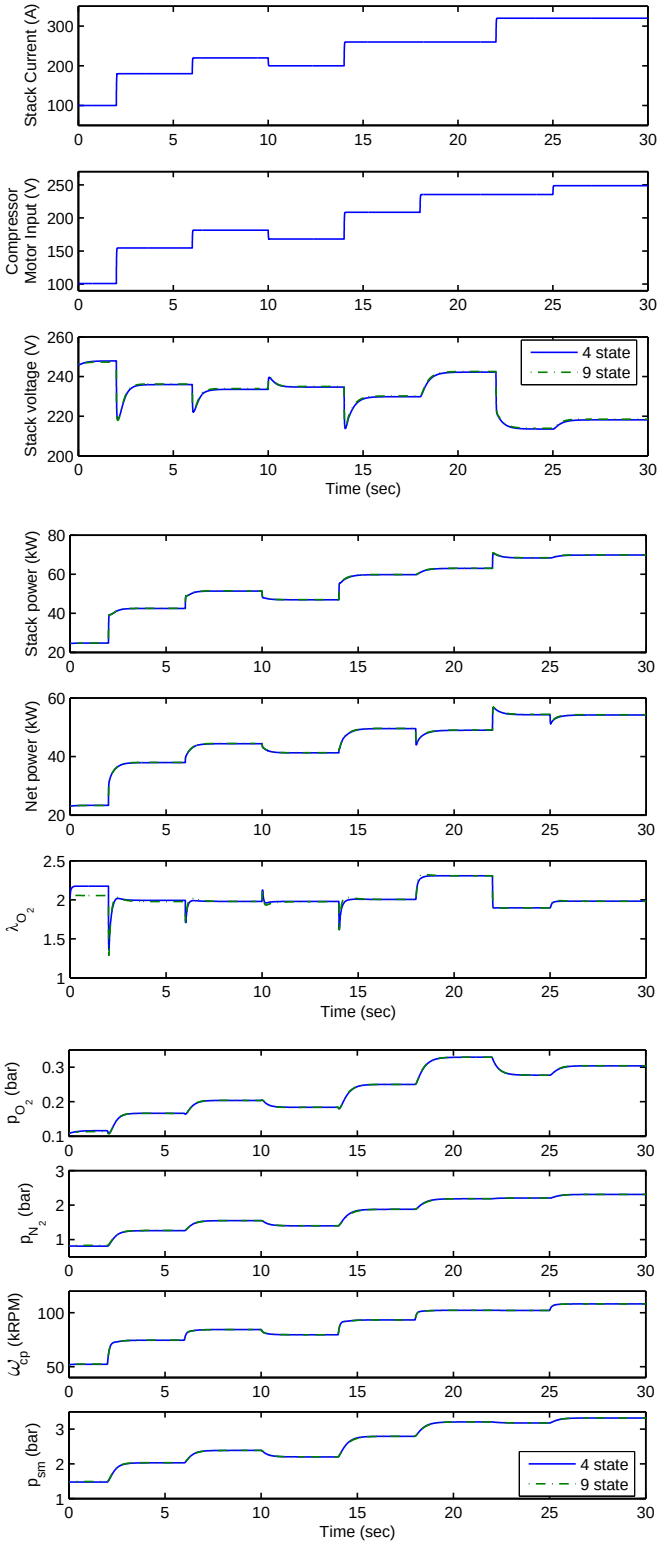

Figure 2.3: Simulation validation of fuel cell reactants supply models

even though the stack voltage v_{st} and power P_{st} increase, the net power $P_{net} = P_{st} - P_{cm}$ actually decreases due to the increased parasitic loss (P_{cm}).

The comparison shows that the equations (2.2) - (2.22) capture the dynamics of voltage and starvation characteristics when humidity and temperature are well controlled. The assumptions in this work eliminate the states of the model in [52], which are return manifold (p_{rm}), hydrogen and vapor pressures (or mass) (m_{H_2}, $m_{w,an}$ and $m_{w,ca}$), and supply manifold mass m_{sm}, but all performance variables and remaining states in (2.24) match well with the original nine state model.

Several other control-oriented fuel cell model derivatives of [52] can be found in literature. The simplest is a two-state model [9, 43], where one dynamic state is cathode pressure used for stack voltage calculation and the other is for compressor dynamics. This two-state model is adequate to model stack power and parasitic losses, and thus is used for vehicle power management system. Drawback of the two state model is, however, that the dynamics inside the fuel cell system, for example, the oxygen excess ratio, can not be captured. The lack of compressor model in another simplified model [63] renders it incapable of describing auxiliary power losses. Finally, another four-state model in [60] has no distinction between oxygen and nitrogen species; thus dynamics of the oxygen excess ratio can not be captured.

We will next analyze the performance limitation and design the controller based on the model developed in this chapter. Also experimental confirmation will be performed in Chapter 4.

Chapter 3

Air flow control of power-autonomous FC system

The purpose of this chapter is to examine the dynamic limitation associated with the air supply to a high-pressure FC power system which will be augmented with DC/DC converter. To investigate the coupling between the electric requirements and the FC power constraints, it is desirable to establish an analytic model for the fuel cell with DC/DC converter and design the overall system. Then the dynamic behavior for fuel cell power system and associated control issues will be covered in Chapter 5 and 6.

The transient response associated with controlling air supply and avoiding oxygen starvation is a key performance factor in PEM fuel cells fed by compressed high-purity hydrogen. The oxygen is supplied through the air supply system and it is typically forced by a blower or a compressor. Although the compressor absorbs a significant amount of power and increases the fuel cell parasitic losses, it is preferred to a blower due to the higher achievable power density (kW/m^3). A blower is typically not capable of pushing high flow rates through the small channels associated with high power density FC stacks. Analysis of the tradeoff between FC power density and parasitic losses from the air supply device can be found in [11]. Comparison of the dynamic flow capabilities of an FC system with a blower and a compressor can be found in [23]. It is shown that the two systems are dynamically similar in providing air flow through the cathode channels. The blower spends time spinning its rotor inertia, which is typically larger than the compressor inertia, whereas the compressor needs time to push the air and elevate the supply manifold pressure. Compressor produces significantly higher operating pressures than a blower.

The goal of this chapter is to examine the performance limitations and tradeoffs associated with the compressor-driven air supply in a high-pressure power-autonomous FC system as shown in Figure 3.1. The importance as well as the limitations of the air supply system in PEM FC is recognized. Regulating air flow based on the flow rate measurement at the supply manifold inlet has a potential limitation because the actual air flow at the cathode inlet is not the same as the

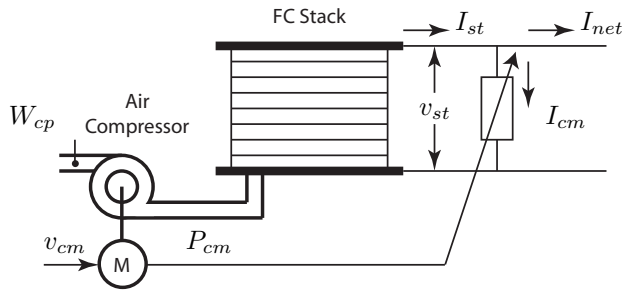

Figure 3.1: Power-autonomous FC stack system

one at the compressor outlet [48, 52, 60]. On the other hand, high compressor control effort to force faster air in the stack can cause instabilities when the compressor draws current directly from the stack [49]. The tradeoff between satisfying net power requirements and maintaining optimum air supply in the stack during load changes is first defined in [54]. We show here that this difficulty is more critical when the compressor motor draws its power directly from the fuel cell as in the case of an autonomous fuel cell. The control limitations achieving fast air flow control in the stack is the result of two non-minimum zeros in the air supply control system. We clarify and quantify these limitations and design controllers that illustrate these limitations in simulations.

The performance limitations are analyzed based on a low-order fuel cell model described in Chapter 2 and Section 3.1. In Section 3.2, the physical problem is formulated into the general control form. The performance measures and control difficulties are summarized in Section 3.3. In Section 3.4, we discuss various feedforward control architectures based on load current measurement and compare them analytically and with simulation. Finally the design of feedback control based on air flow measurement is presented in Section 3.5.

3.1 Power-autonomous fuel cell system

In the high pressure PEM fuel cell system described in Chapter 2, a compressor supplies the air flow necessary for the reaction which depends on the current drawn from the fuel cell, I_{st} as shown in Figure 3.1. The air supplied to the cathode should exceed the air necessary for reaction for several reasons [7, 54]. The oxygen excess ratio (OER), defined as λ_{O_2} in Equation (2.23) of Chapter 2, is a convenient lumped variable to define the control objective in FC air supply. Regulation of λ_{O_2} to a higher enough value can provide enough oxygen into the FC stack to prevent oxygen starvation, but the overall efficiency may decrease due to unnecessary power losses in the air compressor. In this study, we consider the air flow control problem associated with regulating oxygen excess ratio at a fixed desired value ($\lambda_{O_2}^{ref} = 2$), which has been shown to provide adequate supply of oxygen and optimum power generation in the fuel cell stack in [52].

We focus on the dynamic oxygen excess ratio during transient loading. We consider the regulation problem where the compressor is driven directly by the fuel cell, as is shown in Figure 3.1. The total

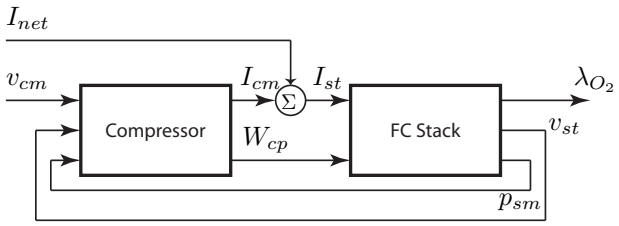

Figure 3.2: Interaction between the air compressor and the FC variable in a power-autonomous FC stack system

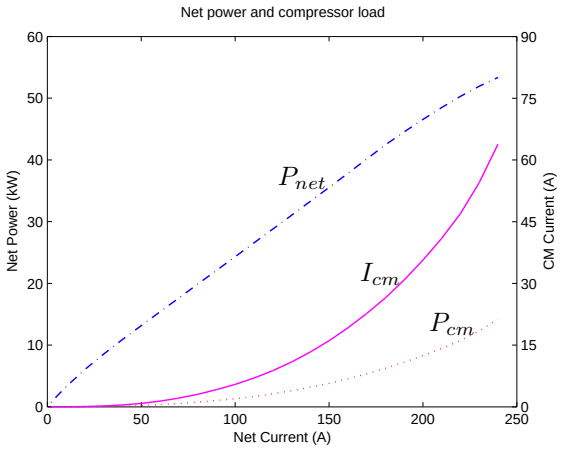

Figure 3.3: Compressor load in the FC system - steady state

current drawn from the fuel cell stack, I_{st} is defined as the sum of the net current I_{net}, which is the current delivered to the load, and the current drawn by all of the FC auxiliaries, particularly the compressor load, I_{cm}

$$I_{st} = I_{net} + I_{cm} \tag{3.1}$$

as shown schematically in Figure 3.1 and in a signal flow diagram in Figure 3.2.

Here it is considered that the compressor motor contributes to the largest percent of FC parasitic losses through the current drawn I_{cm} directly from the stack bus[1]. Figure 3.3 depicts the compressor motor power P_{cm} and net FC power P_{net} when the net current load I_{net} is drawn in steady-state. To calculate the current consumed by the compressor, we assume that the compressor motor has an ideal power transformer. The transformer supplies the necessary power P_{cm} dictated by the DC motor control signal v_{cm} in (2.20) by drawing a current I_{cm} at the FC stack bus voltage v_{st}

$$I_{cm} = P_{cm}/v_{st}. \tag{3.2}$$

Thus, the compressor motor current is implemented so that P_{cm} is simply drawn from the stack through a DC motor control unit instantaneously.

[1] A 75 kW fuel cell stack is typically supplied by 15 kW compressor power [12, 52].

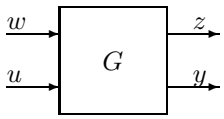

Figure 3.4: General control formulation

The FC air supply interacts with the FC stack through an electrical and an air flow path as shown in Figure 3.2. The electrical coupling is established by the stack voltage v_{st} through Equation (3.2). The FC stack voltage v_{st} is given by the polarization curve in [52, 54]. The air flow through the compressor depends on the FC stack supply manifold pressure p_{sm} through Equation (2.5) in Chapter 2. As can be seen in Figure 3.2, the effect of the compressor voltage command v_{cm} to the oxygen excess ratio λ_{O_2} is also influenced by the interaction between the compressor and FC stack through the air flow path and the electric path.

3.2 Control problem formulation for FC air supply

The control objective of regulating the oxygen excess ratio λ_{O_2} in the fuel cell stack can be achieved by a feedforward and/or feedback control using a compressor motor voltage command v_{cm} during the load (current) changes. Since the performance variable λ_{O_2} is not directly measured, we regulate λ_{O_2} based on two measurements, namely, the demanded load I_{net}, and the air flow rate at the compressor, W_{cp}.

Linear control techniques are used throughout this paper to analyze the inherent control difficulties and to design a controller for the system. A nominal operating point of 40 kW FC net power (67% of the maximum FC net power) is used for the linearization of the nonlinear FC stack system. Deviations from the nominal net current $I^o_{net} = 169$ A, compressor motor voltage command $v^o_{cm} = 164$ V and associated nominal oxygen excess ratio $\lambda^o_{O_2} = 2$ are considered to define the control problem in the general control configuration $[\ z \quad y\ ]^T = G\ [\ w \quad u\ ]^T$ with

$$G = \begin{bmatrix} G_{zw} & G_{zu} \\ G_{yw} & G_{yu} \end{bmatrix} \tag{3.3}$$

as shown in Figure 3.4. Specifically, the control of the FC air supply can be described as a disturbance rejection problem with performance variable $z = \delta\lambda_{O_2} = \lambda_{O_2} - \lambda^o_{O_2}$, control input $u = \delta v_{cm} = v_{cm} - v^o_{cm}$ and disturbance input $w = \delta I_{net} = I_{net} - I^o_{net}$.

The plant transfer functions G_{zu} from u to z, and G_{zw} from w to z of the power-autonomous FC are

$$G_{zu} = \frac{-0.00741(s+101)(s-19.2)(s+3.15)(s+3.09)}{(s+71.3)(s+19.6)(s+3.28)(s+3.12)} \tag{3.4}$$

$$G_{zw} = \frac{-0.0103(s+67.7)(s+19.4)(s+3.29)(s+3.09)}{(s+71.3)(s+19.6)(s+3.28)(s+3.12)}. \tag{3.5}$$

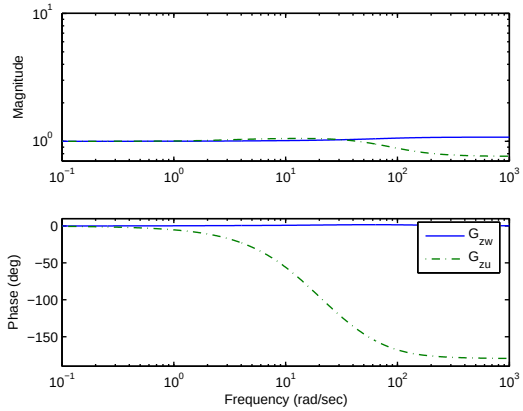

Figure 3.5: Plant transfer function from I_{net} to λ_{O_2} (G_{zw}) and from v_{cm} to λ_{O_2} (G_{zu})

As can be seen in (3.4) and (3.5) G_{zu} and G_{zw} are both stable and have zero relative degree. The transfer function G_{zw} indicates a minimum phase system while G_{zu} has a non-minimum phase (NMP) zero $\zeta_z = 19.2$.

Figure 3.5 shows the frequency responses of the normalized plant transfer functions G_{zw} and G_{zu}. As can be seen in the frequency response plot, G_{zu} has a phase lag associated with non-minimum phase behavior, whereas G_{zw} resembles a static gain. The flat frequency response of the G_{zw} can be physically explained by the direct effect of the net current I_{net} on the stack current I_{st}, which statically affects the mass flow rate of the oxygen reacted in the cathode $W_{O_2,rct}$, which, in turn, affects the OER defined by Equation (2.23). Note that while I_{net} affects statically the $W_{O_2,rct}$ which is the denominator of OER in (2.23), it barely affects the cathode pressure p_{ca} (by depleting oxygen) and thus causes insignificant variation in oxygen flow in the cathode $W_{O_2,in}$, which is the numerator of OER in (2.23).

The non-minimum phase zero in G_{zu} is unavoidable in power-autonomous fuel cell system. The actuator u affects performance variable λ_{O_2} through the flow path and the electric path (see Figure 3.2), with mutual conflicting results. An increase in the compressor command increases the air flow to the FC, and consequently increases the oxygen excess ratio λ_{O_2}, but an increase in the compressor command also increases the FC parasitic load I_{cm}, thus decreases the oxygen excess ratio. The interaction of these two and opposite contributions introduces the non-minimum phase behavior. Moreover, it is important that the NMP behavior is always present independently of the type of compressor or blower in air supply, as long as the power for the air supply component is from the stack itself without an energy buffer such as battery.

Regulating the oxygen excess ratio can be implemented by a feedforward controller since the disturbance input I_{net} can be measured directly. The design limitations associated with NMP dynamics in G_{zu} and the design of feedforward control are discussed in Section 3.3 and 3.4.

Besides the feedforward control, additional measurement from the plant can be used to improve the performance and/or the robustness. Specifically, a feedback controller based on the compressor

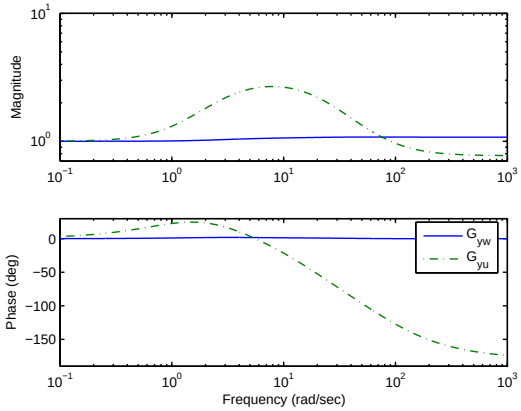

Figure 3.6: Plant transfer function from I_{net} and v_{cm} to air flow error $W_{cp}^{ref} - W_{cp}$ which are denoted as G_{yw} and G_{yu}, respectively

flow measurement W_{cp} will be considered in Section 3.5 similarly to [49] and [53]. The feedback control can be applied so that W_{cp} tracks the reference air flow command W_{cp}^{ref}, thus defining the measurement y

$$y = W_{cp}^{ref} - W_{cp} \tag{3.6}$$

for the general control configuration in Figure 3.4. The demanded air flow rate W_{cp}^{ref} is based on the stack load measurement, I_{st}, and the desired oxygen excess ratio $\lambda_{O_2}^{ref}$, as defined in [53]

$$W_{cp}^{ref} = W_{cp}^{ref}(I_{st}, \lambda_{O_2}^{ref}) \tag{3.7}$$

so that the oxygen excess ratio can be regulated to the desired value $\lambda_{O_2}^{ref}$ at steady-state when the compressor air flow W_{cp} satisfies the reference value W_{cp}^{ref}. The plant transfer functions G_{yu} and G_{yw} are

$$G_{yu} = \frac{0.198(s-81.9)(s+68.3)(s+3.13)(s+1.07)}{(s+71.3)(s+19.6)(s+3.28)(s+3.12)} \tag{3.8}$$

$$G_{yw} = \frac{0.274(s+71.9)(s+19.2)(s+3.34)(s+2.9)}{(s+71.3)(s+19.6)(s+3.28)(s+3.12)} \tag{3.9}$$

for the same operating point defined previously.

Figure 3.6 shows the frequency responses of the normalized plant transfer functions G_{yw} and G_{yu}. As can be seen in the figure, G_{yw} resembles a static gain similarly to G_{zw} in Figure 3.5. This flat frequency response is consistent with the system physics because the net load current I_{net} disturbance directly affects $W_{cp}^{ref}(I_{st})$ through Equation (27) of [53], but it causes minor changes in the compressor air flow W_{cp}, in the open-loop plant.

The existence of a non-minimum phase zero in G_{yu} is unavoidable in a power-autonomous fuel cell system. The control command u affects the measurement $y = W_{cp}^{ref}(I_{st}) - W_{cp}$ through the

flow path and the electric path. Specifically, an increase in the compressor command increases the air flow at the compressor W_{cp}, whereas an increase in the compressor command increase the FC parasitic load I_{cm} and consequently the demanded air flow $W_{cp}^{ref}(I_{st})$. The NMP zero $\zeta_y = 81.9$ in the response from u to y imposes feedback bandwidth limitation on the ability to track the air flow requirement $W_{cp}^{ref}(I_{st})$. Therefore, high gain control on the compressor command can cause instabilities when the compressor draws current directly from the stack, which is empirically observed in [49].

The differences in performance z and measurement y as shown by the frequency responses in Figure 3.5 and 3.6 introduce more difficulties in the control design. The differences in G_{yu} and G_{zu} characterize the different dynamic behavior of z and y, and thus the design of the feedback controller using the measurement y needs to take into account the performance variable, i.e., the oxygen excess ratio λ_{O_2}. Prior work in [48, 52, 60] reports in a qualitative manner that regulating the cathode oxygen flow based on the compressor air flow rate measurement has a potential limitation because the actual air flow at the cathode of the FC stack is not the same as the one at the compressor, thus causing significant problems in regulating oxygen excess ratio inside the stack. The detailed design limitations on feedback control and control design that takes these limitations into account are covered in Section 3.5.

3.3 Performance measures and constraints

While the controller architecture for FC air supply already has been described in [49, 52] as a combined feedforward and feedback control based on the load current and air flow rate measurement, this paper examines the fundamental limitations for the first time. Generalized bounds on control performances are established to clarify and quantify the control difficulties. For performance evaluation, we consider the disturbance response ratio [19]

$$R_{zw} = \frac{T_{zw}}{G_{zw}} \tag{3.10}$$

which is the ratio of the closed-loop response T_{zw} to the open-loop response G_{zw}. The disturbance response ratio is a measure of the performance of the controller in rejecting the disturbance $w = \delta I_{net}$. Given a feedforward controller K_{uw} and feedback controller K_{uy} as in Figure 3.7, the closed-loop response T_{zw} is

$$T_{zw} = G_{zw} + G_{zu}K_{uw} + G_{zu}K_{uy}(1 - G_{yu}K_{uy})^{-1}(G_{yw} + G_{yu}K_{uw}). \tag{3.11}$$

We consider the integral constraints upon R_{zw} for the control system of the plant (3.4)-(3.5) because there exists a non-minimum phase zero in G_{zu}. Since the system is open-loop stable, G_{zw} is minimum phase, and G_{zu} has a NMP zero ζ_z, if T_{zw} is minimum phase[2] then the Poisson integral

[2]The existence of non-minimum phase zero in T_{zw} cannot be determined without the controller, so that the

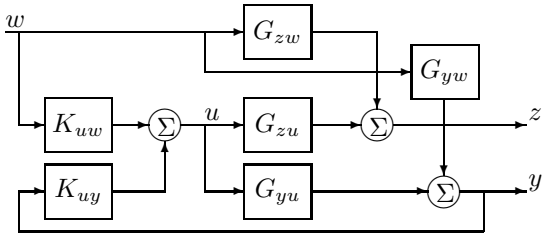

Figure 3.7: Control configuration with feedforward/feedback control

for NMP zeros of G_{zu} (from Proposition V.7 in [19]) is

$$\int_0^\infty \log|T_{zw}(j\omega)|W(\zeta_z,\omega)d\omega = 0 \tag{3.12}$$

and

$$\int_0^\infty \log|R_{zw}(j\omega)|W(\zeta_z,\omega)d\omega = 0 \tag{3.13}$$

where

$$W(\zeta_z,\omega) = \frac{2\zeta_z}{\zeta_z^2+\omega^2}. \tag{3.14}$$

Integral constraints upon R_{zw} due to the NMP zero in G_{zu} in (3.13) dictate that if $|R_{zw}| < 1$ over any frequency range, then necessarily $|R_{zw}| > 1$ at other frequencies since $W(\zeta_z,\omega) > 0, \forall\omega$. Design tradeoffs imposed by Poisson integral in (3.13) are valid with arbitrary measurements, thus they can be applied with any feedforward and feedback controller.

Also we examine the step response of the disturbance response ratio R_{zw} with the normalized integral square output error

$$\|\frac{1}{s}R_{zw}\|_2^2, \tag{3.15}$$

and compare the closed-loop performance associated with various controllers using the cost function

$$J_{\lambda_{O_2}} = \int_0^\infty z^2 dt. \tag{3.16}$$

3.4 Feedforward control design

Since the disturbance input I_{net} is measured, we can apply feedforward control. In the case of a feedforward controller K_{uw} using the disturbance measurement directly as shown in Figure 3.8, the response of z to w is

$$T_{zw} = G_{zw} + G_{zu}K_{uw}. \tag{3.17}$$

Using the performance measures and the insight from the integral constraints in the previous section, various feedforward controllers are compared and analyzed.

condition of T_{zw} will be confirmed after the control design.

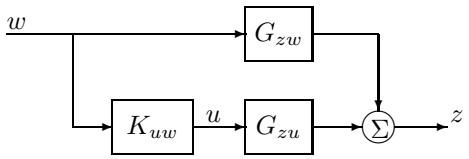

Figure 3.8: Feedforward control configuration when the disturbance is measured directly

3.4.1 Feedforward cancellation controller

A cancellation control that perfectly regulates the performance variable z in the presence of disturbance w may be achieved with a dynamic feedforward controller. The ideal dynamic feedforward controller $K_{uw} = K_{uw}^{ideal}$, that yields $T_{zw} = 0$, can be derived based on a plant inversion

$$K_{uw}^{ideal} = -G_{zu}^{-1} G_{zw}. \tag{3.18}$$

The resulting cancellation controller K_{uw}^{ideal} is, however, unstable due to the non-minimum phase zero ζ_z of G_{zu}. Implementation of the controller in (3.18) is not desirable due to the exact cancellation of NMP zero. As perfect disturbance cancellation using feedforward controller K_{uw}^{ideal} is not a robust option, it is necessary to evaluate the disturbance rejection performance of various other feedforward controllers.

3.4.2 Dynamic and static feedforward control

Since the ideal feedforward controller in (3.18) is unstable due to the non-minimum phase zero ζ_z in G_{zu}, a minimum-phase approximation $\tilde{G}_{zu}$ such that

$$G_{zu} = \tilde{G}_{zu} \frac{\zeta_z - s}{\zeta_z + s}, \tag{3.19}$$

can be applied to replace G_{zu} in (3.18). The transfer function $\tilde{G}_{zu}$ is minimum phase, but maintains the magnitude of G_{zu}. The resulting quasi-cancellation controller K_{uw}^{real} is

$$K_{uw}^{real} = -\tilde{G}_{zu}^{-1} G_{zw}. \tag{3.20}$$

The frequency response of dynamic feedforward controller K_{uw}^{real} and K_{uw}^{ideal} can be seen in Figure 3.9. The magnitudes of two controller transfer functions are identical, though the phase of K_{uw}^{real} differs by 180 degrees at high frequency from the phase of K_{uw}^{ideal}.

It is shown in [26] that assuming G_{zw} is approximated by a static function the feedforward controller, K_{uw}^{real} realizes the minimum achievable normalized integral square output error (using Theorem 2 in [56]) due to a unit step disturbance

$$\min \| \frac{1}{s} R_{zw} \|_2^2 = \frac{2}{\zeta_z} = 0.1044. \tag{3.21}$$

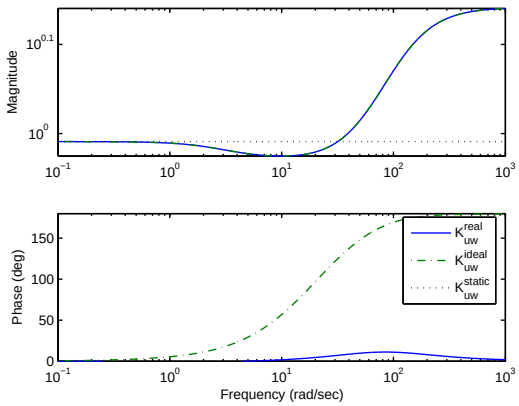

Figure 3.9: Frequency responses of the feedforward controllers, K_{uw}^{real}, K_{uw}^{ideal} and K_{uw}^{static}

In our case, the load disturbance directly affects the oxygen excess ratio, thus G_{zw} can be approximated as a static gain indicated by the near pole-zero cancellation in (3.5) (see Figure 3.5). Therefore it is expected that the K_{uw}^{real} can achieve very good disturbance rejection as indicated by the small values for the measures $\|\frac{1}{s}R_{zw}\|_2^2$ and $J_{\lambda_{O_2}}$ in Table 3.1.

We also compare the performance of dynamic feedforward control with a static feedforward controller. The static feedforward controller

$$K_{uw}^{static} = -\frac{G_{zw}(0)}{G_{zu}(0)} \tag{3.22}$$

has the desired property that the disturbance is completely rejected at DC. The feedforward controller K_{uw}^{static} is realizable only if the DC gain of G_{zu} is not zero, as in the case for this system. Also static feedforward control can be easily implemented by a look-up table.

The disturbance response ratio R_{zw} for K_{uw}^{real} and K_{uw}^{static} feedforward control is shown in Figure 3.10(a). The closed-loop frequency response of each controller explicitly shows tradeoffs due to the Poisson integral in (3.13). At low frequency ranges, both controllers perform well with $|R_{zw}| < 1$, while $|R_{zw}| > 1$ at high frequency ranges. The similarity in the disturbance response at low frequency between the dynamic and static feedforward controller can be explained by the frequency response of K_{uw}^{real} and K_{uw}^{static} as shown in Figure 3.9. The magnitude and phase of the dynamic controller K_{uw}^{real} are similar to the ones of K_{uw}^{static} below the frequency of 10 rad/sec. The disturbance response with dynamic feedforward K_{uw}^{real} is slightly larger than the one obtained by the static feedforward at high frequency due to the small improvements achieved between 6–40 rad/sec.

The disturbance response of both the dynamic and static feedforward controllers to a 20 A step change in load current, corresponding to a power step from 40 to 45 kW, is shown in Figure 3.10(b). Both feedforward controllers show similar oxygen excess ratio λ_{O_2} recovery after the initial excursion. The two controller also achieve similar values for the measures $J_{\lambda_{O_2}}$ and $\|\frac{1}{s}R_{zw}\|_2^2$ as shown in Table 3.1. The initial disturbance responses following a load step change at 0.2 seconds shows a

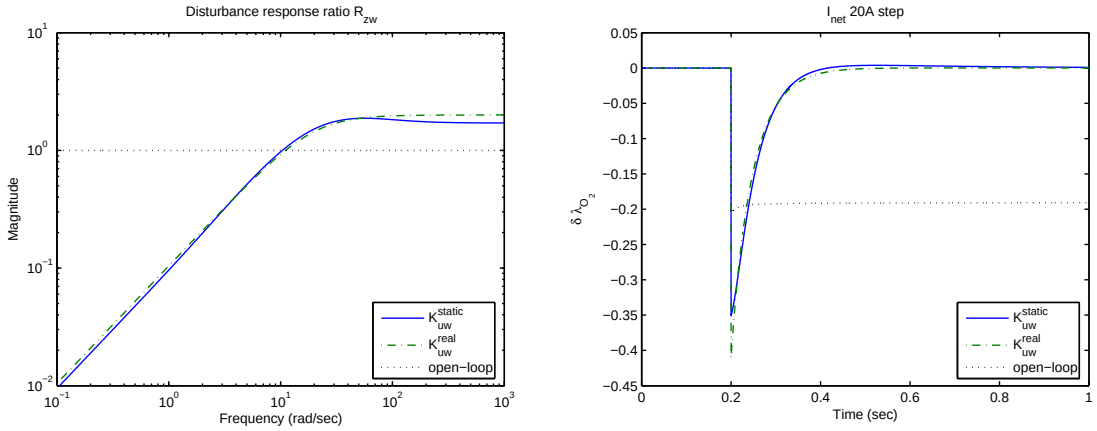

(a) Disturbance response ratio

(b) Step response

Figure 3.10: Disturbance rejection performance with K_{uw}^{real} and K_{uw}^{static} feedforward controller

larger excursion in oxygen excess ratio with K_{uw}^{real} than the one observed with K_{uw}^{static} matching the high frequency behavior in Figure 3.10(a).

The initial excursion of λ_{O_2} corresponds to the largest λ_{O_2} deviation from the nominal value, and thus is the most critical value for oxygen starvation and stack life. This excursion is important enough to warrant further analytic investigation of its value and occurrence. The initial excursion of $z = \delta\lambda_{O_2}$ during a load step change with K_{uw}^{real} controller can be determined analytically from T_{zw}

$$\begin{aligned} T_{zw} &= G_{zw} + G_{zu}K_{uw}^{real} \\ &= G_{zw} - G_{zu}\frac{G_{zw}}{G_{zu}}\frac{\zeta_z - s}{\zeta_z + s} \\ &= G_{zw}\left(1 - \frac{\zeta_z - s}{\zeta_z + s}\right). \end{aligned} \tag{3.23}$$

Then the H^∞ norm of R_{zw} with dynamic feedforward control is

$$\|R_{zw}\|_\infty = \sup_\omega \left|1 - \frac{\zeta_z - j\omega}{\zeta_z + j\omega}\right| = 2 \tag{3.24}$$

attained at infinite frequency. This value implies that the disturbance response of dynamic feedforward control is twice as large at high frequencies ($\omega > 100$ rad/sec in our problem) as the initial excursion of the uncontrolled plant for a given step disturbance. The $\|R_{zw}\|_\infty$ is independent of the location of the non-minimum phase zero ζ_z and always equals 2 with dynamic feedforward control if there exists a NMP zero in the plant G_{zu}. Since all air flow devices powered directly by the FC cause a NMP behavior in the G_{zu} response, all autonomously powered FC system will, thus, have a significant drop in oxygen excess ratio response if a similar dynamic feedforward controller is applied.

In the case of the static feedforward controller that exactly cancels the current disturbance at DC (zero frequency), the initial excursion depends solely on the mismatch between the dynamics from the disturbance to the performance G_{zw} and the dynamics from the control input to the performance G_{zu}. The initial excursion of λ_{O_2} during a load step change with K_{uw}^{static} controller can be calculated from T_{zw}

$$\begin{aligned} T_{zw} &= G_{zw} + G_{zu}K_{uw}^{static} \\ &= G_{zw} - G_{zu}\frac{G_{zw}(0)}{G_{zu}(0)}. \end{aligned} \tag{3.25}$$

This time, the H^∞ norm of R_{zw}

$$\|R_{zw}\|_\infty = \sup_\omega \left| 1 - \frac{G_{zu}/G_{zu}(0)}{G_{zw}/G_{zw}(0)} \right| = 1.87 \tag{3.26}$$

attained at $\omega = 60$ rad/sec, while the infinite frequency response of the $|R_{zw}|$ is

$$\lim_{s\to\infty} |R_{zw}| = 1.71. \tag{3.27}$$

This corresponds to the initial excursion of the oxygen excess ratio with static feedforward control K_{uw}^{static}, which is 1.71 times larger than the one observed in the uncontrolled plant as shown in Figure 3.10(b). Due to the smaller initial λ_{O_2} excursion and ease of implementation, the stack feedforward control K_{uw}^{static} is more preferable than the dynamic feedforward control K_{uw}^{real}.

Note here that a static feedforward controller which regulates λ_{O_2} at steady-state can be implemented by measuring the FC stack current I_{st}, instead of the net (load) current I_{net}. The I_{st}-based feedforward control has been proposed in [53] for the case where the compressor was not powered by the FC stack. When the compressor current is drawn from the fuel cell stack, a portion of the stack load is proportional to the control effort. Therefore the total stack load current is no longer pure disturbance.

The disturbance response ratio of I_{st}-based controller is compared with static feedforward controller in Figure 3.11(a). The response with I_{st}-based control shows larger disturbance amplification than the one with K_{uw}^{static} at high frequency ranges (over 10 rad/sec). In mid frequency, the disturbance rejection performance is better with I_{st}-based control. This tradeoff between the better mid frequency response versus the worse high frequency responses follows the integral constraints in (3.13). There is a small DC error with the I_{st}-based controller because linearization is not accurate away from the nominal operating point. The step response in Figure 3.11(b) reflects the frequency responses of I_{st}-based control. The initial excursion to step load using the I_{st}-based controller is larger than the one of the static I_{net}-based feedforward controller and recovery time is reduced.

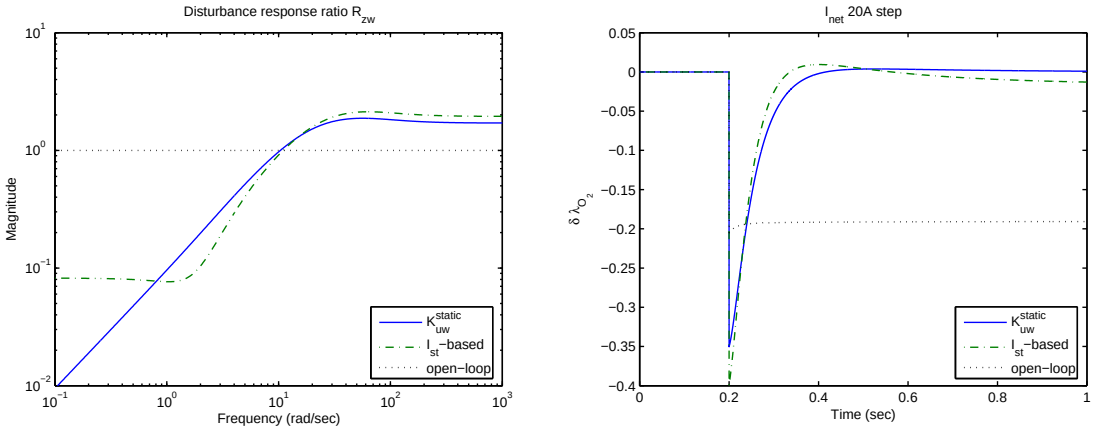

(a) Disturbance response ratio

(b) Step response

Figure 3.11: Disturbance rejection performance of I_{st}-based control

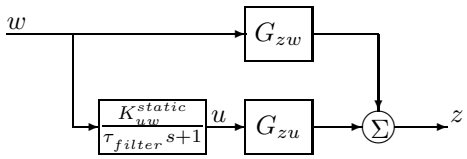

Figure 3.12: Disturbance rejection with a filtered feedforward controller

3.4.3 Static feedforward control with filtered command

The NMP zero dynamics of G_{zu} and the associated integral constraints impose a stringent tradeoff between our ability to achieve simultaneously a small initial excursion and a fast recovery in λ_{O_2} during step change in the load current. A compromise in favor of reducing the initial excursion can be achieved by filtering the static feedforward controller as shown by the schematic of Figure 3.12.

Integral relations applied to Equation (3.13) are still valid even after adding a filter to the control command. The disturbance response ratio in Figure 3.13(a) shows the disturbance attenuation over all frequency ranges. The disturbance attennuation at high frequency improves as the time constant of the filter, τ_{filter}, increases. Meanwhile, the disturbance rejection performance at low frequency deteriorates following the Poisson integral constraint in (3.13). The step responses in Figure 3.13(b) show the tradeoff in time domain as well. An increased τ_{filter} reduces the amount of initial excursion, but decreases the recovery time after the initial excursion occurs. Figure 3.14 summarizes the tradeoff between the initial excursion and the recovery time in oxygen excess ratio during step disturbances.

The integral square output error $J_{\lambda_{O_2}}$ also increases as τ_{filter} increases (in Table 3.1). Larger τ_{filter} increases the recovery time and $J_{\lambda_{O_2}}$ despite the reduced initial excursions. The deterioration in $J_{\lambda_{O_2}}$ can be seen by comparing the areas in Figure 3.13(b). The performance measure $\|\frac{1}{s}R_{zw}\|_2^2$ is similar to $J_{\lambda_{O_2}}$ as shown in Table 3.1. Although K_{uw}^{real} and K_{uw}^{static} are not necessarily the optimal controllers since G_{uw} is not exactly static, the associated closed-loop performance is better than the

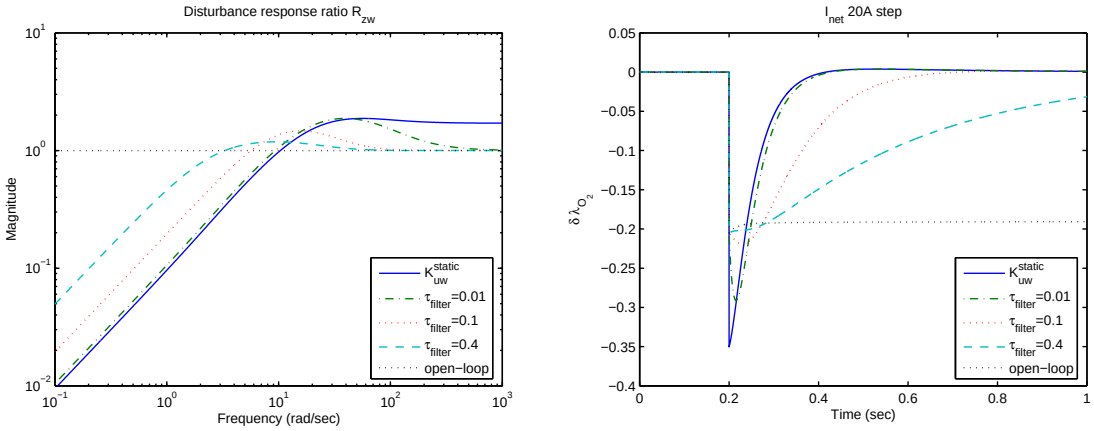

(a) Disturbance response ratio

(b) Step response

Figure 3.13: Disturbance rejection performance of static feedforward with filtered command

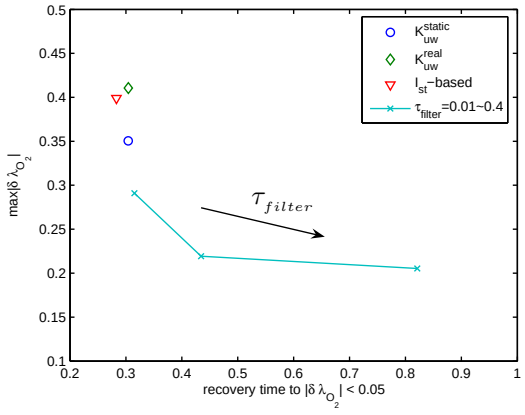

Figure 3.14: Oxygen excess ratio excursion versus recovery time comparison

Controller	$\|\frac{1}{s}R_{zw}\|_2^2$	$J_{\lambda_{O_2}}$
K_{uw}^{real}	0.1044	0.0632
K_{uw}^{static}	0.1051	0.0633
K_{uw}^{static} with $\tau_{filter} = 0.01$	0.1114	0.0650
K_{uw}^{static} with $\tau_{filter} = 0.1$	0.1551	0.0760
K_{uw}^{static} with $\tau_{filter} = 0.4$	0.3008	0.1052

Table 3.1: Performance measures $\|\frac{1}{s}R_{zw}\|_2^2$ and $J_{\lambda_{O_2}}$ during step disturbance

one obtained after the filtering.

3.5 Feedback control design

While the best performance can be achieved with the feedforward control proposed in Section 3.4, feedforward control is sometimes sensitive to uncertainties. Feedback control based on additional measurements could mitigate the sensitivity to modeling error and device aging, so the performance of feedback controllers are studied next.

3.5.1 Cancellation with feedback control

Cancellation control that perfectly attenuates disturbance response in the performance variable z may be achieved with a feedback controller. For the general control configuration with a feedback controller K_{uy} depicted in Figure 3.15, the closed-loop response from w to z, T_{zw}, is given by

$$T_{zw} = G_{zw} + G_{zu}K_{uy}(1 - G_{yu}K_{uy})^{-1}G_{yw} \tag{3.28}$$

where G_{zw}, G_{zu}, G_{yw} and G_{yu} correspond the plant transfer functions in (3.4) and (3.5) of Section 3.2. Since $G_{zu} \neq 0$, $G_{yw} \neq 0$, and $G_{zw}G_{yu} - G_{zu}G_{yw} \neq 0$ in our problem, a feedback controller $K_{uy} = K_{uy}^C$, where

$$K_{uy}^C = \frac{G_{zw}}{G_{zw}G_{yu} - G_{zu}G_{yw}} \tag{3.29}$$

yields $T_{zw} = 0$, and thus may achieve perfect cancellation from the Lemma III.5 in [19]. However, the NMP zero ζ_z of G_{zu} does not satisfy the multiplicity bound

$$m_{zw}(\zeta_z) \geq m_{zu}(\zeta_z) + m_{yw}(\zeta_z) \tag{3.30}$$

that ensures stability from Proposition IV.6 in [19]. Notably, the closed-loop system with the cancellation controller K_{uy}^C in (3.28) is unstable internally.

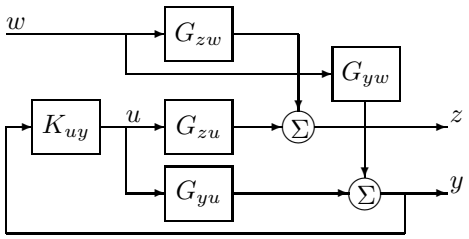

Figure 3.15: Control configuration with feedback control

3.5.2 Proportional integral feedback controller

The oxygen excess ratio λ_{O_2} regulation with feedforward control K_{uw}^{static} or K_{uw}^{real} shows the best integral square output errors from the results in Section 3.4. A simple, proportional and integral (PI) controller

$$K_{uy} = K_P \left(1 + \frac{K_I}{s}\right) \tag{3.31}$$

is added to the static feedforward controller K_{uw}^{static}, based on measuring the difference between W_{cp} and W_{cp}^{ref} in (3.6), so that a zero steady-state flow error and oxygen excess ratio can be achieved despite model uncertainties.

The disturbance response ratios and step responses in Figure 3.16 show the differences between the measurement (compressor flow) and the performance output (oxygen excess ratio) with different feedback control gains K_P and K_I. As can be seen in Figure 3.16(a), the disturbance response increases at both low and high frequency ranges as K_P increases. Larger feedback gain K_P leads to fast settling in compressor air flow (in Figure 3.16(e)), but overcompensates λ_{O_2} and thus results in larger λ_{O_2} excursion and slow recovery in Figure 3.16(c).

Increase in K_I also leads to increased disturbance response, but only at low frequency ranges as can be seen in Figure 3.16(b). With small K_I the feedback control looses its control authority and the feedforward controller determines the performance. The feedback control gains are chosen as $K_P = 0.01$ and $K_I = 10$. The closed loop system performance with these feedback gains is very similar with the response obtained with the static feedforward controller in Section 3.4.

The feedback control designed in this section reduces the sensitivity function $S = 1/(1+L)$ as can be seen in Figure 3.17. In a case of feedforward control, the sensitivity of the system with respect to uncertainties is equal to unity at all frequencies. Although it is hard to notice in the figure, there exist the frequency ranges where the sensitivity function $|S| > 1$ in the case of combined feedforward/feedback control, which follows the Bode integral relations [20].

The non-minimum phase zero ζ_y in G_{yu} affects the closed-loop stability, so that the bandwidth of a stable closed-loop system with feedback control is limited by the NMP zero, e.g., $\omega_{BW,y} < \zeta_y$ [47]. However, this feedback control limitation only implies control bandwidth bounds on regulating the measured output y, and does not necessarily imply degradation in the performance output z because there are differences between the response of G_{zu} and G_{yu}. As can be seen in Figure 3.16, although high feedback gain improves the tracking of the compressor flow (measurement output y),

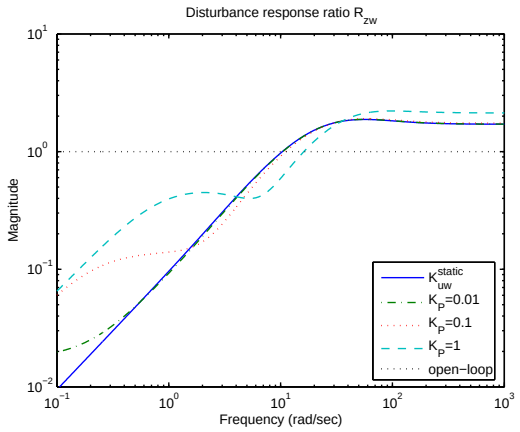

(a) Disturbance response ratio with respect to K_P (K_I = 10)

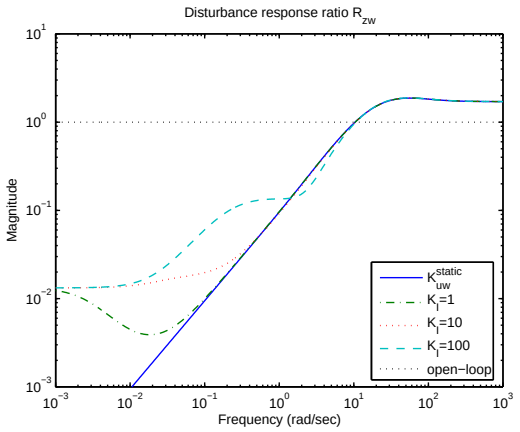

(b) Disturbance response ratio with respect to K_I (K_P = 0.01)

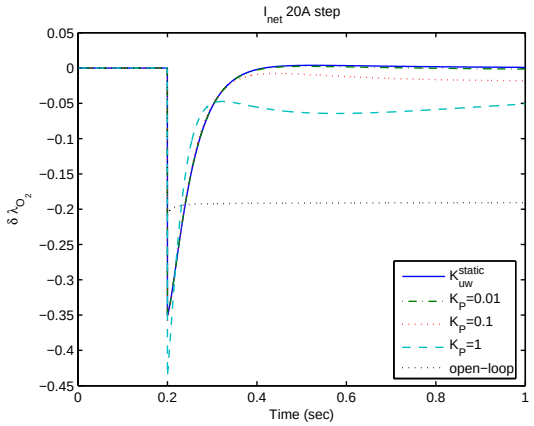

(c) Step response with respect to K_P ($K_I = 10$)

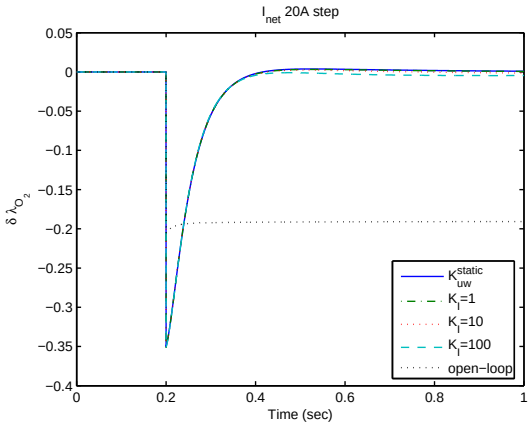

(d) Step response with respect to K_I ($K_P = 0.01$)

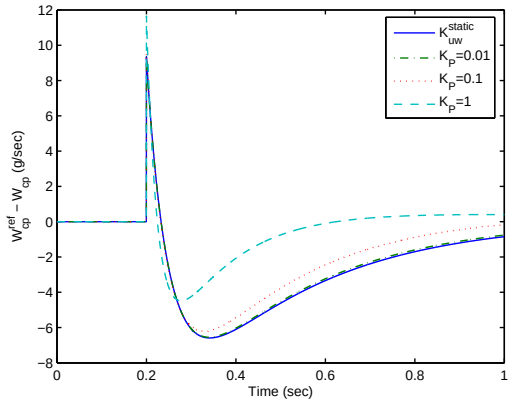

(e) Error in W_{cp} with respect to K_P ($K_I = 10$)

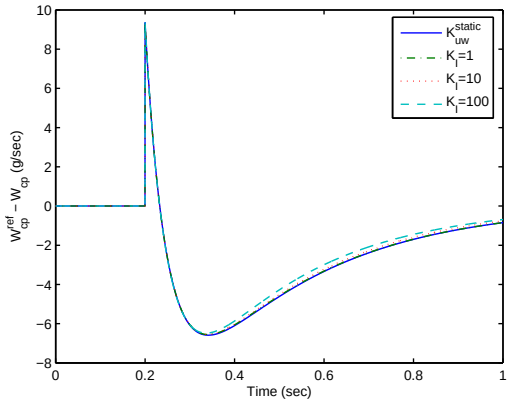

(f) Error in W_{cp} with respect to K_I ($K_P = 0.01$)

Figure 3.16: Disturbance rejection performance of feedback control with K_P and K_I variation

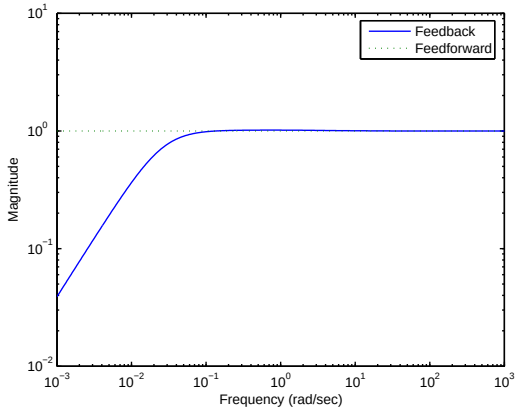

Figure 3.17: Magnitude of sensitivity function of the system with feedback and feedforward control

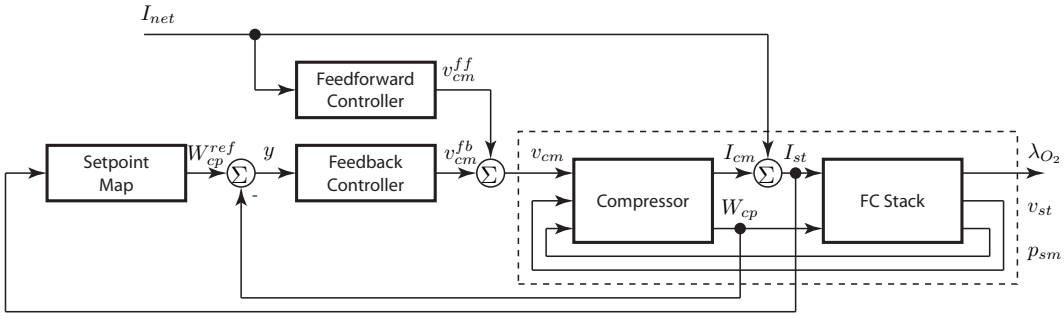

Figure 3.18: Schematic of the fuel cell stack system with air flow control using compressor

it deteriorates the regulation of oxygen excess ratio (performance output).

In conclusion, a low gain feedback controller combined with static feedforward map could provide a control design with adequate performance, robustness and complexity. The compressor control command can be written as

$$\begin{aligned} v_{cm}(t) &= v_{cm}^{ff}(t) + v_{cm}^{fb}(t) \\ &= f(I_{net}) \\ &\quad + K_P \left[\left(W_{cp}^{ref}(I_{st}(t)) - W_{cp}(t) \right) + K_I \int_0^t \left(W_{cp}^{ref}(I_{st}(\tau)) - W_{cp}(\tau) \right) d\tau \right] \end{aligned} \tag{3.32}$$

and the air flow control architecture is shown in Figure 3.18. The feedforward control is implemented as a look-up table, whereas the linear feedback control is based on the nominal operating point.

Chapter 4

Experimental confirmation

In this chapter, the model developed in Chapter 2 and the limitations identified in Chapter 3 are qualitatively confirmed with experiments. The experimental setup consists of a small and commercial fuel cell system (Nexa™ by Ballard Power System Inc.), an electric load and measurement devices installed at the Fuel Cell Control Laboratory in the University of Michigan. Nexa™ fuel cell stack system is an example of power-autonomous fuel cell system supplying power to all its auxiliary components from its own stack power except during start-up and shutdown. Nexa™ has its own dedicated proprietary controller and safety systems so the experimental data collected correspond to the closed-loop behavior of the system. An external controllable load is used to test the Nexa™ behavior.

Using this experimental setup, the closed-loop system response with the model and control design developed in Chapter 2 and 3 is compared with the response of the Nexa™ system and a qualitative confirmation of the model and controller is achieved. Although the qualitative confirmation is a weaker result than a full validation, the comparison presented here provides some level of confidence in the simulation model. Moreover, the comparison shows that all the previous modeling and control analysis results can be applied to a much smaller fuel cell stack system (1.2 kW) than the one originally used (75 kW).

4.1 System operation

The Nexa™ is fully automated, air cooled fuel cell system with internal air humidification, and is designed to be integrated into portable and back-up power. The rated net power is 1200 W at full load with the stack voltage at 26 V. The stack has a total of 47 cells connected in series. Hydrogen is supplied from the compressed tank through the safety system and ambient air is used as oxidant to the cathode through a built-in blower. The supply pressures to the stack are 5.0 psig for the anode and 2.2 psig for cathode. The operating temperature is 65 ℃ which is controlled by another blower in an air-cooled configuration. The operating pressure at fuel supply inlet is chosen at 20 psig.

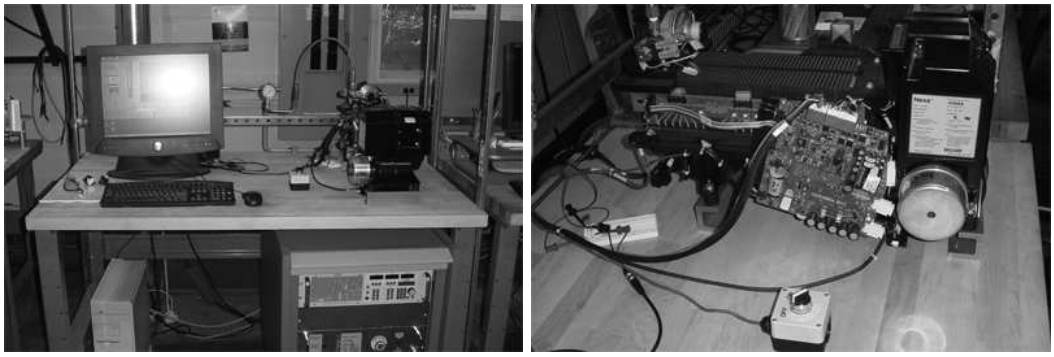

Figure 4.1: Experimental setup

Figure 4.1 depicts the Nexa™ fuel cell system, measurement and safety hardware. The experimental setup consists of the following equipment. An electric load (RBL488 TDI Transistor Devices–Dynaload Division), an analog-to-digital converter board (National Instruments™ PCI-6024E with 12 bit resolution, 200 kS/s maximum sampling rate) and NI™ LabVIEW™ are used. The RBL488 load is adequate to test and analyze fuel cells with constant and transient power capabilities. Sensors are designed and installed to measure the stack voltage, and the current of the fuel cell stack and also the auxiliary load current. To accommodate the high voltage of the stack (from 26 to 50 V) to the adequate range for the A/D board, a simple resistor ladder with precision power film resistors (in 21:1 ratio) is implemented. Two closed-loop hall effect sensors (CLSM-50LA from F.W. Bell), which can pick up the current up to the frequency of 200 kHz, are installed for the net current and auxiliary current measurement. During the experiment, the oxygen excess ratio is not measured since there is no available space for the measurement of air flow rate before the cathode inlet. Also typical air flow rate measurement, for example, the thermal anemometry (hot wire) flow sensor can not be used for humid air after the humidifier.

Figure 4.2(a) shows the steady-state relation between the stack current and the stack voltage, or the polarization curve, of the experimental FC. The regions of activation, ohmic and concentration losses in voltage can be discerned in the voltage versus the stack current plot. The overall trend in the polarization curve is similar to Figure 2.1, which is determined by Equation (2.1). In the power-autonomous FC system, the auxiliary load affects the performance of the FC system. The power performance is determined by the stack characteristics and auxiliary power for the air blower and the cooling fan. As can be seen in Figure 4.2(b), the steady-state net power to the load is a function of the net load current of the FC, which is similar to Figure 3.3. The net power of the experimental FC increases monotonically as the net current increases to the rated maximum. Note here that the current density of the experimental FC is not shown because the active area of the cell is not disclosed from the manufacturer.

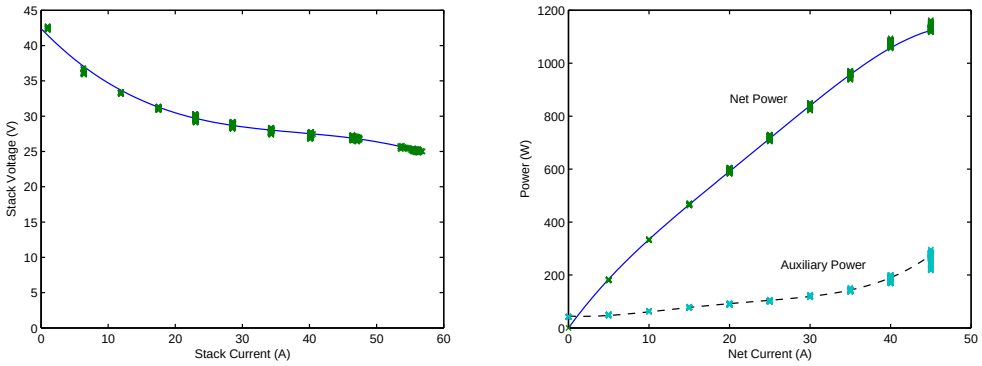

(a) Stack polarization (b) Fuel cell net power

Figure 4.2: Steady-state performance of the Nexa™ FC system

4.2 Experimental comparisons

Various models have been already proposed for the Nexa™ fuel cell stack system. A steady-state polarization model is presented and the cell-to-cell voltage variations are observed in [72]. System identification techniques are used for the parameterization of an equivalent electric circuit based on electrochemistry principles [10]. The parameters for the equivalent electric circuit of the Nexa™ are identified with impedance spectrum measurement. An equivalent electric circuit with static correction for the temperature effects is proposed [62].

The experiment is designed to show the transient responses of the voltage or the current of the FC during the net current or the voltage changes, respectively. Due to the differences in the power and the flow device used by FC in the model and the FC in the experiment, the experimental validation is performed qualitatively instead of comparing the exact measurement.

We achieve here only a qualitative confirmation of the model and controller using the experimental setup due to the differences between the fuel cells considered in the 75 kW fuel cell stack system model and the 1.2 kW power experimental set-up. Although the difference in the power range is important, the most important difference in the two systems is the operating pressure. The compressor-driven FC in the model operates at high pressures whereas the blower-driven FC in the Nexa™ experimental apparatus operates at low pressures. To compare the response of the two systems, the current and voltage load ranges for the simulation are chosen to be low (60/300 Amperes and 250/350 Volts) in order to ensure operation of low pressure range to avoid the effect of the cathode pressure variation.

4.2.1 Net current input

The experimental data during a command of net current input are shown in Figure 4.3(a). A net load current increase from 20 to 30 A is applied to the experimental FC within 0.02 second at 0.2 second. A pure step change in net current is not applied in order to avoid the effects of the

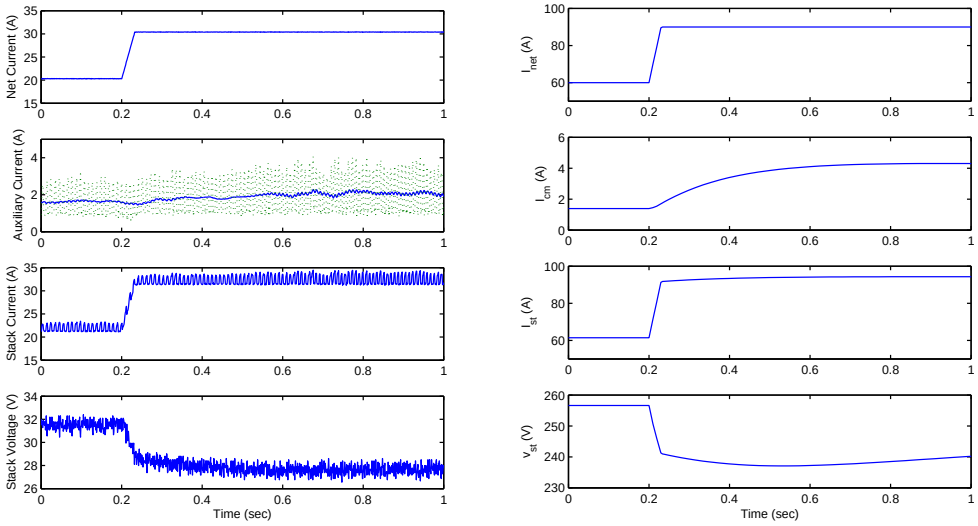

(a) Experimental result

(b) Simulation result

Figure 4.3: Experimental comparion - net current step

control logic in the electric load and the power cable between the stack and the load. The rate of change of $10/0.02 = 500$ A/sec is fast enough to excite the dynamics of the experimental fuel cell. When the net current load increases, the stack voltage immediately drops following the current input. Then there is a slow voltage decrease that matches the response of the measured auxiliary current which increases rather slowly as shown in Figure 4.3(a). Due to the slow auxiliary current increase, we postulate that a filtered feedforward controller similar to the one analyzed in Section 3.4 is used by the Nexa™ control system. In Nexa™ FC system, the air supply blower and cooling fan are actually controlled by a pulse width modulation (PWM) command and thus the auxiliary current measurement exhibits continuously pulsing results. The averaged current is calculated and plotted over the measured current.

Simulation is also performed during a change in net current from 60 to 90 A. The air supply control is based on feedforward control from the net current measurement. The first order filter is added to the feedforward control, which is shown in Section 3.4. The filter time constant $\tau_{filter} = 0.4$ second is chosen to match the dynamics of the auxiliary current load. As can be seen in Figure 4.3(b), the voltage dynamic behavior of the FC model is similar to the results of the experiment. The simulation result in the compressor motor load I_{cm}, the stack current I_{st} and voltage v_{st} supports our conjecture about the air supply control strategy in the Nexa™ .

4.2.2 Stack voltage input

A stack voltage input is also applied to the experimental FC, which is shown in Figure 4.4(a). When the stack voltage is used as the input of the system, the dynamic behavior of the stack current

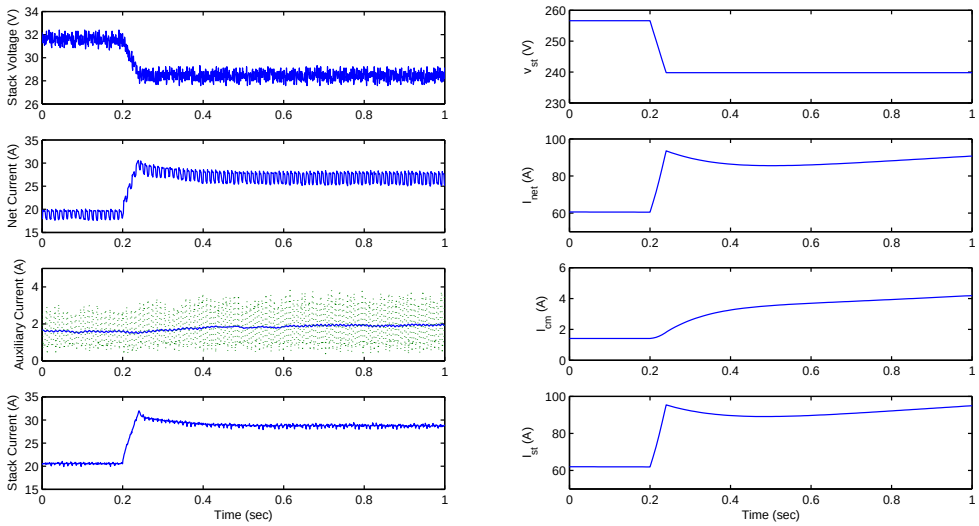

(a) Experimental result

(b) Simulation result

Figure 4.4: Experimental comparison - voltage step

represents the performance of the fuel cell system. Simulation results with voltage input are shown in Figure 4.4(b). Although the input of the fuel cell stack system is the stack voltage, the air supply dynamics of the fuel cell system are same as in the case of the current input model. The same air supply control is applied with filtered feedforward command based on the net load current measurement. Most features of the dynamic behavior of the experiment are predicted well with the simulation. The net current shows overshoot after the step voltage decrease, followed by the increase in auxiliary current load.

In the experimental comparisons with two different input situations, the model developed in Chapter 2 and the control design analyzed in Chapter 3 shows the ability to describe transient power performance of the FC. Here the oxygen excess ratio behavior is not verified experimentally due to the lack of OER sensor. Based on the transient responses in the net load current and the auxiliary load current, the changes in oxygen excess ratio are expected to be as in Figure 3.13(b). In the case of the experimental FC system, reducing the occurrence of large excursions in oxygen excess ratio is more critical due to the unknown pulsating loads typically observed in power supply applications. Thus, we postulate that the feedforward control is passed through a slow filter, and hence the initial excursion of the oxygen excess ratio is not affected by the air supply control during step changes in current or voltage. The advantage of filtered command in air supply is reduced disturbance ratio at high frequency current input (see Figure 3.13(a)), while the disadvantage is slower recovery after the initial excursion, as can be seen in Section 3.4. If there exists a supervisory controller that manages power drawn from the FC, high frequency current input can be filtered by the DC/DC converter while low frequency current disturbance rejection in regulating λ_{O_2} can be

achieved by the air supply control. The final two chapters cover these issues on integration of the FC with DC/DC converter and battery.

Chapter 5

DC/DC converters for fuel cell system

In this chapter, we present controller design and performance analysis of an autonomous FC power system which is augmented with a DC/DC converter for regulated voltage power source. We show that there is a tradeoff between the bus voltage regulation and oxygen excess ratio in the FC without hybridization. This combination of FC and DC/DC converter is applicable for the stationary system for back-up power or distributed power generation. In this case, the control objective of DC/DC converter is dedicated to boosting varying FC voltage to constant output voltage at the power bus. To investigate the coupled dynamics with currents and voltages in the fuel cell power system, it is necessary to establish an analytic model for the fuel cell with DC/DC converter and design the integrated system. In this chapter, it is shown that the dynamics of the DC/DC converter represents the coupling of currents and voltages of the fuel cell and the DC/DC converter.

We also present the control design for the bidirectional DC/DC converter. The control problem of bidirectional DC/DC converter arises when charging/discharging the battery to buffer the FC load. Control effects of the bidirectional DC/DC converter are not known yet, because the bidirectional DC/DC converter manifests the FC stack voltage and not the current, and the voltage dynamics of the fuel cell have not been discussed before. We show here control design of the bidirectional DC/DC converter for the FC hybrid architecture.

In the last part of this chapter, the effects of the DC/DC converter control on the fuel cell system and the DC/DC converter are shown. The decentralized control scheme is applied to individual controllers for the fuel cell system and the DC/DC converter. The current drawn from the fuel cell is determined by the closed-loop performance of the DC/DC converter. Using the DC/DC converter to shape the FC current can resolve the oxygen excess ratio regulation problem. Filtering the current from the FC limits the ability of the DC/DC converter to regulate the bus voltage, and thus it introduces a new tradeoff between oxygen excess ratio and bus voltage. The simulation results show that there is a tradeoff between the two performance objectives, FC oxygen excess ratio

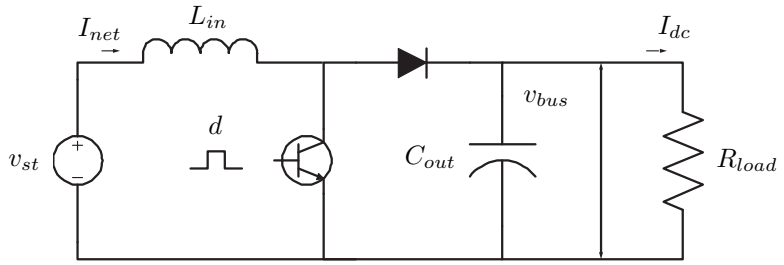

Figure 5.1: DC/DC boost converter

and the output voltage of the converter. Finally, a model-based, multivariable optimal controller is designed to moderate the performance conflict.

5.1 DC/DC converter

In this study, two kinds of DC/DC converter for fuel cell application are considered. First, the unidirectional DC/DC converter transforms the DC fuel cell stack power to output voltage-current requirements of the external power devices that connect to an FC system. Here we consider a boost converter (shown in Figure 5.1) that can be used in PEM fuel cell applications. The voltage and current at the DC/DC converter input are the FC stack voltage v_{st} and the net FC current I_{net}, respectively. In steady-state, the converter functionality can be described by

$$\begin{aligned} v_{st} I_{net} &= v_{bus} I_{dc}, \\ (1-d) I_{net} &= I_{dc}. \end{aligned} \tag{5.1}$$

The bus voltage v_{bus} and the output current I_{dc} are associated with the duty cycle d of the solid state switch in the circuit. The inductance of input inductor L_{in}, the capacitance of output capacitor C_{out} and the resistance of the load R_{load} are shown in Figure 5.1.

In the area of fuel cell power applications, bidirectional DC/DC converter is considered, specifically in a load-following fuel cell system that the FC power meets most of power demand while small-sized battery covers some transients and start-up/shutdown [70, 72]. Bidirectional converter has an ability to match high voltage fuel cells with low voltage battery when fuel cell is directly connected to the DC bus in a hybrid configuration, as shown in Figure 1.2(b). Figure 5.2 depicts one of the bidirectional converter topology for low voltage battery and high voltage DC bus.

5.1.1 DC/DC converter model

In this study, the DC/DC boost converter is selected for 50 kW power and based on 400 V output voltage with nominal input voltage is 250 V and thus nominal input current is 200 A. Ideally the input power is processed in a converter with 100 % efficiency. Actual efficiency is slightly less than 100 % due to the losses in the inductor, capacitor, transformer, switch and controller circuit. A

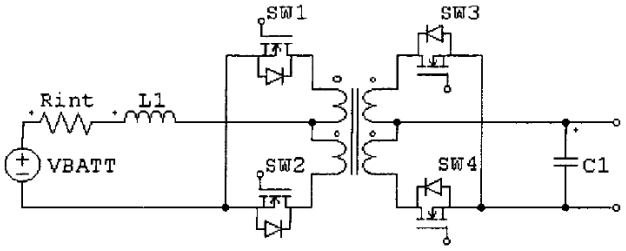

Figure 5.2: Bidirectional DC/DC converter [65]

typical boost converter for PEM fuel cell application has about 95 % efficiency when the voltage boost ratio is approximately two [67].

Increasing L_{in} reduces the ripple of the input current. Although large L_{in} protects the stack from high frequency AC current, the associated increase in resistance might decrease the converter efficiency. The size of C_{out} is usually determined by the ripple specification of output voltage. Other considerations such as the voltage and current limit of the capacitor should also be accounted especially due to high voltage and current values associated with FC applications. For the subsequent dynamic analysis, the values of inductor and capacitor are selected to be as $L_{in} = 1$ mH and $C_{out} = 1200$ μF.

An average nonlinear dynamic model can be used to approximate the boost converter switching dynamics [41]

$$\begin{aligned} L_{in}\frac{dI_{net}}{dt} &= v_{st} - (1-d)v_{bus}, \\ C_{out}\frac{dv_{bus}}{dt} &= (1-d)I_{net} - \frac{v_{bus}}{R_{load}}. \end{aligned} \tag{5.2}$$

The inputs to the converter, based on realistic FC operation, are the duty cycle d, the input voltage v_{st}, and the output current, $I_{dc} = v_{bus}/R_{load}$. Linearization and Laplace transformation from these inputs to the output voltage v_{bus} provide the following transfer functions [15]

$$v_{bus} = G_d(s)d + G_v(s)v_{st} - Z_{out}(s)I_{out} \tag{5.3}$$

$$G_d(s) = \frac{\frac{v_{bus,n}}{(1-d_n)R_{load,n}C_{out}}\left[\frac{(1-d_n)^2R_{load,n}}{L_{in}} - s\right]}{s^2 + \frac{1}{R_{load,n}C_{out}}s + \frac{(1-d_n)^2}{L_{in}C_{out}}}$$

$$G_v(s) = \frac{\frac{1-d_n}{L_{in}C_{out}}}{s^2 + \frac{1}{R_{load,n}C_{out}}s + \frac{(1-d_n)^2}{L_{in}C_{out}}}$$

$$Z_{out}(s) = \frac{\frac{1}{C_{out}}s}{s^2 + \frac{1}{R_{load,n}C_{out}}s + \frac{(1-d_n)^2}{L_{in}C_{out}}}$$

where d_n is the nominal duty cycle and $R_{load,n}$ is the nominal load resistance. The transfer function Z_{out} is called converter impedance and represents the effect of small load (current) changes to v_{bus}.

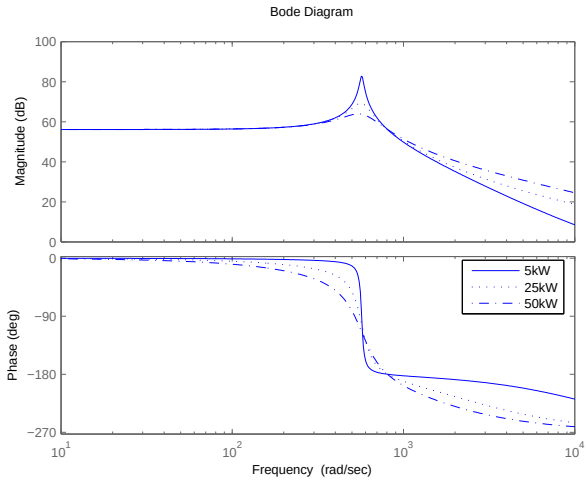

Figure 5.3: Open-loop dynamics of G_d for different load levels

As can be seen in the zero at the origin of Z_{out}, the steady-state output voltage is not affected by changes in load. This capability to reject load disturbances (variation in I_{out}) and regulate the output voltage (v_{bus}) is desirable. However, a zero at $s = 0$ corresponds to a derivative of the disturbance input causing large deviation in v_{bus} during a step change in load. Thus, although the zero at the origin helps the steady-state performance, it deteriorates the transient performance. The impedance can also represent the dynamics of R_{load} to v_{bus} when the electric load is purely resistive which is typical for automotive or backup power applications.

The output voltage dynamics depends on nominal power level and input voltage which are reflected in the open-loop transfer function through different d_n and $R_{load,n}$ values. It can be shown that the characteristic equation given by the denominator of the transfer function of the transfer functions in (5.3) has under-damped behavior for typical combinations of L_{in}, C_{out}, d_n and $R_{load,n}$. The damping ratio decreases when power increases or $R_{load,n}$ decreases in $\zeta = \frac{1}{2R_{load,n}(1-d_n)}\sqrt{L_{in}/C_{out}}$. The gain and phase Bode plots of the transfer function G_d in (5.3) shown in Figure 5.3 describes the open-loop dynamics (from control input d to performance variable v_{bus}).

Low damping of the open-loop dynamics causes undesirable output oscillations that can be reduced with judicious control design as discussed below. As the Bode plots indicate, the open loop converter has fast dynamics with natural frequency $\omega_n = (1-d_n)/\sqrt{L_{in}C_{out}}$ approximately at 1000 rad/sec. The fast converter dynamics cause abrupt changes in I_{net} and act as a disturbance to the fuel cell. Therefore, the converter control design has to reduce this high frequency disturbance to the fuel cell by providing damping, or in other words, filtering the current I_{net} drawn from the FC.

5.1.2 DC/DC converter control

The converter control objective is to maintain constant bus voltage despite variations in the load and the input (fuel cell) voltage. In the fuel cell application, the converter operates in large range of

power. We thus consider disturbances in $G_{load} = 1/R_{load}$ that can capture the large load variation better than the output current I_{out} formulation in Equation (5.3). Nonlinear control techniques in [16] were employed to handle large variations in converter loads. We employ linear control techniques similar to [15] and formulate the bus voltage regulation problem using the control structure in [25].

In the DC/DC converter model described in Figure 5.1 and Equation (5.2), the only control input is the duty cycle of the DC/DC converter. The duty cycle, the actual control command to the DC/DC converter, is controlled in order to achieve the following objectives: (i) protect the fuel cell system from abnormal load including transient and (ii) maintain the DC-bus voltage v_{bus}. In our case, the fuel cell is augmented with the DC/DC boost converter, matching the voltage of the DC-bus, v_{bus} to the desired value v_{bus}^{ref}. By changing the duty cycle, the net current of the fuel cell and the bus voltage can be regulated, but not independently from each other.

Figure 5.4 shows the controller design for a DC/DC converter. Dual loop control (voltage/current control) can be implemented for the DC/DC boost converter [41]. Both current of the fuel cell, I_{net} and voltage of the bus, v_{bus} are controlled by the feedback controller.

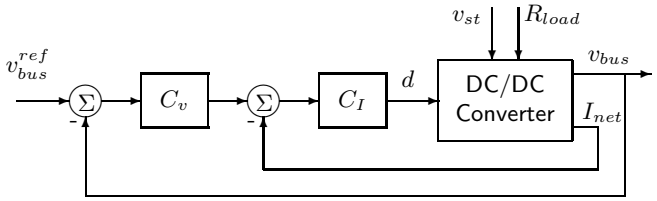

Figure 5.4: DC/DC boost converter control

In this control scheme, the outer loop controller C_v is composed of a proportional-integral (PI) controller for zero steady-state error in DC-bus voltage v_{bus}^{ref}. Then the output from C_v can be the virtual reference of I_{net}, which becomes the current drawn from the fuel cell when the converter connects to the fuel cell. Nonlinear logic such as slew rate limiter, saturation or any kind of filter can be added to shape the current from the fuel cell stack [67]. A proportional controller (P) is used for the net fuel cell current controller C_I. Both P and PI controllers for C_v and C_I, respectively, can be tuned sequentially using classical control techniques. The C_v and C_I controllers can also be tuned using single-input, single-output classical proportional, integral and derivative (PID) control tuning techniques for regulating v_{bus}. Indeed, adding a proportional feedback C_I around the I_{net} measurement is equivalent to a derivative controller around v_{bus} which is needed to dampen the typically under-damped DC/DC converter dynamics, which is shown in Section 5.1.1.

We choose to apply a model-based linear quadratic regulator approach after transforming the C_v and C_I controllers to state feedback as follows. The controlled duty cycle d is

$$d(s) = -K_{Dv} I_{net}(s) - K_{Pv} v_{bus}(s) - \frac{K_{Iv}}{s} v_{bus}(s) \tag{5.4}$$

and formulated as state feedback when an integrator q, where $dq/dt = v_{bus}$, is added for the v_{bus} regulation objective. The optimal state feedback gains K_{Dv}, K_{Pv} and K_{Iv} can be selected from a

linear quadratic regulator design [25]. The controller gains are derived based on the minimization of a quadratic cost function

$$J = \int_0^\infty \left[\begin{array}{cc} I_{net} & v_{bus} \end{array} \right] Q \left[\begin{array}{c} I_{net} \\ v_{bus} \end{array} \right] + u^T R u + q^T Q_I q \, dt. \tag{5.5}$$

With known gains, two equivalent controllers, C_v and C_i are separated

$$\begin{aligned} C_v(s) &= \frac{K_{Pv}}{K_{Dv}} + \frac{K_{Iv}}{K_{Dv} s} \\ C_I(s) &= K_{Dv}. \end{aligned} \tag{5.6}$$

Figure 5.5 shows simulation results of the boost converter with two degree of freedom controllers (solid line) and the open-loop performance (dashed line). The feedback controller gain is determined by the LQR weight matrix $Q = I$, $Q_I = 10000$ and $R = 0.1$. First, a step decrease of input voltage from 250 V to 225 V is applied to emulate fuel cell voltage which corresponds to 70 mV average cell voltage drop. During this change, shown in (a), the duty cycle d increases and draws more current from the input source. The performance variable v_{bus} recovers within 0.1 second. The controller can be tuned to handle the input voltage change faster at the expense of faster transient in current drawn from the fuel cell I_{net}. The graphs in column (b) show the closed-loop response during a load change. The load change corresponds to increase in power from 50 kW to 55 kW. In this situation, steady-state voltage regulation is not a problem because the DC gain of the impedance transfer function Z_{out} is zero as discussed in Section 5.1.1. Nevertheless, the controller we design reduces d for a short time. This decrease helps filter the sharp and oscillatory current in I_{net} that would have occurred otherwise (shown in dashed line). Here it can be observed that the closed-loop I_{net} increases and settles to the next steady-state level in both input voltage change and output power change. This behavior clarifies the causality between the fuel cell and converter dynamics, where the fuel cell becomes a current source in the output voltage regulation problem.

5.1.3 Bidirectional DC/DC converter model

In a case of load-following fuel cell hybrid system depicted in Figure 1.2(b), the major power flows from the FC to the load directly without a DC/DC converter. Here a small amount of battery current flows through the DC/DC. This configuration has an advantage on efficiency because it avoids the DC/DC converter losses. The size and power requirement for bidirectional DC/DC converter is thus relatively smaller than the ones for the DC/DC converter in Section 5.1.1. Here we consider 10 kW power bidirectional DC/DC converter that boosts 24 V battery power to the stack bus voltage, or charging the battery with fuel cell power.

Given the topology in Figure 5.2, the switches of the converter operate only in two different switching states, leading to the simplified analytic model shown in Figure 5.6. An averaged model

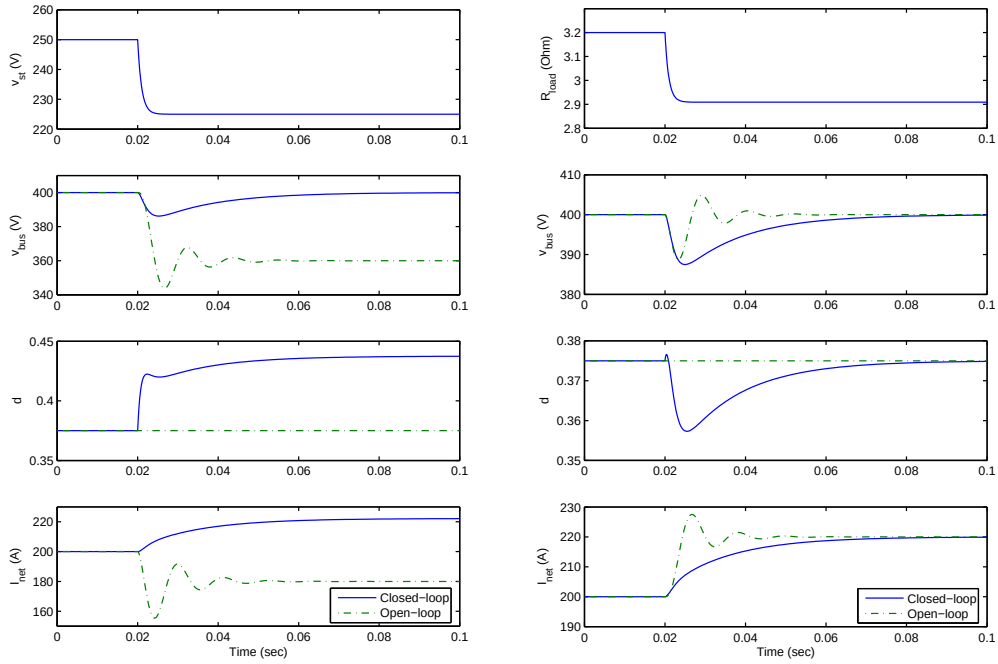

(a) input voltage change (b) load resistance change

Figure 5.5: Simulation results of the DC/DC converter

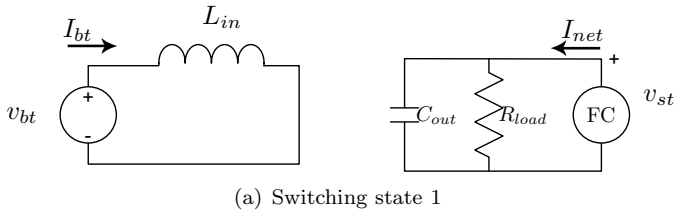

(a) Switching state 1

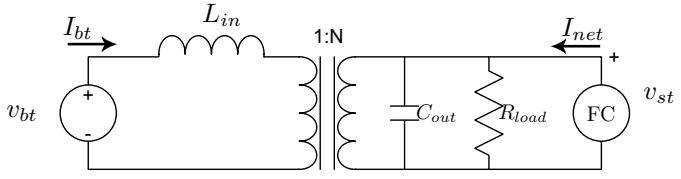

(b) Switching state 2

Figure 5.6: Bidirectional DC/DC converter model

based on duty cycle d can be described in [65]

$$L_{in}\frac{d}{dt}I_{bt} = -\frac{1-d}{N}v_{st} + v_{bt} \quad (5.7)$$

$$C_{out}\frac{d}{dt}v_{st} = \frac{1-d}{N}I_{bt} - \frac{1}{R_{load}}v_{st} + I_{net} \quad (5.8)$$

where v_{bt} is the battery voltage and I_{bt} is the battery current, respectively. For the subsequent dynamic analysis of the bidirectional DC/DC converter, the values of inductor and capacitor are selected to be as $L_{in} = 13$ μH, $C_{out} = 10000$ μF and the transformer ratio of $N = 5$.

Figure 5.7 shows open-loop dynamics of the bidirectional converter with respect to changes in load resistance R_{load}, fuel cell current I_{net}, battery voltage v_{bt} and duty cycle d. During the changes in the load resistance or fuel cell current, the stack voltage varies abruptly, which may increase in the fuel cell current also. The battery current changes much and stays away from zero when the other operating conditions vary. This can cause aggressive battery use especially when we consider small-sized, low voltage battery for load-following fuel cell configuration. By changing the duty cycle, the fuel cell stack voltage and the battery current can be regulated, but no independently from each other.

5.1.4 Bidirectional DC/DC converter control

The control objectives of the bidirectional DC/DC converter depend on the electric architecture. It was qualitatively described that the controller that splits load to the FC and battery can be achieved indirectly by adjusting bus the stack voltage using battery and bidirectional DC/DC converter [58]. The dynamics of bidirectional DC/DC converter are tied with the load current, fuel cell net current, battery voltage, and the control input, duty cycle d as can be seen in Equation (5.8).

Figure 5.8 shows the controller design for a bidirectional DC/DC converter. Dual loop control (voltage/current control) can be implemented, which is similar to the one shown in Section 5.1.2. Here both current of the battery, I_{bt} and voltage of the fuel cell, v_{st} are determined by the feedback controller. We can again choose to apply a model-based linear quadratic regulator approach after transforming the C_v and C_I controllers to state feedback as follows. The controlled duty cycle d is

$$d(s) = -K_{PI}I_{bt}(s) - K_{Pv}v_{st}(s) - \frac{K_{II}}{s}I_{bt}(s) \quad (5.9)$$

and formulated as state feedback when an integrator q is added for the I_{bt} regulation objective. The optimal state feedback gains K_{PI}, K_{Pv} and K_{II} can be selected from a linear quadratic regulator design. With known gains, the two equivalent controllers, C_v and C_I, are separated

$$\begin{aligned} C_I(s) &= \frac{K_{PI}}{K_{Pv}} + \frac{K_{II}}{K_{Pv}s} \\ C_v(s) &= K_{Pv}. \end{aligned} \quad (5.10)$$

The details in control results are shown with the hybrid configuration in Section 6.3.

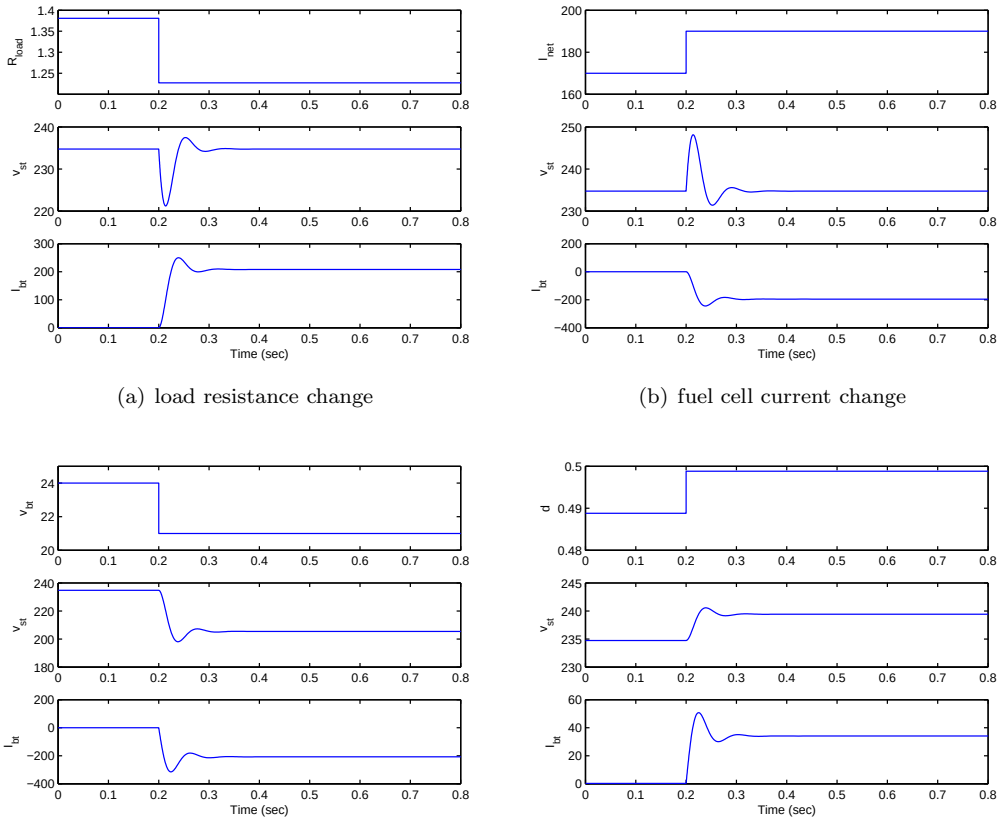

(a) load resistance change

(b) fuel cell current change

(c) battery voltage change

(d) duty cycle change

Figure 5.7: Open-loop simulation of the bidirectional DC/DC converter

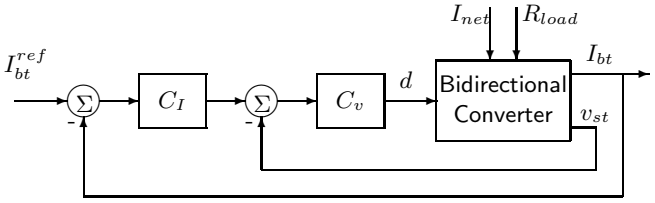

Figure 5.8: Bidirectional DC/DC converter control

5.2 Coordination of the DC/DC converter with the fuel cell

Here we first consider the integration of the fuel cell with the controlled compressor, and the controlled DC/DC converter in autonomous power supply. This integration exactly follows the hybrid configuration of the FC in Figure 1.2(a) except battery is not included. In an industrial application, the fuel cell with its compressor and compressor controller is viewed as one component and the DC/DC converter with its controller as another as shown in Figure 5.9(a). Typically, these two components are provided by different manufacturers based on some initial specifications. The two controllers are calibrated separately and small corrections are performed after the two components are connected. This control architecture is called decentralized, and the calibration is called sequential, because one controller is tuned and then the other is re-tuned to minimize interactions between the two components. The process is sometimes tedious and can be suboptimal even after many iterations.

Another tuning methodology that chooses the right calibration by taking into account the component interaction is called multivariable and results in a centralized controller as shown in Figure 5.9(b). Decentralized control is successful if there is minimal coupling between the two systems. In our case, the performance variables λ_{O_2} and v_{bus} are conflicting with each other and result in a challenging calibration problem.

5.2.1 Decentralized control

When the fuel cell with its compressor and compressor controller is viewed as one sub-system and the converter with its controller as another, two different control objectives, oxygen excess ratio regulation in the fuel cell and bus voltage regulation in the DC/DC converter are pursued by two controllers.

The control objective of regulating the oxygen excess ratio λ_{O_2} can be achieved by a combination of feedback and feedforward control by measuring the compressor air flow rate W_{cp} and the demanded load current I_{net}. Figure 3.18 in Chapter 3 shows the feedback and feedforward controllers which are designed to regulate the oxygen excess ratio in an autonomous fuel cell power system.

Regulating air flow in power-autonomous fuel cell system has inherent performance limitations. The volume of supply manifold including humidifier and heat exchanger after the flow meter causes significant lag or delay on regulating oxygen excess ratio inside the stack [52, 60]. On the other hand, using a large compressor control effort may overcome the limitation above at the risk of

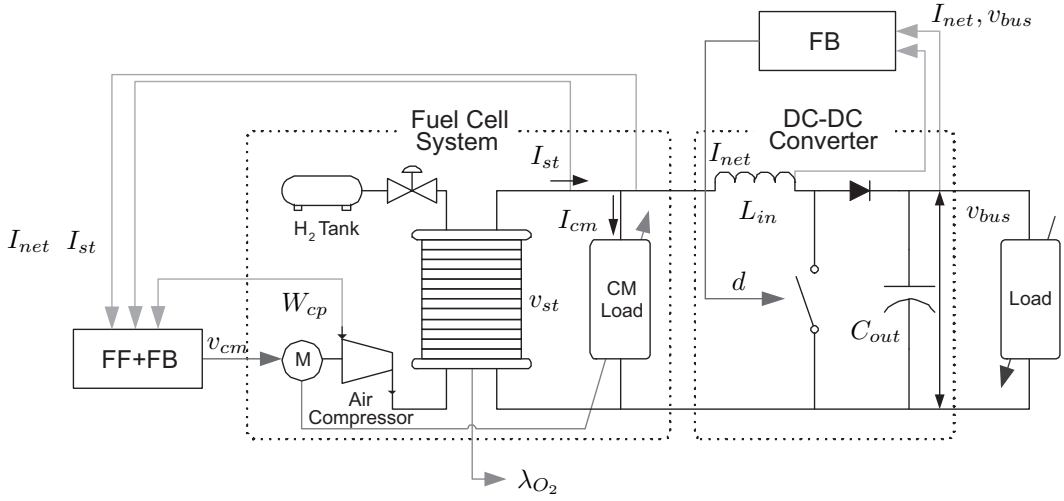

(a) Decentralized control scheme

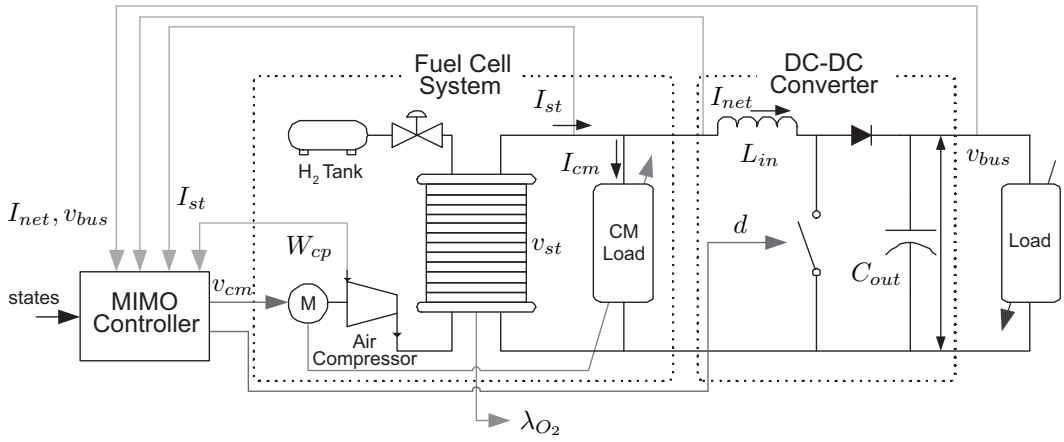

(b) Coordinated control scheme

Figure 5.9: Control schemes for fuel cell power system

causing instabilities when the compressor draws current directly from the stack [49]. These control performance and limitations in the FC air supply are analyzed in Chapter 3. The oxygen excess ratio λ_{O_2} regulation with combined feedforward/feedback control shows the best results within the inherent limitations. Then the load current to the fuel cell stack is shaped (filtered) to improve the performance of the closed-loop air supply dynamics. The selection of control gains in the DC/DC converter mainly handles the bus voltage regulation. This calibration allows us to modify the fuel cell current request based on its impact on oxygen starvation.

Figure 5.10 shows the simulation results of the fuel cell power system with two decentralized controllers during a step load resistance change to the DC/DC converter input. The step size of the resistance load change matches with the increase of the output power from 40 kW to 45 kW so that the output power reaches to the 45 kW when the bus voltage v_{bus} of the DC/DC converter settles to nominal value of 400 V. The net fuel cell current I_{net}, which is the output of the DC/DC converter and the input to the FC in Figure 5.10, is filtered as a results of the integration with DC/DC converter, but the net current overshoot with the effort of regulating the bus voltage, consequently affecting the oxygen excess ratio, that is the performance output of the FC. The compressor command v_{cm} is determined by the controller designed in Section 3.5.

As can be seen in dashed line in Figure 5.10, when the converter controller acts fast to regulate v_{bus}, there exists large excursion in λ_{O_2}. The control gain of the case DEC1 is determined by LQR weight matrix of $Q = I$, $Q_I = 1000$ and $R = 0.1$. The duty cycle d reacts faster after the step load change in R_{load} in order to regulate v_{bus}. The following increase in d causes a sudden current load I_{net} increase, which causes unacceptable λ_{O_2} excursion. The effect of load increase becomes severe due to the compressor current I_{cm} drawn from the FC, which can be estimated by observing the compressor input v_{cm}, the stack current I_{st}, and the net current I_{net}.

Detuning of the converter controller is necessary to avoid this fast interaction in the fuel cell. As can be seen from the result of the fuel cell controller in Chapter 3, reducing high frequency current load by changing the bandwidth of the DC/DC converter control is desirable to reduce large excursion in the oxygen excess ratio (see Figure 3.16). The solid line (DEC2) shows the simulation results after the detuning by the LQR weight matrix of $Q = I$, $Q_I = 100$ and $R = 0.1$. Now the duty cycle reacts slower than the tune of DEC1, filtering the FC net current and avoiding the large λ_{O_2} excursion. For these converter gains, the output voltage v_{bus} recovers slowly demonstrating performance tradeoffs between the oxygen excess ratio regulation and the bus voltage regulation. Full state feedback control is introduced in the next section to allow coordination between the DC/DC converter and the compressor controller and check if it is possible to improve further both performance variables λ_{O_2} and v_{bus}.

5.2.2 Full state feedback control

As we have seen in the previous section, the two performance outputs are conflicting. It is, thus, not clear if any control design can improve the performance of both outputs. A centralized, model-based controller is designed to define the optimal signals within the conflict. The approach is known as

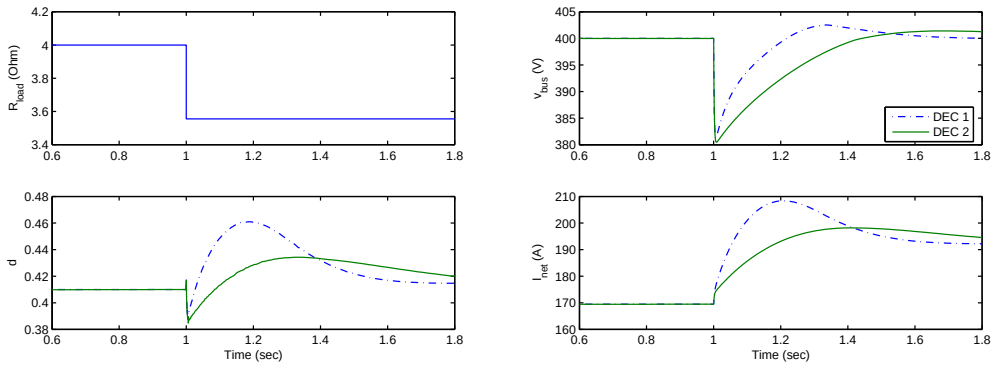

(a) DC/DC converter inputs

(b) DC/DC converter outputs

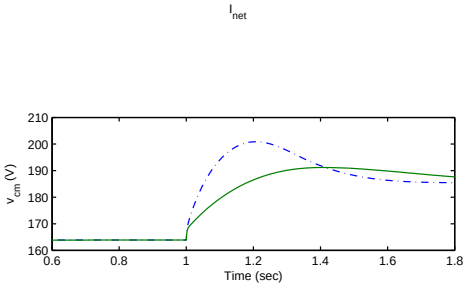

(c) Fuel cell system input

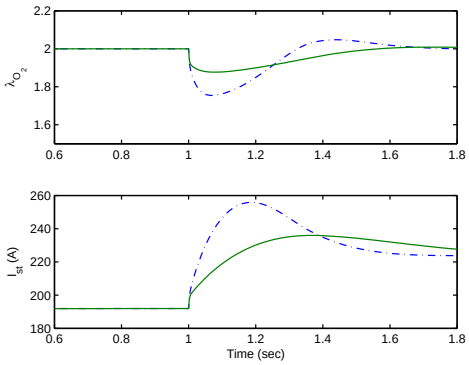

(d) Fuel cell system outputs

Figure 5.10: Simulation results of the nonlinear fuel cell power system model - decentralized control

linear quadratic regulator (LQR). We employ linearization of the state-space representation of the FC model in Chapter 2 and the static feedforward control design in Chapter 3, and the DC/DC converter of Section 5.1 at 40 kW power level

$$\begin{aligned} \dot{x} &= Ax + B_u u + B_w w \\ y &= C_y x + D_{yu} u \\ z &= C_z x + D_{zu} u \end{aligned} \tag{5.11}$$

where the state x, input u, disturbance w, measurement y, and performance variable z, are

$$\begin{aligned} x &= \begin{bmatrix} p_{O_2} & p_{N_2} & \omega_{cp} & p_{sm} & I_{net} & v_{bus} \end{bmatrix}^T \\ w &= G_{load} \\ u &= \begin{bmatrix} v_{cm} & d \end{bmatrix}^T \\ y &= \begin{bmatrix} W_{cp}^{ref} - W_{cp} & v_{bus}^m \end{bmatrix}^T \\ z &= \begin{bmatrix} \lambda_{O_2} & v_{bus} \end{bmatrix}^T. \end{aligned} \tag{5.12}$$

The units are pressure in bar, rotational speed in kRPM, mass flow rate in g/sec, voltage in V, and current in A. Note here that the static feedforward control from I_{net} measurement to the compressor control from Section 3.4 is included into the plant model above.

To eliminate steady-state error, integrators on the two measurements, $W_{cp}^{ref} - W_{cp}$ and v_{bus}^m, are added to the controller. And it is assumed that two outputs can be directly and instantaneously measured. The state equations of the integrators are

$$\frac{d}{dt} \begin{bmatrix} q_1 \\ q_2 \end{bmatrix} = \begin{bmatrix} W_{cp}^{ref} - W_{cp} \\ v_{bus}^m \end{bmatrix} \tag{5.13}$$

where W_{cp}^{ref} from Equation (3.7). The augmented plant, which combines the original states, x, and the integrator, q, is represented by

$$\dot{x}_a = \begin{bmatrix} \dot{x} \\ \dot{q} \end{bmatrix} = \begin{bmatrix} A & 0 \\ C_y & 0 \end{bmatrix} \begin{bmatrix} x \\ q \end{bmatrix} + \begin{bmatrix} B_u \\ D_{yu} \end{bmatrix} u + \begin{bmatrix} B_w \\ 0 \end{bmatrix} w = A_a x_a + B_{ua} u + B_{wa} w. \tag{5.14}$$

The optimal control law uses a state feedback with integral control

$$u = \begin{bmatrix} v_{cm} \\ d \end{bmatrix} = -K_{LQR} \begin{bmatrix} p_{O_2} \\ \vdots \\ v_{bus} \end{bmatrix} - K_{I,LQR} \begin{bmatrix} q_1 \\ q_2 \end{bmatrix}. \tag{5.15}$$

The sixteen unknowns elements of the controller gain K_{LQR} and $K_{I,LQR}$ are derived based on the

minimization of a quadratic cost function

$$\begin{aligned} J &= \int_0^\infty z^T Q_z z + u^T R u + q^T Q_I q \, dt \\ &= \int_0^\infty x_a^T \begin{bmatrix} C_z^T Q_z C_z & 0 \\ 0 & Q_I \end{bmatrix} x_a + u^T R u \, dt = \int_0^\infty x_a^T Q x_a + u^T R u \, dt \end{aligned} \tag{5.16}$$

that explicitly depends on the performance variables λ_{O_2} and v_{bus} through the weights Q_z, Q_I and R. The actuator cost is added to the cost function through the weight R to prevent excessive actuator inputs, which is especially useful for the air compressor controller. Different coefficient in Qs and R can be applied in J for tuning the optimal control law (5.15), so that the control gain is

$$\begin{bmatrix} K_{LQR} & K_{I,LQP} \end{bmatrix} = R^{-1} B_a^T P \tag{5.17}$$

where P is the solution to the Algebraic Riccati Equation (ARE)

$$P A_a + A_a^T P + Q - P B_a R^{-1} B_a^T P = 0 \tag{5.18}$$

which can be solved using MATLAB.

The linear simulation result of the coordinated controller is shown in Figure 5.11. The detuned decentralized controller (DEC2) is also shown with dash-dot line for comparison. Same step resistance change input is applied intending to increase output power from 40 kW to 45 kW. The centralized controller CEN is tuned to match the v_{bus} settling of the detuned, decentralized controller DEC2, but performs considerably better than the decentralized controller in regulating λ_{O_2}. The relatively slow recovery of λ_{O_2} from CEN controller is a drawback, but λ_{O_2} excursion is reduced significantly. The voltage recovery of the centralized controller CEN1 ensures 5 kW power increase in 0.4 seconds same as the decentralized controller. The control strategy based on LQR design can be observed with the response the duty cycle d in the solid line. The duty cycle initially drops to protect the FC while waiting for the air supply to increase. When the compressor ramps up then d increases rapidly to recover the output voltage v_{bus}.

The responses shown in this section is based on the assumption that all system states x are known. In practice, a state estimator (or observer) is needed to estimate the system state $\hat{x}$ from available measurements y. The design of a state observer is presented in the following section.

5.2.3 Observer design

The estimate of the state $\hat{x}$, used in the calculation of the control input (Equation (5.15)) is determined by a state observer based on Kalman filter design. Besides the measurements for integrator states, which are $y_1 = W_{cp}$ and $y_2 = v_{bus}$, the FC system and the DC/DC converter has available measurements such as $y_3 = I_{st}$, $y_4 = v_{st}$ and $y_5 = I_{net}$. Also supply manifold pressure $y_6 = p_{sm}$ is

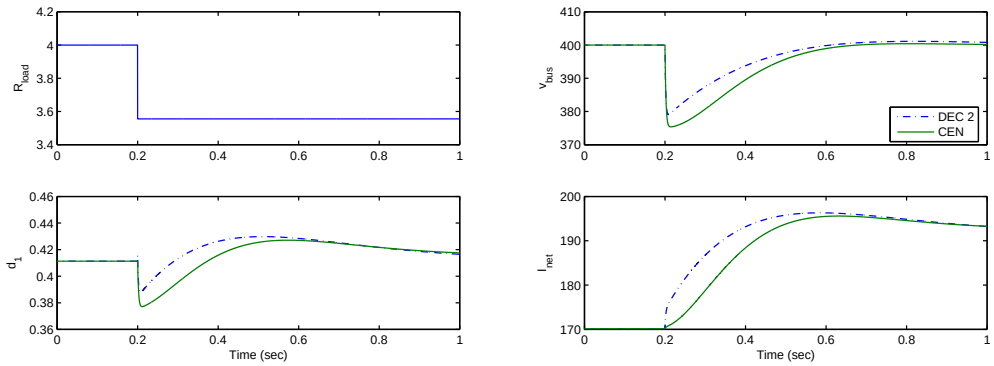

(a) DC/DC converter inputs

(b) DC/DC converter outputs

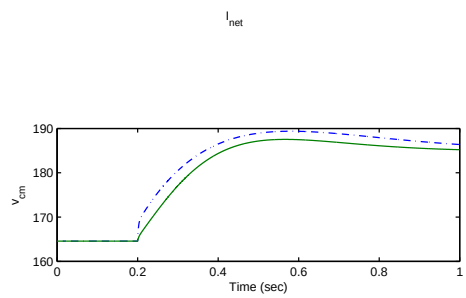

(c) Fuel cell system input

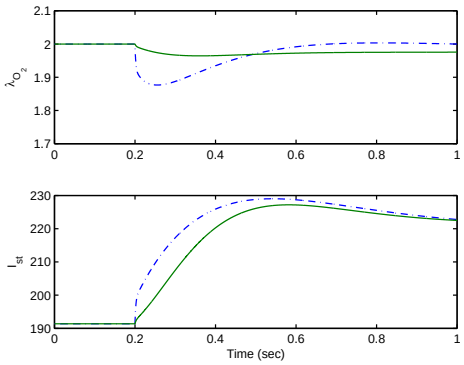

(d) Fuel cell system outputs

Figure 5.11: Simulation results of the linear fuel cell power system model - centralized control

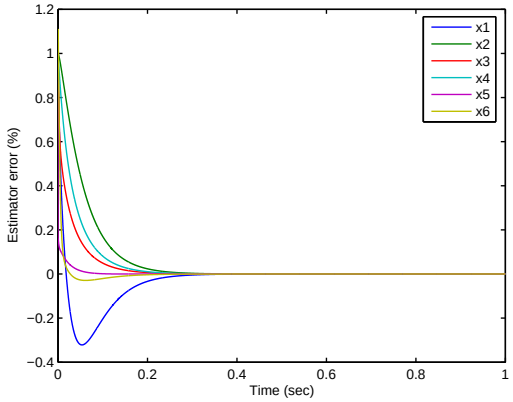

Figure 5.12: Observer state error

measured. The observer state equations are

$$\begin{aligned} \dot{\hat{x}} &= A\hat{x} + B_u u + B_w w + L(y - \hat{y}) \\ \hat{y} &= C_y \hat{x} + D_{yu} u \end{aligned} \tag{5.19}$$

Based on the Linear Quadratic Gaussian method, the optimal gain L is

$$L = SC_y^T W_y^{-1} \tag{5.20}$$

where S is the solution to dual of the ARE

$$SA^T + AS + V_x + SC_y^T W_y^{-1} C_y S = 0. \tag{5.21}$$

The positive definite matrices, V_x and W_y, represent the intensities of process and measurement noises, respectively. The weight matrices chosen are

$$\begin{aligned} V_x &= \text{diag} \begin{bmatrix} 1 & 1 & 1 & 1 & 1 & 1 \end{bmatrix} + \alpha B_u B_u^T \\ W_y &= 1 \times 10^{-3} \text{diag} \begin{bmatrix} 1 & 1 & 1 & 1 & 1 & 1 \end{bmatrix}. \end{aligned} \tag{5.22}$$

The V_x is in the form used in the feedback loop recovery procedure [14]. Using this procedure, the full state feedback loop gain properties can be recovered by increasing the value of α. The value of α chosen in this design is 1×10^{-1}. Figure 5.12 shows the response of observer error based on the measurements in linear simulation. The initial errors of all states are set at 1% of deviation from nominal points.

The nonlinear simulation of the system with output observer feedback is shown in Figure 5.13. A step change in resistance input is applied intending to increase the output power from 40 kW to 47.5 kW. The bus voltage recovery and λ_{O_2} excursion of the output-based CEN matches with the

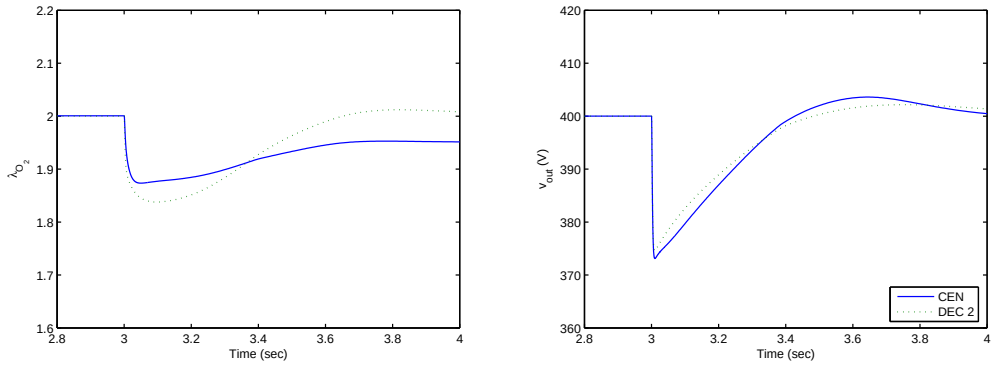

(a) Oxygen excess ratio

(b) Output voltage

Figure 5.13: Simulation results of the nonlinear fuel cell system model - observer based control

performance achieved with DEC2, with minor improvement in λ_{O_2} excursion. The oxygen excess ratio shows less deviation with CEN, but the penalty comes with the bigger output voltage drop.

Based on the nonlinear simulations and baring in mind that there will be a small mismatch between the model used to design the centralized controller and the plant, we conclude the following. The coordination between the air supply compressor and the DC/DC converter controllers cannot outperform a well tuned decentralized controller, especially, when the tuning of the DC/DC converter controller is based on the understanding the FC stack system limitations. This understanding can be established by the methodology of Chapter 3, applied to a FC model of Chapter 2.

The optimal control tuning based on the quadratic cost function in (5.16) manages the oxygen excess ratio from the communication and coordination in the system. However, the consequence of the increase in the bus voltage drop in Figure 5.11 raises questions associated with the power quality. The performance of the controller needs be evaluated with the load profiles for the specific applications, and the vehicle propulsion loads will be applied to compare the performance of the decentralized and multivariable controllers in Chapter 6.

Chapter 6

Control of FC hybrid electric vehicle

This chapter presents details of the electric configuration and control in the fuel cell hybrid system, performing system analysis with transient response characteristics. First, the control methodology for FC air supply and DC/DC converter in Chapter 5 is extended to the FC hybrid vehicle configuration in Figure 1.2(a). Hybridization in FC system with added battery offers more degrees of freedom on the system performances, which depends on the controller architecture and strategy. As a result, it is expected that battery added to support the voltage bus will relieve the major conflict between regulating λ_{O_2} and v_{bus} shown in Chapter 5. On the other case, added battery will affect the performance of the fuel cell along with the bidirectional DC/DC converter in the configuration of Figure 1.2(b). In both cases, control of the (unidirectional or bidirectional) DC/DC converter manages the power split between the FC and the battery in hybrid configurations.

In this chapter, the FC hybrid models comprising of the fuel cell, the DC/DC converter and the battery are developed. Complete forward-facing, causal models for a fuel cell hybrid vehicle are designed for component evaluation and detailed control simulation. The performance is evaluated for each component and system in dynamic simulation of the forward-facing model. Interactions among the driver command, vehicle dynamics, traction motor load, DC/DC converters, battery and fuel cells are highlighted. The baseline performance with decentralized controller is established and multivariable control design also is applied and compared as is in Chapter 5, assessing the effects of control calibrations.

Specifically, the air-supply sub-system and its dynamic control is implemented and evaluated during simulation analysis. The model captures the dynamic effect of the air supply compressor, which results in major power losses in a direct hydrogen fuel cell system. The different control strategy and tuning for the DC/DC converter is considered to achieve the power split and fuel cell protection. To focus on the modeling and control of FC hybrid power system, a battery model, which can capture the dynamic behavior between voltage-current relations, is used.

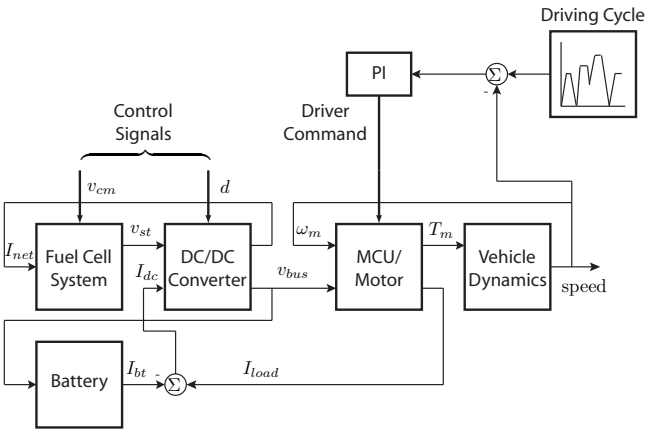

Figure 6.1: FC HEV powertrain causality flowchart (a)

In this work, regenerative braking is not included to concentrate on the interaction between the FC, battery and the load. The model for regenerative braking can be added to charge the battery by the current from the motor after isolating the fuel cell. The electric architectures considered in this work is also applicable to auxiliary power unit (APU), which usually has no energy recovery devices, by replacing the vehicle propulsion load with other electric loads. Cold start and shut-down are not considered in this work.

6.1 Fuel cell hybrid vehicle models

The fuel cell hybrid vehicle models in this chapter include not only the forward-facing vehicle and traction motor model but also complete causal models for the fuel cell system in Chapter 2 and 3, the DC/DC converter in Chapter 5 and the battery.

Figure 6.1 depicts the causal flow chart of a fuel cell hybrid vehicle model in the electric architecture of Figure 1.2(a). The fuel cell system model in this work captures dynamic performance in power including effects of parasitic losses. As can be seen in the block diagram of the fuel cell system, the disturbance input to the fuel cell system is the net current I_{net} and the performance output is the stack voltage v_{st}. The model also predicts oxygen starvation from the dynamics of its air supply system. In the causality flowchart, the fuel cell system model includes air supply system with flow and electric coupling from the input command of air compressor motor, which is developed in Chapter 2 and 3. The compressor command input v_{cm} is controlled to prevent oxygen starvation during the vehicle operation.

The DC/DC converter maintains the bus voltage that supplies power to the inverter/motor and auxiliaries, and the battery matches additional power for the load or captures the remaining power from the fuel cell. The dynamic model of DC/DC converter developed in Section 5.1.1 is applied, so that the DC/DC converter connects the fuel cell system with the battery and the vehicle propulsion load with the duty cycle input d. The disturbance inputs of the DC/DC converter model are the

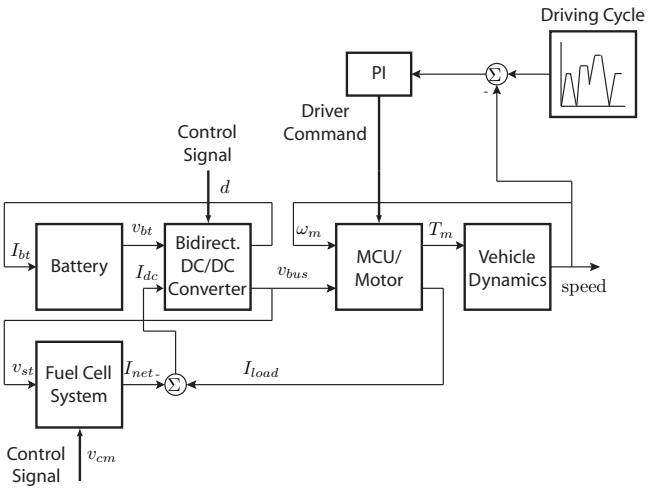

Figure 6.2: FC HEV powertrain causality flowchart (b)

fuel cell stack voltage v_{st} and the DC/DC output load current I_{dc}. The outputs of the DC/DC converter model are the fuel cell net current I_{net} and the bus voltage v_{bus}. The load current to the DC/DC converter, I_{dc} is defined from the traction load current I_{load} and the battery current I_{bt}, or $I_{dc} = I_{load} - I_{bat}$. Thus the traction power is drawn from the fuel cell and the battery. Here the battery is modeled with the voltage input v_{bus} and the current output I_{bt}.

Figure 6.2 depicts another causal flowchart of the fuel cell hybrid vehicle model in the electric architecture Figure 1.2(b). In this case, the DC bus line is directly linked with fuel cells, leading to varying bus voltage [32]. This configuration is realized in hardware with the bidirectional DC/DC converter located between the battery and the load. Although the flow chart looks similar to the one in Figure 6.1, the major difference is that the positions of fuel cell system and battery, which are switched with each other. The inputs and outputs of the FC and battery are also switched, such that now input of the fuel cell system is the stack voltage v_{st} instead of I_{net}. The control of the bidirectional DC/DC converter manages battery current I_{bt}, and thus the voltage of the fuel cell stack is controlled. In the two causal flowcharts, the motor, motor control unit (MCU) and vehicle parts are commonly used.

6.1.1 Motor, motor control unit and vehicle model

In an FC electric hybrid drive train, the driver control command directly manipulates the torque/power of the traction motor. In actual vehicle, the driver command is interpreted as a variable frequency/amplitute command through the DC/AC inverter and AC machine. In this work, inverter, motor and control unit are modeled as a DC motor with the driver torque demand, the speed of the motor ω_m and the DC-bus voltage v_{bus} as inputs and the load current I_{load} as output. The values of the traction motor parameters are shown in Table 6.1.

The motor torque T_m generated following the driver command forms the traction force of the

Table 6.1: Traction motor parameters

Variable	Value
Traction motor constant	0.15 V/(rad/sec)
Traction motor constant	0.15 N-m/A
Resistance	0.002 Ω

Table 6.2: Baseline vehicle characteristics

Variable	Value
Total vehicle mass	1591 kg
Aerodynamic drag coefficient	0.312
Frontal area	2.06 m^2
Rolling resistance coefficient	0.02
Radius of wheel	0.3 m
Accessory load	500 W

vehicle. The vehicle speed is the output of first order vehicle dynamics associated with its mass and other parameters through the traction force. In driving cycle simulation, the driver command is the output from a proportional-integral (PI) controller that is designed to track the speed of a given cycle. For this study, the fuel cell hybrid vehicle characteristics are assumed to be based on a compact sedan. The values of the parameters for the vehicle model are shown in Table 6.2.

6.1.2 Battery model

The battery current is determined by an internal resistance model

$$v_{bt} = v_o - R_{int} I_{bt}. \tag{6.1}$$

The battery open circuit voltage v_o and the internal resistance R_{int} are static functions of the battery state of charge (SOC) as shown in Figure 6.3 (a) and temperature T. The internal resistance of the battery also changes with sign of the current, or charging/discharging as shown in Figure 6.3 (b).

Assuming the battery is placed in parallel with the DC/DC converter, as shown in Figure 6.1, the terminal voltage of each battery module is determined by the DC/DC converter ($v_{bt} = v_{bus}/31$) and the battery current is then

$$I_{bt} = \frac{v_o(SOC, T) - v_{bt}}{R_{int}(SOC, sign(I_{bt}), T)}. \tag{6.2}$$

Table 6.3: Battery parameters

Variable	Value
Capacity	18 Ah
Charging efficiency	0.9
Maximum allowable voltage	16.5 V
Minimum allowable voltage	9.5 V

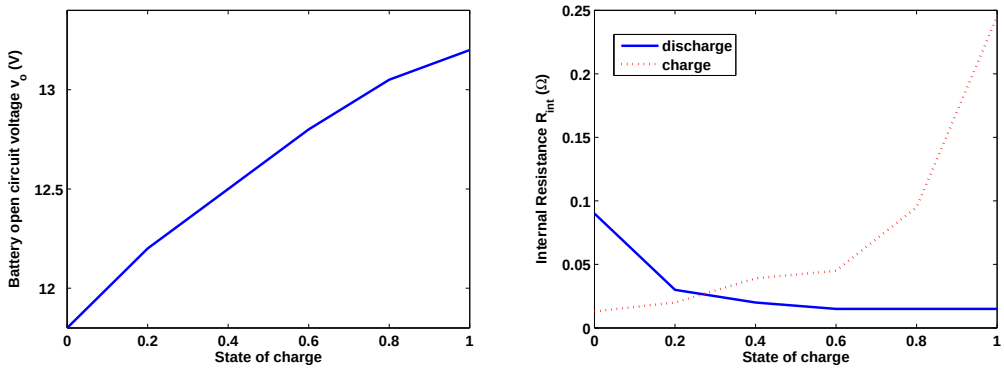

(a) Battery open circuit voltage v_o

(b) Internal resistance R_{int}

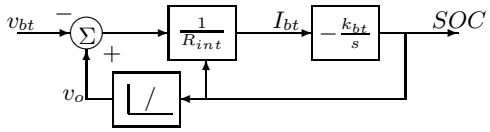

(c) Block diagram

Figure 6.3: Battery model

Here we assume that the battery temperature is maintained constant with an external cooling circuit. The battery parameters are based on the Lead-Acid type battery in ADVISOR model [35] and summarized in Table 6.2.

The SOC is calculated from the battery current and the capacity of the battery ($1/k_{bt}$)

$$\frac{dSOC}{dt} = \begin{cases} k_{bt} I_{bt} & I_{bt} \geq 0 \\ -\eta_{bt} k_{bt} I_{bt} & I_{bt} < 0 \end{cases} \tag{6.3}$$

where η_{bt} is the battery charging efficiency. Figure 6.3 (c) shows the block diagram of the battery model and the relationship between the battery parameters, R_{int} and v_o, and the state of charge.

To ensure proper shut down and start-up power from the battery, the battery should remain half charged. The SOC of each of the 31 battery modules is indeed maintained at 0.6 as shown later by regulating the bus voltage at 400 V. Note that at SOC=0.6 a battery module has open circuit voltage of 12.9 V (Figure 6.3 (a)), thus 31 modules at SOC=0.6 can be connected in parallel with the 400 V bus.

6.2 Control of FC hybrid power - part (a)

We first consider decentralized control as in Chapter 5, combining the fuel cell with its compressor and compressor controller and the DC/DC converter with its controller as another. Two different control objectives, oxygen excess ratio regulation in the fuel cell and bus voltage (or battery SOC) regulation in the DC/DC converter are pursued by two controllers.

The dynamic coupling between the voltages and currents among the fuel cell, battery and the traction load is captured by a dynamic model of the DC/DC converter as shown in the electric hybrid configuration of Figure 6.1. A DC/DC converter controller is then designed to boost and regulate the voltage at the converter output. Good regulation of the voltage at the converter output is typically achieved by large current drawn from the fuel cell and it is typically followed by small currents drawn from the battery. The converter controller can be tuned to avoid causing abrupt current draw from the fuel cell. In this work, various DC/DC converter controller gains result in different levels of power split between the fuel cell and the battery. It is thus possible to assess the effects of control calibrations on the power split, FC oxygen excess ratio, compressor behavior, and vehicle efficiency.

In the last section, we introduce coordination between the DC/DC converter controller and the FC controller, which follows the one in Chapter 5, into a combined system controller with optimal gains that emulates an FC load-following power split scenario. The centralized control accounts for the limitations in the fuel cell system and allows us to construct a controller for the smallest possible power assist level without compromising the fuel cell operation. The results of fuel economy and battery sizing with the dynamic model and control in this work provide insight on the necessary hybridization of a fuel cell power system without employing cycle-dependent optimization.

6.2.1 Hybrid power management

The control objectives for fuel cell hybrid power train are as follows: (i) protect the fuel cell system from abnormal load including transient (ii) maintain state of charge of the battery (iii) maintain the DC-bus voltage v_{bus} (iv) regulate the current (from both the fuel cell and battery) to the optimized values if supervisory control demand exists. A control strategy for splitting power between the fuel cell and the battery is implemented based on controlling the duty cycle of the DC/DC converter. In our case, the fuel cell is augmented with the DC/DC boost converter, matching the voltage of the DC-bus, v_{bus} to the desired value v_{bus}^{ref}. By changing the duty cycle, the net current of the fuel cell and the voltage of the battery which is equal to the bus voltage can be regulated, but not independently from each other.

Dual loop control (voltage/current control) is applied for the DC/DC boost converter as shown in Chapter 5 (see Figure 5.4). Both current of the fuel cell, I_{net} and voltage of the bus, v_{bus} are controlled by the feedback controller. Regulating v_{bus} to a v_{bus}^{ref} is equivalent to regulating I_{bt} to zero due to the integration achieved naturally through the battery state of charge (see Figure 6.3). The regulation at zero battery current ensures that the battery serves as a power assist device without an explicit supervisory controller.

If there is a pre-defined current command from the supervisory control or fuel cell system itself, the current loop (inner loop), C_I control can be used without the outer loop C_v. The demanded current can be drawn from the fuel cell as fast as the control bandwidth of the inner loop allows. The supervisory command may decide the fuel cell current for optimal efficiency in terms of energy management or dynamic FC limitations such as oxygen starvation. Many FC manufacturers bundle

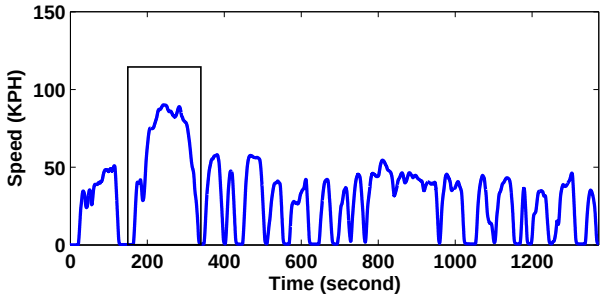

Figure 6.4: Vehicle speed on the FTP cycle

their FC with a fuel cell controller unit that broadcasts the maximum FC current that is safe to draw from the FC. This signal can then be used with the inner loop controller C_I, eliminating the C_v controller. Nonlinear logic such as a slew rate limiter, saturation or filter can be added to shape the current demanded from the fuel cell stack. However, current control can lead to conservative operation of the fuel cell or excessive battery use. Due to the complexity and uncertainty in the fuel cell system, control of battery current has lower priority most times. Thus it is necessary to implement high fidelity logic that can handle the fuel cell and battery performance with extensive optimization.

The outer loop through the selection of C_v gains mainly handles the bus voltage regulation if there exists no supervisory control command. We define the DC/DC converter loop time constant τ_{dc} as the time needed to regulate v_{bus} within 63 % of v_{bus}^{ref} after a load disturbance I_{dc}. This time constant also defines how fast I_{net} is drawn from the FC and should be tuned to match the dynamic performance of the fuel cell system. The C_v calibration allows us to modify the fuel cell current request based on its impact on oxygen starvation or other dynamic limitations. The dual loop controller in (5.4) shows that the dual loop can manage the fuel cell system and battery performance in hybrid power and achieve different power split levels depending directly on the controller C_v gains and the achieved closed loop time constant τ_{dc}.

6.2.2 Effects of control strategy on fuel efficiency and hybridization level

The simulation results from the causal model for the fuel cell hybrid powertrain show the impact of different sub-system control designs on the hybrid design. Two different control calibration emulating load-following and load-leveling scenarios were designed to demonstrate the characteristic of the fuel cell operation. Both control strategies use decentralized control to show the effect of controller design on the performance of oxygen supply and power split. Simulation comparison is performed first using the FTP (Federal Test Procedure) driving cycle, which emulates an urban route as shown in Figure 6.4. Battery and FC sizes are fixed in the simulation analysis to concentrate on the effect of the control strategy (effect of C_v calibration).

Figure 6.5 shows the simulation results for a portion of the FTP driving cycle with two different power control calibrations. First a controller calibration, that results in a load-leveling FC hybrid,

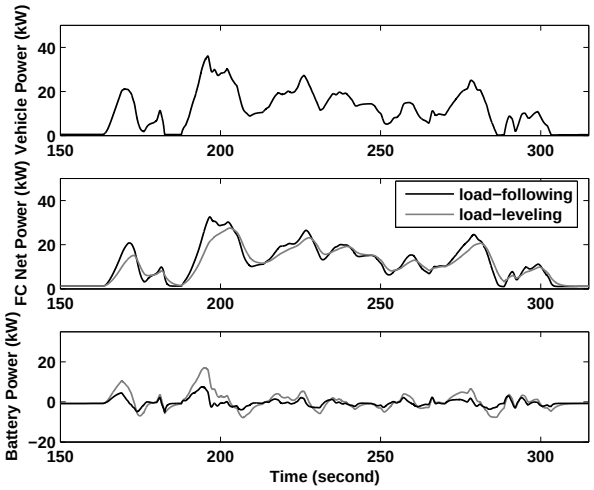

Figure 6.5: Power split in the FTP driving cycle with respect to control calibration

is considered which uses limited FC power and relies on transient power from the battery. The power split is achieved by the DC/DC converter control in (5.4) with low bandwidth (τ_{dc}=2 s) in the voltage loop. The other strategy shown is a load-following FC, which uses the FC power to the maximum whenever needed. The control calibration was performed by changing the bandwidth of the DC/DC converter response, i.e., fast response of the DC/DC converter for load-following FC operation (τ_{dc}=0.6 s).

During cycle simulation, the operating characteristics of the FC hybrid vehicle depend on the control calibration. Although both the load-leveling and load-following FC hybrid show limited FC net power below 36 kW, maximum power from the battery differs from 17 kW (load-leveling) to 7.5 kW (load-following). As can be seen in Figure 6.5, battery power is mostly used as transient power assist in load-leveling FC hybrid.

The changes in control calibration have limited effect on the fuel cell in the case of FTP driving cycle (mild power demand), leading to FC usage up to current density of 0.43–0.53 A/cm^2 as can be seen in Figure 6.6 (a) and (b). Even though load-following operation of FC shows higher power use in FC (0.53 A/cm^2), the histogram distribution (in the bar graph) shows similar overall characteristics. In both cases, the FC operates in the region of system efficiency over 45 %.

Simulation comparison is also performed on a portion of the US06 driving cycle which represents driving with hard-acceleration and high power demands as shown in Figure 6.7. Figure 6.8 shows the simulation comparison with two different power control calibrations during the portion of the US06 cycle. During aggressive demands in propulsion power, the operating characteristics of the FC depend on the control strategy. The load-leveling FC hybrid shows limited FC power up to 40 kW and uses battery power up to 30 kW. The load-following FC tuning uses FC power to satisfy approximately the maximum transient vehicle power demand of 50 kW.

In both cases, accurate air-supply and power-assist ensure regulation of oxygen supply in safe

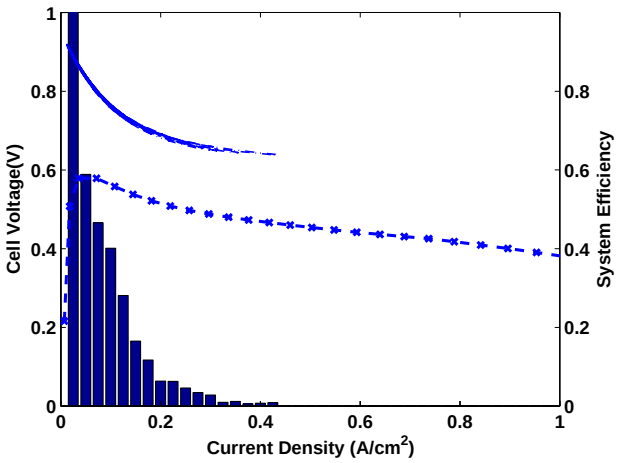

(a) Load-leveling FC

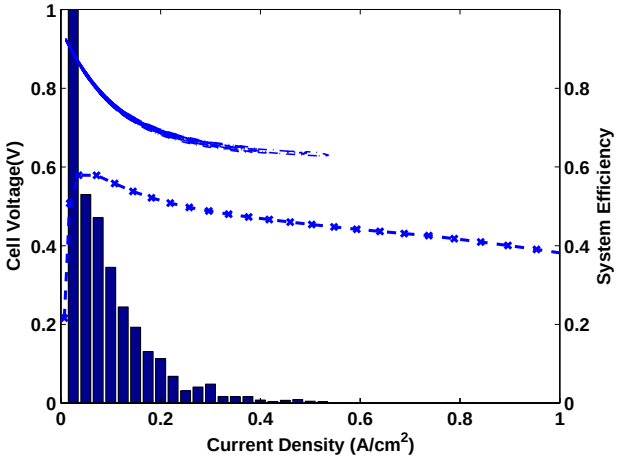

(b) Load-following FC

Figure 6.6: System efficiency (-x-), FC response ($\cdots$) and distribution (bar) for the FTP cycle

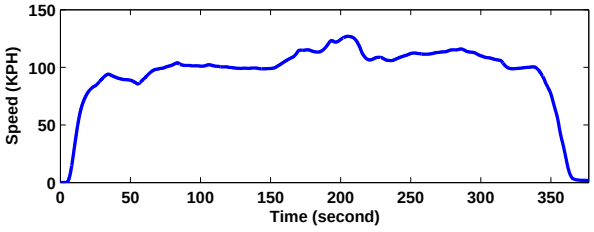

Figure 6.7: Vehicle speed on a portion of the US06 cycle

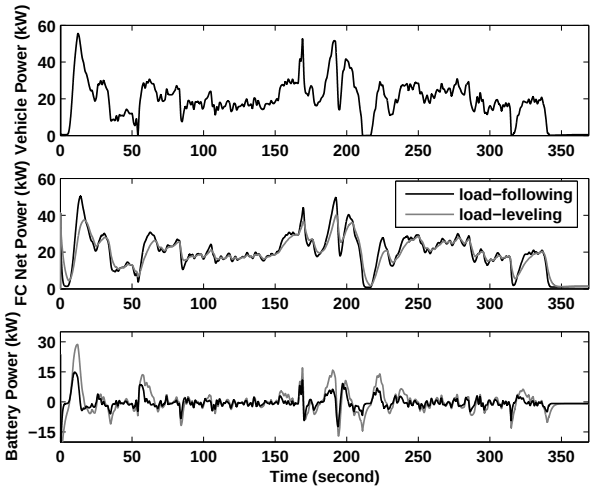

Figure 6.8: Power split in a portion of US06 driving cycle with respect to control calibration

regimes as can be seen in Figure 6.9 (a) and Figure 6.10 (a). The oxygen excess ratio λ_{O_2} is well regulated around the desired setpoint ($\lambda_{O_2}^{ref} = 2$) without large excursion, which could cause oxygen starvation. The regulation is achieved despite the large currents drawn from the fuel cell, 0.7 A/cm^2 and 1 A/cm^2 for the load-leveling and load-following calibrations as shown in Figure 6.9 (b) and Figure 6.10 (b). As the power demand of the traction motor changes, deficit power from fuel cell is naturally covered by the battery for a short while. Battery current is not used when power from the fuel cell follows the motor load. The changes in SOC of the load-leveling system are larger than that of load-following system, but battery usage for power-assist is minimal in both cases as intended.

It is observed that the hydrogen fuel economy is almost invariant to the control tuning, being 66–67 MPGE (miles per gallon equivalent to the energy stored in one gallon of gasoline) on the FTP cycle and 44 MPGE on the US06 cycle as can be seen in Figure 6.11. As it is shown in Figures 6.6, 6.9 (b) and 6.10 (b), aggressive fuel cell use, which might lower the fuel cell efficiency during a load-following FC calibration, is only effective for a short period. Thus the hydrogen fuel consumption shows no difference overall with respect to control calibrations. However, the results in battery usage ΔSOC (0.51 % in load-following vs. up to 5 % in load-leveling for US06) and maximum power (15 vs. 30 kW) suggest that it is feasible to accommodate a smaller size battery, saving weight and volume in load-following FC. Thus, FC transient power response and not efficiency is the key consideration in sizing the battery in a hybrid FC vehicle.

As can be seen in λ_{O_2} and the battery current profile in Figure 6.10, minimizing battery power with load-following calibration is followed by larger deviation in oxygen excess ratio than that with load-leveling calibration. High bandwidth in regulating v_{bus} to v_{bus}^{ref} results in abrupt I_{net} variation and thus drop in λ_{O_2}. It is more clear in Figure 6.12 that there is a tradeoff between the two performance variables, namely, the battery SOC and oxygen excess ratio. The oxygen excess ratio regulation degrades when the SOC variations are reduced. Therefore, decision in controller tuning

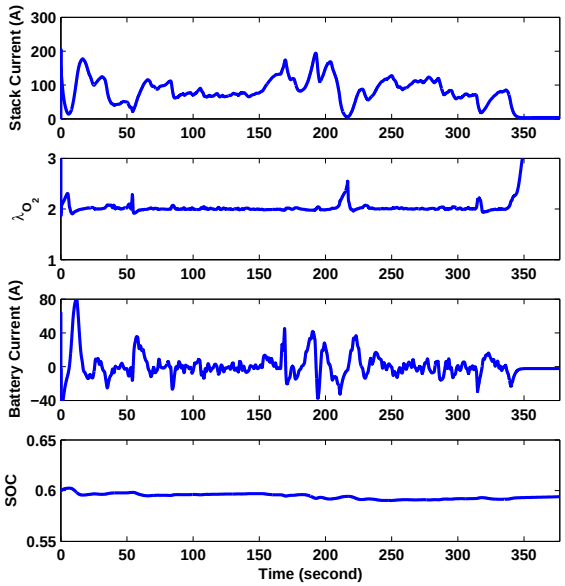

(a) FC current, oxygen excess ratio, battery current and SOC

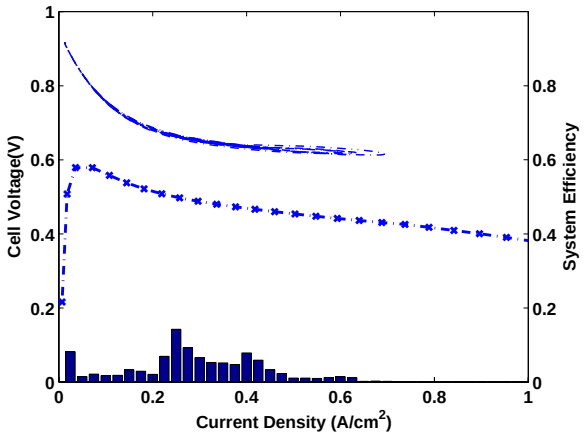

(b) System efficiency (-x-), FC response ($\cdots$) and distribution (bar)

Figure 6.9: Fuel cell and battery operating characteristics of hybrid vehicles for a portion of the US06 cycle - load-leveling FC

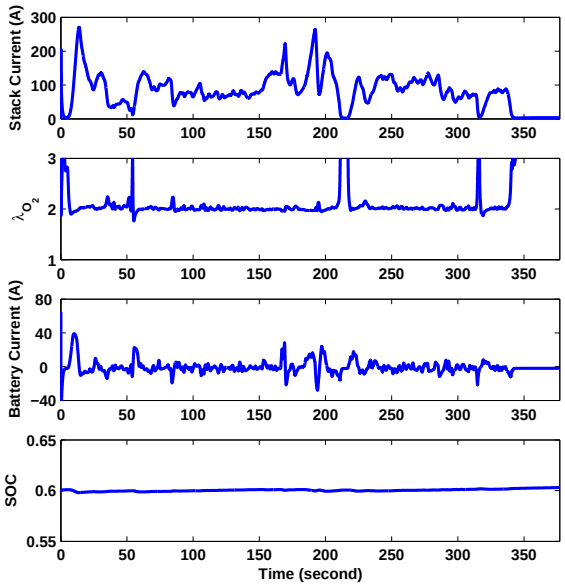

(a) FC current, oxygen excess ratio, battery current and SOC

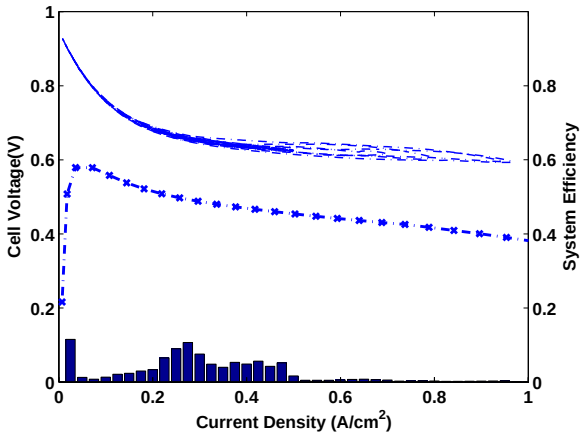

(b) System efficiency (-x-), FC response (···) and distribution (bar)

Figure 6.10: Fuel cell and battery operating characteristics of hybrid vehicles for a portion of the US06 cycle - load-following FC

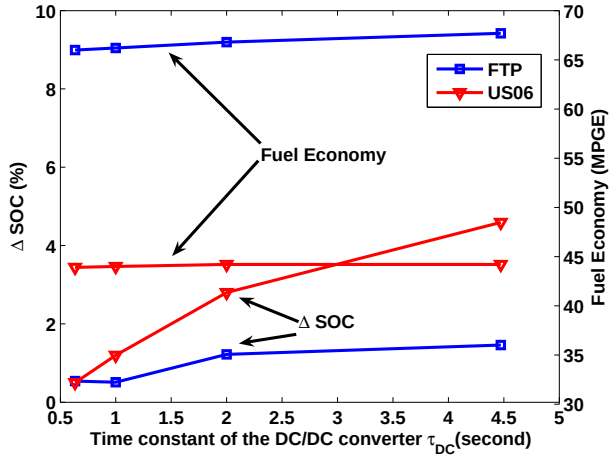

Figure 6.11: Battery usage and fuel economy with respect to controller calibration and the cycle

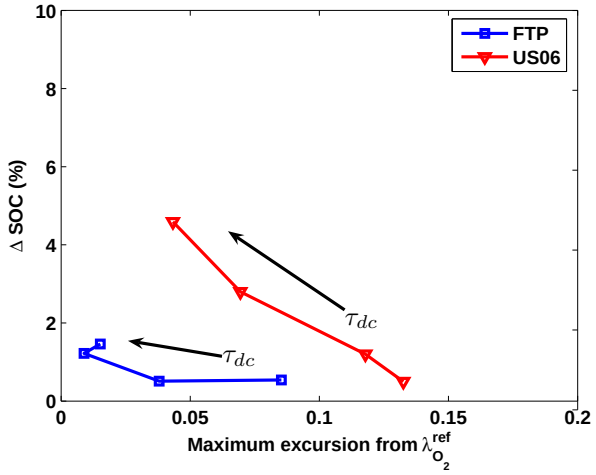

Figure 6.12: Battery usage and oxygen excess ratio with respect to controller calibration and the cycle

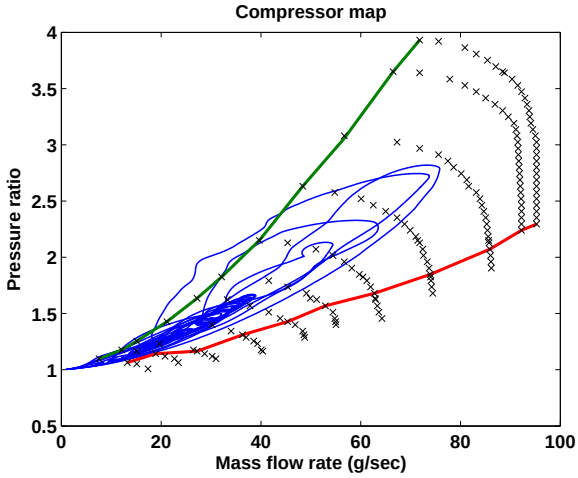

Figure 6.13: Compressor transient response(blue line) on static compressor map(x) with load-following FC power

and battery sizing should be done under the specification for maximum allowable oxygen excess ratio deviation.

In the controller tuning, actuator limits should be also be taken into account. Specifically, in a high-pressure FC system with an air supply compressor, the dynamic behavior of the compressor imposes additional limitations through its surge and choke characteristics. Surge causes large variations in flow and choke is an upper limit to the compressor air flow. In a fuel cell system there is a potential for both compressor surge and choke during an abrupt decrease and increase, respectively, in the applied compressor voltage command v_{cm}. Figure 6.13 shows the compressor transient response with load-following FC on a portion of the US06 cycle. As can be seen in the Figure 6.13, the transient responses are mostly within the region of safe compressor operation, not falling into the surge region (left solid line) or choke region (right solid line). A more sophisticated control for surge prevention by manipulating current load can be found in [68].

Another significant compressor consideration arises from its parasitic loss and its effects on the FC system efficiency at low loads. Lowering the minimum air flow rate in the compressor helps in achieving high efficiency in low power ranges [59]. The minimum air flow rate in the compressor can be as low as 5 g/s (the air flow at the maximum power is 95 g/s) with the controller described in this work. Also note here that the fuel cell model in this work is not turned off anytime during simulation because 500 W of accessary load is always applied independently of the vehicle speed. The simulation result shows that the FC efficiency is always over 40 % mainly because of low minimum air flow rate explained above (see all histograms of driving cycle simulations).

6.2.3 Centralized control

In fuel cell hybrid power systems, the performance variables, oxygen excess ratio and battery SOC, are defined through the interaction between the fuel cell system and DC/DC converter. Controller

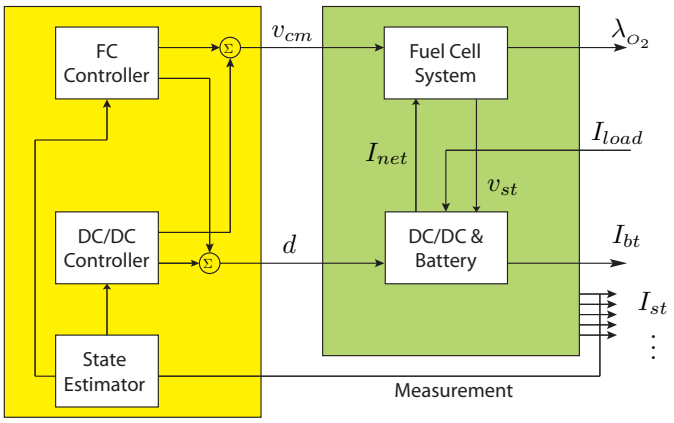

Figure 6.14: Centralized control architecture in fuel cell hybrid power

bandwidth of the DC/DC converter mainly determines SOC by v_{bus} regulation and λ_{O_2} through controlling current from the FC, I_{net}. Another control design that takes into account directly the tradeoff between small excursions in λ_{O_2} and SOC is called multivariable control and it results in a centralized controller as shown in Figure 6.14.

We apply a model-based linear quadratic regulator approach for the whole FC-DC/DC-battery hybrid system, which is similar to the approach in Chapter 5. This coordinated control preserves the control authority on oxygen regulation and power distribution in the same way as decentralized control, and in addition introduces interaction between the FC and the converter controllers. The resulting optimal control produces additional command to d through the estimated deviation in λ_{O_2}. Moreover, the v_{cm} command is now shaped through its effects to current drawn from the battery I_{bt}.

A linear model is reformulated for FC-battery hybrid system from the previous section. Again, the operating point is set at $\lambda_{O_2} = 2$, and $v_{bus} = 400$ V when fuel cell stack provides $P_{net} = 40$ kW. The linearized plant is denoted by

$$\begin{aligned} \dot{x} &= Ax + B_u u + B_w w \\ y &= C_y x + D_{yu} u \\ z &= C_z x + D_{zu} u \end{aligned} \tag{6.4}$$

where the state x, input u, disturbance w, measurement y, and performance variable z, are

$$\begin{aligned} x &= \begin{bmatrix} p_{O_2} & p_{N_2} & \omega_{cp} & p_{sm} & I_{net} & v_{bus} \end{bmatrix}^T \\ w &= I_{load} \\ u &= \begin{bmatrix} v_{cm} & d \end{bmatrix}^T \\ y &= \begin{bmatrix} W_{cp}^{ref} - W_{cp} & I_{bt}^m \end{bmatrix}^T \end{aligned}$$

$$z = \begin{bmatrix} \lambda_{O_2} & I_{bt} \end{bmatrix}^T \tag{6.5}$$

To eliminate steady-state error, the integrators on the two measurements, $W_{cp}^{ref} - W_{cp}$ and I_{bat}^m, are added to the controller. The state equations of the integrators are

$$\frac{d}{dt}\begin{bmatrix} q_1 \\ q_2 \end{bmatrix} = \begin{bmatrix} W_{cp}^{ref} - W_{cp} \\ I_{bt}^m \end{bmatrix} \tag{6.6}$$

where W_{cp}^{ref} from Equation (3.7). The LQR control law is determined to minimize the cost function, which is similar to the one in Section 5.2.2.

Note here that the centralized controller penalizes deviations of the battery current I_{bt} instead of v_{bus} in order to minimize the use of the battery. As can be seen from the decentralized load-following FC hybrid scheme (in Figure 6.10), reduced I_{bt} helps minimizing SOC indirectly. The information that is required for the centralized controller is collected by the state estimator designed from the various existing measurements, namely, the stack current I_{st}, the stack voltage v_{st} and the supply manifold pressure p_{sm} similar to the scheme in Chapter 5.

This communication and coordination help obtain accurate control in air delivery and improve transient FC performance. Communication between the FC controller and DC/DC controller yield optimized performance in coordinated control, resulting in reduced battery usage. Figure 6.15 shows the simulation result of the centralized control for the portion of the US06 cycle. As can be seen in the figure, the maximum current from the battery is limited to 30 A or 12 kW power, compared with the 15 kW maximum power obtained from the load-following decentralized control in Figure 6.10. The variation in SOC is 0.39 %, which is lower than the 0.51 % achieved through the load-following decentralized control in Figure 6.11.

6.3 Control of FC hybrid power - part (b)

In previous section, it is shown that model-based control calibration in FC hybrid power system determines the power split and the hybridization level. Given the analysis results, applying small-sized battery or batteries, instead of 31 series of batteries, will reduce the vehicle volume and weight since the changes in hybridization level has no effects on overall system efficiency. However, the electric configuration used in previous section constrains us to use large-sized battery because a large series of batteries needs to support high voltage DC bus.

The electric configuration in Figure 1.2(b) allows us to use separate voltages in the stack and the battery, thus enables to accommodate smaller battery (see also Figure 6.2). Reducing weight of the battery and power electronic devices will improve even better efficiency unless it compromises on performance [58]. In this section, the performance analysis and evaluation is performed with control design and battery sizing. To compare the performances directly with the previous results, the vehicle mass is not changed even with small-sized battery.

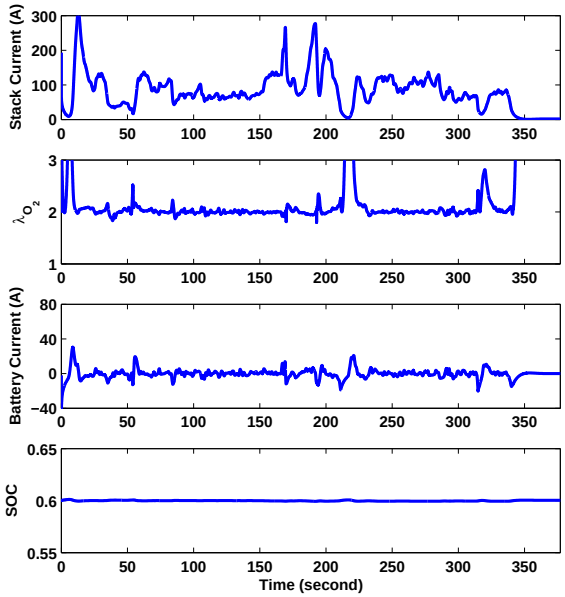

Figure 6.15: Fuel cell and battery operating characteristics of hybrid vehicles for a portion of the US06 cycle - centralized control

6.3.1 Hybrid power management

Here we apply decentralized control with the fuel cell control design in Chapter 3 and the bidirectional DC/DC converter control in Chapter 5. As shown in the flowchart of Figure 6.2, the fuel cell model uses the stack voltage as the input in this case. Although the stack voltage is the input of the fuel cell system model instead of the fuel cell current, the air supply dynamics of the fuel cell system has not changed as can be seen from the experimental results in Chapter 4. The same air supply control in Equation (3.32) is applied with net load current and the compressor air flow rate measurements, which is shown in Chapter 3.

The control design in the bidirectional DC/DC converter follows the same procedures as in Section 6.2, except that the bidirectional DC/DC converter protect the FC from severe voltage load variations, instead of the current load changes. The stack voltage load can vary following the changes in traction load as shown in Figure 5.7, which could result in oxygen starvation. Therefore the control objective of the bidirectional DC/DC converter in the electric configuration of Figure 6.2 is as follows: (i) protect the fuel cell system from large changes in (voltage) load (ii) protect the battery from large current draw. These objective can be captured in a quadratic cost function

$$J = \int_0^\infty \begin{bmatrix} I_{bt} & v_{st} \end{bmatrix} Q \begin{bmatrix} I_{bt} \\ v_{st} \end{bmatrix} + u^T R u + q^T Q_I q \, dt. \tag{6.7}$$

where the integrator q corresponds to the battery state of charge, $dq/dt = I_{bt}$, and the optimal state

feedback control is given in Section 5.1.4

$$d(s) = -K_{PI} I_{bt}(s) - K_{Pv} v_{st}(s) - \frac{K_{II}}{s} I_{bt}(s). \tag{6.8}$$

In the quadratic cost function both v_{st} and I_{bt} are penalized. The weight on the stack voltage v_{st} penalizes the variation of the fuel cell load. An increase in the weight $Q(2,2)$ results in a controller that allows less fuel cell load variations, which consequently causes higher battery currents in order to follow the vehicle traction load. The weights on the battery current and the integrator affect the regulation performance on battery current and state of charge. Increases on these weights will results less battery assist in hybrid mode and might cause violation in maximum fuel cell current limit or oxygen starvation.

6.3.2 Battery sizing

With the electric architecture of fuel cell hybrid with bidirectional DC/DC converter, the battery size (or number of battery modules) can vary unlike the case in Section 6.2. Finding minimum number of batteries will minimize the vehicle weight, and thus maximize the hydrogen fuel economy if the overall system efficiency is conserved. The optimal battery size in FC hybrid has been determined using dynamic programming [64]. The dynamic programming technique can also define the power split with constraints on fuel cells and battery performance. The optimization results is, however, dependent to the specific cycle and the implementation on real-time, causal controller is not straightforward.

Here we design a bidirectional DC/DC converter controller to split power between the FC and battery first. Then the number of batteries that satisfies the FC and battery constraints is determined with driving cycle simulation comparison. Since the nominal battery voltage is 24 V, the battery pack is designed with series of two batteries and several parallel connections. Tradeoff between the fuel cell and the battery performance is now realized as constraints in the current and voltage of both the FC and battery. The control gain tuning of the bidirectional DC/DC converter is performed in favor of the fuel cell performance on oxygen starvation and maximum current. To minimize the size (or number) of the batteries, the fuel cell load needs be operated as the load-following hybrid. After several simulation trial to find the same fuel cell dynamics with the load-following hybrid in Section 6.2, the LQR weight matrix are chosen as $Q = \text{diag} \begin{bmatrix} 5 & 750 \end{bmatrix}$, $Q_I = 0.01$ and $R = 1 \times 10^6$ for Equation (6.7). As can be seen in the weight matrix, the weights on I_{bt} and the integrator are much smaller than the one used for v_{st}. This combination of weights produces a controller that protects the fuel cell from oxygen starvation at the cost of larger battery usages.

Simulation analysis is performed with different number of battery modules. Table 6.4 shows the battery usage with different number of batteries in two driving cycles. The constraints on battery voltage are shown in Table 6.3. The battery model used here is the same with the one in Section 6.1.2. For the US06 driving cycle, the battery voltage exceed the maximum allowable in the case with 8 batteries. Exceeding the maximum battery voltage will result in overcharging with

Table 6.4: Battery usage comparion

No. of batteries	Min. voltage ($\geq$ 9.5)		Max. voltage ($\leq$ 16.5)	
	FTP	US06	FTP	US06
8	11.34	12.06	16.72	16.72
10	11.61	12.21	16.11	16.05
12	11.80	12.32	15.58	15.58

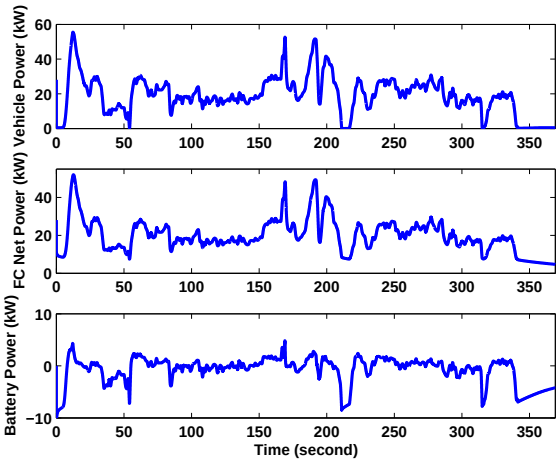

Figure 6.16: Power split in a portion of US06 driving cycle

high current. When the number of batteries is 10, the changes in the battery voltage are within the allowable range. As the number of batteries increases, the battery loads decrease with smaller variation observed in the voltage. We choose 10 batteries for the following performance validation.

Simulation comparison is also performed to see the operating characteristics on the portion of the US06 driving cycle as shown in Figure 6.7. Figure 6.16 shows the simulation result in power split during the portion of the US06 cycle. As can be seen in the figure, fuel cell power almost follows the vehicle traction load and the power-assist from the battery is minimal as intended. Battery usage is actually smaller than the one observed at the load-following hybrid (9 kW versus 15 kW, see Figure 6.8).

Figure 6.17 shows that the oxygen excess ratio λ_{O_2} is well regulated around the desired setpoint ($\lambda_{O_2}^{ref} = 2$) without large excursion, which could cause oxygen starvation. The λ_{O_2} regulation is achieved despite the large stack voltage variations, which result in current densities up to 1 A/cm^2 as shown in Figure 6.18. Overall operating characteristics of the fuel cell are similar as in the load-following hybrid in Figure 6.10 or the centralized control in Figure 6.15. Since the number of batteries is reduced to about one-third of the one with the load-following FC in Section 6.2, variations in the battery SOC are larger than the ones observed in previous designs. Here the control strategy does not regulate the battery SOC directly. However, the weights on I_{bt} and its integrator determines the battery performance, and thus the SOC remains within safe ranges.

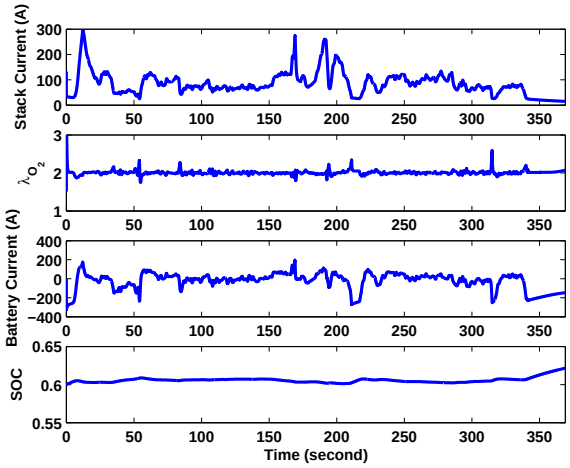

Figure 6.17: Fuel cell and battery operating characteristics of hybrid vehicles for a portion of US06 cycle

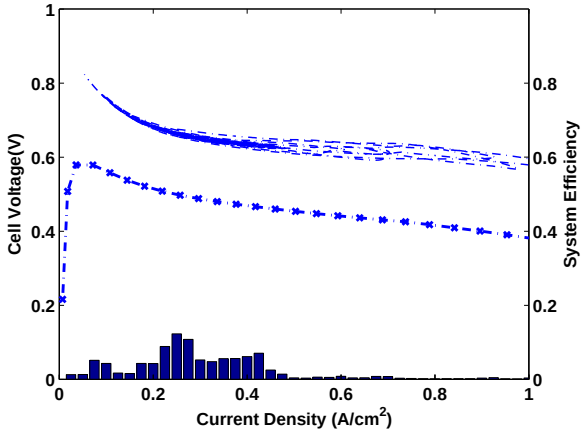

Figure 6.18: System efficiency (-x-), FC response ($\cdots$) and distribution(bar) for a portion of US06 cycle

The hydrogen fuel economy on the FTP cycle is 65 MPGE and on the US06 cycle is 45 MPGE. As expected, observed that the hydrogen fuel economy is same as the results in Section 6.2 because the hybrid operation characteristic is similar to the load-following hybrid in Section 6.2. Note here that the actual hydrogen fuel economy of the system with the smaller battery will be improved if one considers the reduction in the vehicle weight due to the reduced battery and power electronics weight.

In this chapter, we design decentralized and multivariable controllers regulating the bus voltage and preventing fuel cell oxygen starvation using dynamic causal models for a direct-hydrogen fuel cell and a DC/DC converter. Various controller gains are used to span the fuel cell operation from load-following to load-leveling, and hence, determine the required fuel cell-battery sizing (hybridization level) and the associated trends in the fuel economy. Two candidate electric architectures are considered and the control strategies and tunings for these architectures are presented.

The proposed controllers directly manipulate actuator commands, such as the DC/DC converter duty cycle, and achieve a desired power split. The controllers are demonstrated through simulation of a compact sedan using a mild and an aggressive driving cycle. Our results provide insight on the strategy and calibration of a fuel cell hybrid electric vehicle with no need for a supervisory controller that typically depends on optimal power split during a specific driving cycle.

Chapter 7

Conclusions

Prompt response is essential in fuel cell power applications. Transient performance requirement is sometimes more critical than efficiency, given the importance of accepting fast changing and unpredictable electric loads. The fuel cell response is, however, limited by the complex dynamics associated with mass and heat balances inside and outside the FC stack. To mitigate these limitations, a fuel cell stack is typically combined with a battery through a DC/DC converter into a hybrid power system. Hybridization may protect the fuel cell from harmful transitions that can cause oxygen starvation. In addition, hybridization may lead to higher fuel cell efficiency, although the anticipated efficiency improvements are not same as the ones observed in ICE hybrid systems. Hybridization, finally may introduce unnecessary weight and complexity associated with the addition of batteries.

The dissertation addresses modeling, analysis and controller design of FC power combining a fuel cell system, a DC/DC converter and a battery in various electric configurations. We design controllers using linear quadratic optimization techniques and span the fuel cell operation from load-following to load-leveling, and hence, determine the required fuel cell-battery sizing (hybridization level) and the resulting trends in the system efficiency. The controller designed optimally manages the air and the electron flow, balancing the slow power response of the fuel cell stack without overestimating or underestimating its transient capabilities. Our optimal control scheme utilizes minimal battery power, defining minimal hybridization needs in FC autonomous power systems.

The ultimate goal of this work is to contribute to the fuel cell technology in the areas of control and coordination, specifically for hybrid power applications where many power sources are employed. There is an intense interest right now about augmenting FCs in the power grid. Depending on the connection (parallel, series, etc) the control methodology and the dynamic load capability change. This work will also augment the recent research in power management of fuel cells for optimal fuel economy in transportation applications. Given the emphasis on coordination issues and multidisciplinary aspects, this work will contribute to the core system technology used for design assessment of the other future energy systems. Eventually our work on multivariable dynamic energy systems can be augmented to address reliable distributed energy by defining requirements on the minimum com-

munication among the embedded controllers in distributed power sources and the need for energy storage.

7.1 Air flow control in power-autonomous FCS

This dissertation fist focused on the question of the best transient performance (or limitations) of the stand-alone fuel cell system as a power source before hybridization. To this end, a simple but accurate, low-order FC system model is introduced to describe the necessary flow and electric dynamics using a combination of physical principles and empirical relations. Model validation is pursued through experiments on a 1.2 kW, 47 cell low pressure FC stack.

The coupling between the electric and flow paths in a compressor-driven fuel cell stack is clarified for the first time. This coupling imposes control limitations with regard to NMP zeros in the air flow control path affecting both performance and measurements. The control problem is then formulated in the general control form, and the theory of fundamental limitations is used to clarify the difficulties in avoiding oxygen starvation during load changes. Although the load changes are known (measured) their effects cannot be completely attenuated because NMP zeros make the application of cancellation controllers unfeasible. The design tradeoffs imposed by the Poisson integral associated with the NMP zero are then summarized. Finally, a combined feedforward and feedback control is designed to achieve adequate performance and illustrate the performance limitations in simulation.

7.2 Control design of FC hybrid power system

The second question addressed in this dissertation is the control calibration and associated efficiency benefits of various hybrid fuel cell electric architectures. System integration and control issues are also associated with various electric architectures with the fuel cell stack, DC/DC converter and battery. To investigate the coupled dynamics associated with current and voltage in a fuel cell power system, we include a DC/DC converter that transforms unregulated DC power from the FC to regulated DC grid power. We have demonstrated performance tradeoff in achieving the stack and grid objectives.

Despite many publications that debate on the size and efficiency of the DC/DC converter and battery, dynamic performance and control design issues have not been addressed. In this work, we show development of a low level controller that directly manipulates physical actuator inputs, and at the same time, it offers calibration parameter for power optimization. Although these issues cannot be all treated fully in a comprehensive way, our work is distinct in that we focus on the physical connection and also control difficulties. We include the dynamic interaction of voltage, current, flow, pressure arising from physical interconnection instead of managing power in higher level.

In this work we considered a compact sedan fuel cell electric hybrid with a compressor driven 75 kW proton exchange membrane fuel cell, a DC/DC converter and a battery, and assess the effect of different control calibrations and strategies in the power split, the vehicle efficiency, the

battery utilization and the FC oxygen starvation. A forward-facing (causal) model is used and the assessment is performed for two different driving cycles with mild (FTP) and aggressive (US06) accelerations.

The overall controller automates two processes. First, it adjusts the FC air flow through a compressor motor command to minimize oxygen starvation periods. Second, it regulates the bus voltage or the battery current through the duty cycle of the DC/DC converter. The FC compressor controller is novel because its calibration balances the benefits from the instantaneous flow increase and its drawbacks from the increase in the FC load (parasitic losses). Once the FC controller is tuned, a DC/DC converter controller is designed to transform the unregulated FC voltage to regulated bus voltage.

Different gains in the converter controller achieve different transient responses in the bus voltage regulation. Fast voltage regulation corresponds to a load-following FC calibration with high FC utilization and low battery utilization (50 kW in FC power versus 15 kW in battery power for the aggressive cycle). Slow voltage regulation results in a load-leveling FC calibration that does not exhibit any significant benefits when compared to the load-following calibration. The control calibration has minimal effect on fuel economy primarily because typical driving cycles can be accomplished by a well controlled FC with efficiencies up to 45 %. A smaller battery size (10 versus 31 packs) can reduce the vehicle weight and volume without adversely affecting the FC performance (efficiency, oxygen excess ratio) or requiring operation close to the compressor surge and choke limits.

The control design in this work deals with actual current and voltage instead of power unlike many other papers, respecting their causal relationship. Also the designed control system does not require inner loop controllers that realize the power split command from a supervisory controller since the designed controllers manipulate directly physical actuators setting in the FC stack system and the DC/DC converter. Therefore applying and re-tuning our control methodology to various hardware configurations can be done directly without cycle dependent optimization.

Although the analysis of FC hybrid power system is based on vehicle propulsion application, any PEM FC hybrid system, such as auxiliary power unit or distributed power source, will benefit from the control design and analysis we performed in this thesis.

7.3 Future Study

Fuel cell vehicle: The transient performances and control limitations in PEM FC system depend on the air supply system as we have shown in this study. The air supply system also has an important role in the overall system efficiency of the PEM fuel cell stack. The operating pressure is one of the major factors in integrating the air supply system, including a compressor or blower, manifold, channel and orifice design. Since vehicle propulsion applications impose strict requirements on the size and weight, optimizing the overall FC system efficiency is highly dependent on both the air supply system design and its control. The combined control and optimization will be the next step in designing an air supply system for fuel cell vehicle.

In a fuel cell electric hybrid vehicle, the regenerative braking helps capture and reuse the energy and also may result in fuel economy improvement. In this study, regenerative braking was not considered to generalize the problem for the FC hybrid power system for not only vehicular application but also portable and stationary power. The FC hybrid power train model with regenerative braking will show detailed results, including the effect of the regenerative braking over the fuel economy.

System coordination and communication: In an electric architecture of the fuel cell hybrid power system, the communication issues arise with system coordination. The communication in centralized control in this study may have advantages over the non-causal communication with such as power-request and power-available signals. The power-request signal, which is mainly an interpretation of driver power demand, and the power-available signal, which includes expected air supply into the stack based on the request, are both predictive information that can differ from the real system. Thus these signals may lead to inaccurate or conservative operation in fuel cell power. The communication and coordination presented in this work have the capability of monitoring the state of the system and manipulate physical actuators in real time.

The drawback of the coordinated, centralized control is the increase of computation for measurement and state estimation. Although the centralized control achieves similar performance as the results of to decentralized control, additional communication in centralized control will eventually help improving the system robustness in the area of such as monitoring and fault detection. Thus the centralized control in FC hybrid coordination needs to be extended to the communication study, which defines minimal communication among the hybrid power components.

List of Symbols

$\bar{R}$	Universal gas constant	8.3145 J/(mol·K)
A	Active area	cm^2
A_T	Opening area of the nozzle	
C	Capacitance, Controller	F
C_D	Discharge coefficient of the nozzle	
C_p	Specific heat capacity of the air	1004 J/(mol·K)
d	Duty cycle	
F	Faraday number	96,485
G	Transfer function, Conductance	℧
I	Current	A
i	Current density	A/cm^2
J	Inertia, Cost function	$kg{\cdot}m^2$
k	Flow constant, Motor constant	kg/(s·Pa), V/(rad/sec), N-m/A
L	Inductance, Observer gain	H
M	Molar mass	kg/mol
m	Mass, Multiplicity	
n	Number of cells	
p	Pressure	Pa
R	Resistance	Ω
SOC	State of charge	
T	Temperature, Torque	K, N·m
u	Control input	
V	Volume	m^3
v	Voltage	V

W	Mass flow rate	
w	Humidity ratio, Disturbance input	
x	Mass fraction, State	
y	Molar ratio, Measurement output	
z	Performance variable	

Greek letters

η	Efficiency	
γ	Ratio of the specific heat capacities of the air	1.4
λ_m	Membrane water activity	
λ_{O_2}	Oxygen excess ratio	
ω	Rotational speed	rad/sec
ϕ	Relative humidity	
τ	Time constant	

Subscripts

act	Activation loss
an	Anode
atm	Atmospheric
bt	Battery
ca	Cathode
cm	Compressor motor
$conc$	Concentration loss
cp	Compressor
D	Derivative
dc	DC/DC converter
fc	Fuel cell
$filter$	Filter
H_2	Hydrogen
in	Input
$load$	Load
LQR	Linear quadratic regulator
m	Motor
max	Maximum

n	Nominal
N_2	Nitrogen
O_2	Oxygen
ohm	Ohmic loss
out	Output
rct	Reacted
sat	Saturation
sm	Supply manifold
st	Stack
u	Control input
v	Vapor
w	Disturbance input
y	Measurement output
z	Performance variable

Superscripts

fb	Feedforward
ff	Feedback
m	Measurement
ref	Reference

Bibliography

[1] J. C. Amphlett, R. M. Baumert, R. F. Mann, B. A. Peppley, P. R. Roberge, and A. Rodrigues, "Parametric modelling of the performance of a 5-kW proton-exchange membrane fuel cell stack," *Journal of Power Sources*, vol. 49, pp. 349–356, 1994.

[2] J. C. Amphlett, E. H. de Oliviera, R. F. Mann, P. R. Roberge, A. Rodrigues, and J. P. Salvador, "Dynamic interaction of a proton exchange membrane fuel cell and a lead-acid battery," *Journal of Power Sources*, vol. 65, pp. 173–178, 1997.

[3] J. C. Amphlett, R. F. Mann, B. A. Peppley, P. R. Roberge, and A. Rodrigues, "A model predicting transient responses of proton exchange membrane fuel cells," *Journal of Power Sources*, vol. 61, pp. 183–188, 1996.

[4] M. Badami and C. Caldera, "Dynamic model of a load-following fuel cell vehicle: impact of the air system," SAE paper 2002-01-0100, 2002.

[5] F. Barbir, "System design for stationary power generation," in *Fuel Cell Technology and Application*, ser. Handbook of Fuel Cells - Fundamantals, Technology and Applications, W. Vielsthch, H. A. Gasteiger, and A. Lamm, Eds. John Wiley and Sons, 2003, vol. 4.

[6] J. Benziger, E. Chia, E. Karnas, J. Moxley, C. Teuscher, and I. G. Kevrekidis, "The stirred tank reactor polymer electrolyte membrane fuel cell," *AIChE Journal*, vol. 50, no. 8, pp. 1889–2000, Aug. 2004.

[7] G. Boehm, D. P. Wilkinson, S. Knights, R. Schamm, and N. J. Fletcher, "Method and appratus for operating a fuel cell," U.S. Patent 6 461 751, Oct. 8, 2002.

[8] D. D. Boettner, G. Paganelli, Y. G. Guezennec, G. Rizzoni, and M. J. Moran, "Proton exchange membrane fuel cell system model for automotive vehicle simulation and control," *ASME Journal of Energy Resources Technology*, vol. 124, pp. 20–27, 2002.

[9] S. Caux, J. Lachaize, M. Fadel, P. Shott, and L. Nicod, "Modelling and control of a fuel cell system and storage elements in transport applications," *Journal of Process Control*, vol. 15, pp. 481–491, 2005.

[10] W. Choi, J. W. Howze, and R. Enjeti, "Development of an equivalent circuit model of a fuel cell to evaluate the effects of inverter ripple current," *Journal of Power Sources, In press.*

[11] J. M. Cunningham, M. A. Hoffman, and D. J. Friedman, "A comparison of high-pressure and low-pressure operation of PEM fuel cell systems," SAE paper 2001-01-0538, 2001.

[12] J. M. Cunningham, M. A. Hoffman, R. M. Moore, and D. J. Friedman, "Requirements for a flexible and realistic air supply model for incorporation into a fuel cell vehicle (FCV) system simulation," SAE paper 1999-01-2912, 1999.

[13] J. M. Cunningham, R. Moore, S. Ramaswamy, and K. Hauer, "A comparison of energy use for a direct-hydrogen hybrid versus a direct-hydrogen load-following fuel cell vehicle," SAE paper 2003-01-0416, 2003.

[14] J. C. Doyle and G. Stein, "Robustness with observers," *IEEE Transactions on Automatic Control*, vol. 24, no. 4, pp. 607–611, Aug. 1999.

[15] R. W. Erickson and D. Maksimovic, *Fundamentals of Power Electronics*, 2nd ed. Norwell, MA: Kluwer Academic Publishers, 2001.

[16] G. Escobar, R. Ortega, H. Sira-Ramírez, J.-P. Vilain, and I. Zein, "An experimental comparison of several nonlinear controllers for power converters," *IEEE Control Systems Magazine*, vol. 19, no. 1, pp. 66–82, 1999.

[17] Z. Filipi, L. Louca, A. G. Stefanopoulou, J. T. Pukrushpan, B. Kittirungsi, and H. Peng, "Fuel cell APU for silent watch and mild electrification of a medium tactical truck," SAE paper 2004-01-1477, 2004.

[18] G. R. Flohr, "Performance considerations of a bi-directional DC/DC converter for fuel cell powered vehicles," SAE paper 2002-01-1902, 2002.

[19] J. S. Freudenberg, C. V. Hollot, R. H. Middleton, and V. Toochinda, "Fundamental design limitations of the general control configuration," *IEEE Transactions on Automatic Control*, vol. 48, no. 8, pp. 1355–1370, Aug. 2003.

[20] J. S. Freudenberg and D. P. Looze, "Right half plane poles and zeros and design tradeoffs in feedback systems," *IEEE Transactions on Automatic Control*, vol. 30, no. 6, pp. 555–565, June 1985.

[21] D. J. Friedman, "Maximizing direct-hydrogen PEM fuel cell vehicle efficiency - is hybridization necessary?" SAE paper 1999-01-0530, 1999.

[22] M. H. Fronk, D. J. Wetter, D. A. Masten, and A. Bosco, "PEM fuel cell system solutions for transportation," SAE paper 2000-01-0373, 2000.

[23] S. Gelfi, A. G. Stefanopoulou, J. T. Pukrushpan, and H. Peng, "Dynamics of low-pressure and high-pressure fuel cell air supply systems," in *Proceedings of the 2003 American Control Conference*, vol. 3, Denver, CO, June 2003, pp. 2049–2054.

[24] General Motors Corporation. (2003) GM - GMability Advanced Technology: HydroGen3 takes a big step toward the production line. [Online]. Available: http://www.gm.com/company/gmability/adv_tech/600_tt/650_future/hydrogen3_050103.html

[25] C. Gezgin, B. S. Heck, and R. M. Bass, "Control structure optimization of a boost converter: An LQR approach," in *Proceedings of the IEEE Power Electronics Specialists Conference*, vol. 2, St. Louis, MO, June 1997, pp. 901–907.

[26] G. C. Goodwin, M. E. Salgado, and J. I. Yuz, "Performance limitations for linear feedback systems in the presence of plant uncertainty," *IEEE Transactions on Automatic Control*, vol. 48, no. 8, pp. 1312–1319, Aug. 2003.

[27] D. Grupp, M. Forrest, P. Mader, C. J. Brodrick, M. Miller, and H. Dwyer, "Development of a retrofit fuel cell auxiliary power unit for truck idle reduction," SAE paper 2004-01-2629, 2004.

[28] W. B. Gu, C. Y. Wang, and B. Y. Liaw, "Numerical modeling of coupled electrochemical and transport precesses in lead-acid batteries," *Journal of The Electrochemical Society*, vol. 144, no. 6, pp. 2053–2061, 1997.

[29] Y. Guezennec, T.-Y. Choi, G. Paganelli, and G. Rizzoni, "Supervisory control of fuel cell vehicles and its link to overall system efficiency and low-level control requirements," in *Proceedings of the 2003 American Control Conference*, vol. 3, Denver, CO, June 2003, pp. 2055–2061.

[30] L. Guzzella and A. Sciarretta, *Vehicle Propulsion Systems: Introduction to Modeling and Optimization*. Berlin: Springer-Verlag, 2005.

[31] J. B. Heywood, *Internal Combustion Engine Fundamentals*. New York: McGraw-Hill, 1988.

[32] T. H. Hunt and R. Spiteri, "Method and system for controlling power distribution in a hybrid fuel cell vehicle," U.S. Patent 6 792 341, Sept. 14, 2004.

[33] T. Ishikawa, S. Hamaguchi, T. Shimizu, T. Yano, S. Sasaki, K. Kato, M. Ando, and H. Yoshida, "Development of next generation fuel-cell hybrid system - consideration of high voltage system," SAE paper 2004-01-1304, 2004.

[34] Z. Jiang, L. Gao, and R. A. Dougal, "Flexible multiobjective control of power converter in active hybrid fuel cell/battery power sources," *IEEE Transactions on Power Electronics*, vol. 20, no. 1, pp. 244–253, 2005.

[35] V. H. Johnson, "Battery performance models in ADVISOR," *Journal of Power Sources*, vol. 110, pp. 321–329, 2002.

[36] P. B. Jones, J. B. Lakeman, G. O. Mepsted, and J. M. Moore, "A hybrid power source for pulsed power applications," *Journal of Power Sources*, vol. 80, no. 1-2, pp. 242–247, 1999.

[37] J.-H. Jung, Y.-K. Lee, J.-H. Joo, and H.-G. Kim, "Power control strategy for fuel cell hybird electric vehicles," SAE paper 2003-01-1136, 2003.

[38] A. Y. Karnik and J. Sun, "Modeling and control of an ejector based anode recirculation system for fuel cells," in *Proceedings of the 3rd International Conference on Fuel Cell Science, Engineering, and Technology*, Ypsilanti, MI, May 2005.

[39] M. Kim, H. Peng, C.-C. Lin, E. Stamos, and D. Tran, "Testing, modeling, and control of a fuel cell hybrid vehicle," in *Proceedings of 2005 American Control Conference*, Portland, OR, June 2005, pp. 3859–3864.

[40] S. D. Knights, K. M. Colbow, J. St-Pierre, and D. P. Wilkinson, "Aging mechanisms and lifetime of PEFC and DMFC," *Journal of Power Sources*, vol. 127, pp. 127–134, 2004.

[41] P. T. Krein, *Elements of Power Electronics*. New York and Oxford: Oxford University Press, 1998.

[42] J. Larminie and A. Dicks, *Fuel Cell Systems Explained*, 2nd ed. Chichester and Hoboken, NJ: John Wiley & Sons, 2003.

[43] C.-C. Lin, H. Peng, M. Kim, and J. W. Grizzle, "Integrated dynamic simulation model with supervisory control strategy for a PEM fuel cell hybrid vehicle," in *Proceedings of the ASME Dynamic Systems and Control Division*, vol. 73, Anaheim, CA, Nov. 2004, pp. 275–286.

[44] C. Liu, T. Nergaard, L. Leslie, J. Ferrell, X. Huang, T. Shearer, J. Reichl, J. Lai, and J. Bates, "Power balance control and voltage conditioning for fuel cell converter with multiple sources," in *Proceedings of the IEEE Power Electronics Specialists Conference*, June 2002, pp. 2001–2006.

[45] T. Markel, K. Wipke, and D. Nelson, "Vehicle system impacts of fuel cell system power response capability," SAE paper 2002-01-1959, 2002.

[46] R. D. Merritt and J. D. Blair, "Constant voltage fuel cell with improved reactant supply and control system," U.S. Patent 5 366 821, Nov. 22, 1994.

[47] R. H. Middleton, "Trade-offs in linear control system design," *Automatica*, vol. 27, no. 2, pp. 281–292, Mar. 1991.

[48] Y. Motozono, M. Yamashita, M. Yamaoka, K. Nagamiya, and I. Maeda, "Fuel cell control apparatus," U.S. Patent 6 638 652, Oct. 28, 2003.

[49] W. E. Mufford and D. G. Strasky, "Power control system for a fuel cell powered vehicle," U.S. Patent 5 991 670, Nov. 23, 1999.

[50] A. Ohkawa, "Electric power control system for a fuel cell vehicle employing electric douple-layer capacitor," SAE paper 2004-01-1006, 2004.

[51] B. K. Powell and T. E. Pilluti, "A range extender hybrid electric vehicle dynamic model," in *Proceedings of the 33rd IEEE Conference on Decision and Control*, vol. 3, Buena Vista, FL, Dec. 1994, pp. 2736–2741.

[52] J. T. Pukrushpan, H. Peng, and A. G. Stefanopoulou, "Control-oriented modeling and analysis for automotive fuel cell systems," *ASME Journal of Dynamic Systems, Measurement, and Control*, vol. 126, no. 1, pp. 14–25, 2004.

[53] J. T. Pukrushpan, A. G. Stefanopoulou, and H. Peng, "Control of fuel cell breathing," *IEEE Control Systems Magazine*, vol. 24, no. 2, pp. 30–46, Apr. 2004.

[54] ——, *Control of Fuel Cell Power Systems: Principles, Modeling, Anylysis and Feedback Design*, ser. Advances in Industrial Control. London: Springer-Verlag Telos, 2004.

[55] J. T. Pukrushpan, A. G. Stefanopoulou, S. Varigonda, L. M. Pedersen, S. Ghosh, and H. Peng, "Control of natural gas catalytic partial oxidation for hydrogen generation in fuel cell applications," *IEEE Transactions on Control Systems Technology*, vol. 13, no. 1, pp. 3–14, Jan. 2005.

[56] L. Qui and E. J. Davidson, "Performance limitations of non-minimum phase systems in the servomechanism problem," *Automatica*, vol. 29, no. 2, pp. 337–349, Mar. 1993.

[57] K. Rajashekara, "Propulsion system strategies for fuel cell vehicles," SAE paper 2000-01-0369, 2000.

[58] S. Ramaswamy, R. Moore, J. M. Cunningham, and K.-H. Hauer, "A comparison of energy use for a indirect-hydrocarbon hybrid versus an indirect-hydrocarbon load-following fuel cell vehicle," SAE paper 2004-01-1476, 2004.

[59] P. Rodatz, G. Paganelli, A. Sciarretta, and L. Guzzella, "Optimal power management of an experimental fuel cell/supercapacitor-powered hybrid vehicle," *Control Engineering Practice*, vol. 13, no. 1, pp. 41–53, Jan. 2005.

[60] P. Rodatz, G. Paganelli, and L. Guzzella, "Optimizing air supply control of a PEM fuel cell system," in *Proceedings of the 2003 American Control Conference*, vol. 3, Denver, CO, June 2003, pp. 2043–2048.

[61] J. St-Pierre, D. P. Wilkinson, S. Knights, and M. Bos, "Relationships between water management, contamination and lifetime degradation in PEFC," *Journal of New materials for Electrochemical Systems*, vol. 3, pp. 99–106, 2000.

[62] K. Stanton and J.-S. Lai, "A thermally dependent fuel cell model for power electronics design," in *Proceedings of the IEEE Power Electronics Specialists Conference*, June 2005, pp. 1647–1651.

[63] J. Sun and I. Kolmanovsky, "Load governor for fuel cell oxygen starvation protection: A robust nonlinear reference governor approach," in *Proceedings of the 2004 American Control Conference*, vol. 1, Boston, MA, June 2004, pp. 828–833.

[64] O. Sundström and A. G. Stefanopoulou, "Optimal power split in fuel cell hybrid electric vehicle with different battery sizes, drive cycles, and objectives," in *IEEE Proceedings of 2006 International Conference on Control Applications, To be appeal*.

[65] A. D. Swingler and W. G. Dunford, "Development of a bi-directional DC/DC convreter for inverter/charger applications with consideration paid to large signal operation and quasi-linear digital control," in *Proceedings of the IEEE Power Electronics Specialists Conference*, vol. 2, June 2002, pp. 961–966.

[66] S. Um, C.-Y. Wang, and K. S. Chen, "Computational fluid dynamics modeling of proton exchange membrane fuel cells," *Journal of The Electrochemical Society*, vol. 147, no. 12, pp. 4485–4493, 2000.

[67] U.S. Department of Energy, Office of Fossil Energy, and National Energy Technology Laboratory, *Fuel Cell Handbook*, 7th ed. Morgantown, WV: EG&G Technical Services, Inc., 2004.

[68] A. Vahidi, I. Kolmanovsky, and A. G. Stefanopoulou, "Constraint management in fuel cells: A fast reference governor approach," in *Proceedings of 2005 American Control Conference*, Portland, OR, June 2005, pp. 3865–3870.

[69] A. Vahidi, A. G. Stefanopoulou, and H. Peng, "Model predictive control for starvation prevention in a hybrid fuel cell system," in *Proceedings of 2004 American Control Conference*, Boston, MA, June 2004, pp. 834–839.

[70] Y. Wang and C.-Y. Wang, "Transient analysis of polymer electrolyte fuel cells," *Electrochimica Acta*, vol. 50, no. 6, pp. 1307–1315, 2005.

[71] W.-C. Yang, B. Bates, N. Fletcher, and R. Pow, "Control challenges and methodologies in fuel cell vehicle development," SAE paper 98C054, 1998.

[72] W. H. Zhu, R. U. Payne, D. R. Cahela, and B. J. Tatarchuk, "Uniformity analysis at MEA and stack levels for a Nexa PEM fuel cell system," *Journal of Power Sources*, vol. 128, no. 2, pp. 231–238, Apr. 2004.